Studies on Electrocatalytic Activities of Boron Nitride of Various Structures towards Oxygen Reduction Reaction and Hydrogen Evolution Reaction

(種々の構造をもつ窒化ホウ素の酸素還元反応および水素生成反応に対する電極触媒活性に関する研究)

Ganesan Elumalai

Division of Graduate School of Chemical Sciences and Engineering
Graduate School of Chemical Sciences and Engineering
Hokkaido University

2014

Acknowledgement

Foremost, I would like to express my sincere gratitude to my advisor Prof. Kohei Uosaki, for the continuous support of my Ph.D. study and research, for his patience, caring, motivation, enthusiasm, immense knowledge and providing me an excellent research atmosphere. His guidance helped me in all the time of research and writing of this thesis. I could not have imagined having a better advisor and mentor for my Ph.D. study. His scientific spirit is a model virtue for my future career.

I would like to also express my sincere gratitude to Dr. Hidenori Noguchi, for his kindness, constant support, guidance, discussions and resolving the problems throughout my graduate study and thesis writing.

I would like to express my special thanks to Dr. Takuya Masuda for his guidance, advices and caring. I would like to also thank Dr. Mikio Ito, Dr. Yu Sun, Dr. Shengfu Tong and Mr. Cepi Kurniawan for their directions, co-operation and advices. I sincerely thank all of my group members who worked and studied together with me at the Nanointerface group for their kind co-operation.

I also take this opportunity to express my sincere gratitude to National Institute for Materials Science (NIMS) for offering me a NIMS Junior Researcher fellowship and Hokkaido University for offering me a Ph.D. position. My heartfelt thanks to Miss. Kyoko Okada for her support and kind assistance during my Ph.D. Study. And also my sincere thanks to Miss. Rumiko Enjoji for her support.

I sincerely thank all of my friends in Tsukuba for their constant support, encouragement, advices and for making comfortable life here in Tsukuba.

I would like to express my wholehearted thanks and love to my parents, sister, and grandparents for their constant support, encouragement and sacrifices. I sincerely dedicate my thesis to my parents for their hard work and selfless love.

Ganesan Elumalai

Tsukuba

September 2014

Table of Contents

Chapter 1

INTRODUCTION

1.1 General Introduction

Since the time of industrial revolution, the demands for energy have been raising exponentially. Fossil fuels such as oil, coal, natural gas etc., are utilizing for the current energy demands but it is a limited resource. When the requirement of the fossil fuels exceeds the price also proportionally get increases. In this case, the price hikes renewed the interest in alternative energy conversion devices, such as fuel cells (FCs) [1, 2]. FCs are one of the promising alternative energy sources for the future energy demand due to the lack of fossil fuels and its environmental impacts [1-8]. FCs was direct result of the discovery of water electrolysis in 1789 by Adriaan Paets van Troostwijk and Jan Rudolph Deiman. The discovery of the FC itself is usually attributed to Schönbein or Grove [4]. Their discoveries were published months after one another, which mean that 1839 is the year in which the concept of the FC was first published. Over the years interest in FCs has decreased, especially due to the emergence of fossil fuels and the combustion engine. Starting with the oil crises in the 1970's, interest in FCs has increased again in recent years. Initially, FCs were especially of interest for situations where normal combustion engines (or, in a previous era, steam engines) could not operate, or remote areas which were not connected to the power grid [4, 5]. This includes submarine and space applications. In the last few decades, automotive applications for the general public have become attractive both for consumers to have an alternative to ever-increasing gas prices, and for governments to reduce carbon emissions and dependence on oil [2]. There is a preferred type of FC for each application, with the proton exchange membrane fuel cell (PEMFC) preferred for the use in automotive applications [5, 6]. The higher power density and quick start up due to the lower operating temperature make this PEMFC the first choice for commercial applications such as laptop power and cell phone batteries as well [6]. However, the fuel in these cells will differ depending on the proposed applications. For use in vehicles, H_2 is preferred, due to its high power-density and higher operating potentials. The difficulty in storing this gas makes it less suitable for smaller applications like the previously mentioned laptops and cell phones. For those applications, liquid fuels such as methanol (direct methanol fuel cell DMFC), formic

acid (direct formic acid fuel cell DFAFC) or ethanol (direct ethanol fuel cell DEFC) are preferred. The nomenclature of these FCs includes "direct" to stress that the respective fuels are used directly, and not reformed to H_2 before use in the cell. Finally, for large stationary applications, solid oxide fuel cell (SOFC) [4, 7] are preferred, both because they are easier to adapt to existing infrastructure [2] and can operate at higher current densities [4].

1.2 Working principle of Fuel cell and water electrocatalysis

FC is an energy device which converts chemical energy into electrical energy using fuels such as H_2, O_2, air, etc. There are many types of FCs, but they all consist of anode, cathode and electrolyte that allow electrons to move between the two sides of the FC [1-8]. Electrons are drawn from anode to cathode through an external circuit, producing direct current electricity as shown in Figure 1.1.

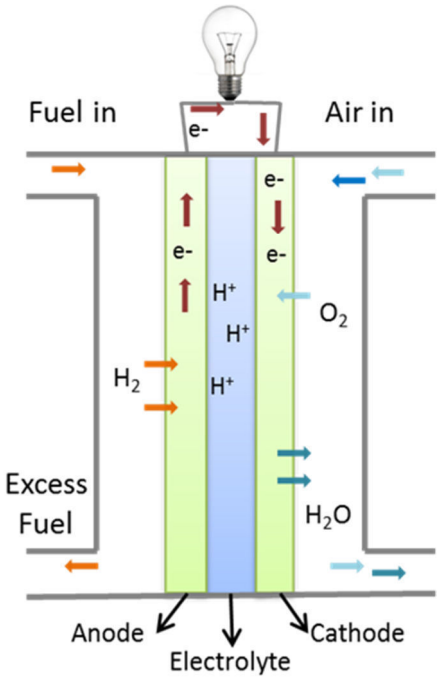

Figure: 1.1 Scheme of FC systems.

PEMFCs are one of the best FC system which operates on H_2/air are being considered as high efficiency, low pollution power generators for stationary and transportation applications [9-11]. Figure 1.1 shows a typical FC system in which, H_2 is oxidized at anode and O_2 is reduced at cathode as expressed in equation (1.1), (1.2) and (1.3).

H_2 is consumed at anode, yielding electrons to cathode and producing H^+ ions:

$$H_2 \rightarrow 2H^+ + 2e^- \qquad E^o = 0.00 \text{ V vs SHE} \qquad (1.1)$$

The H^+ ions are conducted through the proton conducting membrane electrolyte, and are combined at the cathode with electrons and the O_2 to generate water:

$$1/2O_2 + 2H^+ + 2e^- \rightarrow H_2O \qquad E^o = 1.23 \text{ V vs SHE} \qquad (1.2)$$

Thus, the PEMFC combines H_2 and O_2 to generate electrical power the only by-products are and pure water and heat:

$$H_2 + 1/2O_2 \rightarrow H_2O \qquad E^o_{cell} = 1.23 \text{ V vs SHE} \qquad (1.3)$$

Electrocatalysts are playing a crucial role in H_2 oxidation and O_2 reduction reactions during FC operation [11-13]. Oxidation of the H_2 molecule is widely studied and comparatively easy by using Pt catalyst [14-21]. Nevertheless, the reduction of O_2 molecule is more challenging due to the overpotential, it causes substantial electric losses. Appropriate electrocatalytic materials for O_2 reduction have not yet discovered [9-11, 22-56]. The critical role of the catalyst has commonly recognized in both catalytic activity and durability [57-60]. The catalyst should have several important properties including excellent electronic conductivity, high corrosion resistivity, uniform particle size distribution, high surface area, strong cohesive force to catalyst particles, easy formation of uniform dispersion of catalyst particles on their surface, etc., to achieve a high performing FC catalyst [57]. For example, currently Pt or the Pt-based catalyst supported on carbon materials [9-11, 22-56] are the most used catalysts in PEMFCs, which are porous conductive materials with a high specific surface area of >100 $m^2\ g^{-1}$ [61]. A state-of-the-art FC requires 0.5 mg Pt per cm^2 electrode area. These results are obtained from 0.5 g Pt per kW of power, or 50 g Pt per 100 kW vehicles [62]. At present, around 200 tons of Pt is being produced each year, globally. Only 4 million cars could be produced, by the current annual production of Pt, using current technology. The current output of the automobile industry is at least an order of magnitude larger than this. Therefore, for PEMFCs to become economically viable, catalyst costs need to be reduced to a similar level as those of the Pt group metals used in catalytic converters for internal combustion engines. The anode loading could be dropped to 0.05 mg cm^2 without

measurable kinetic losses. However, 0.4 mg cm^2 is currently needed at the cathode, where the ORR takes place [62]. Carbon supports for Pt loading are excellent in terms of their large surface area, high electrical conductivity, and pore structures, [34, 63-65] the major drawback is the corrosion caused by electrochemical oxidation that affects the catalyst strength and reliability in a PEMFC operation. For example, the oxidation of the carbon support has clearly been observed during long-term FC operation (>500 h) at higher temperatures [66, 67]. The Pt particles were either separated from the carbon supports due to the oxidation of the carbon or agglomerated into larger sizes because of the loss in electrocatalytic surface area. The situation became even worse when the FC has operated at an extremely high temperature (300^oC) [57]. In the following sections the commonly used catalysts in FCs were briefly reviewed.

1.3 Oxygen reduction reaction (ORR)

The most abundant element in the Earth's crust is O_2. The oxygen reduction reaction (ORR) has been extensively studied and it is the most crucial process in FCs [22, 23]. ORR is one of the key steps in PEMFC. The pronounced irreversibility of the reactions involved has imposed severe limitations in the understanding of the multiple consecutive steps of the reaction. In the most cases at current densities practical for kinetic studies, the current-voltage data are not sensitive to the back reaction and hence yield information only up to the rate-controlling step, which usually occurs early in the pathway. Further, the reduction and oxidation processes are studied only at widely separated potentials and thus the surface properties, e. g. electronic (such as work function and d-band character), adsorption energy of reaction intermediates, geometrical arrangement of atoms, and possibly concentration of surface defects [44-55]. These kinds of situation made more number of complicated possible pathways for ORR. The reason of these complicated situations were outlined by Damjanovic in his pioneering review [56]

(1) Nobel metals and their alloys can only withstand the highly positive potential associated with O_2 reduction (or oxidation) without undergoing dissolution themselves and hence contributing to the overall current.
(2) The mechanistic analysis of ORR is relatively involved owing to the numerous reaction steps and reaction intermediates with the energy of adsorption varying with the electrode potential and coverage. Furthermore, the reduction of O_2 may proceed

either by a two electron process to H_2O_2 or by a four electron process leading to water [68, 69]. H_2O_2 may at-least partially, reduce to water, or it may catalytically decompose.

The direct 4-electron reduction pathway:

$$O_2 + 4H^+ + 4e^- \rightarrow H_2O \quad (1.4)$$

Two electron reduction pathway:

$$O_2 + 2H^+ + 2e^- \rightarrow H_2O_2 \quad (1.5)$$

(3) In the potential range in which O_2 dissolution occurs, the electrode surface may be covered with oxide or relatively bare, so meaningful conclusion on the catalysis may be drawn.

(4) Due to low exchange current densities, other electrode reactions may become potential controlling, particularly at low current densities (in alkaline solutions, the exchange current density for the H_2O_2 couple on most electrode surfaces is quite high compared to that for all the overall four-electron reduction to water, as consequence, it has possible to obtain more insight into this pathway). So even traces of impurities can profoundly affect the overall kinetic.

As described in the working principle and water electrolysis section, two half-reactions occur in the process of generating energy in the FC, and it is known that the reaction happening at the cathode side is prone to high overpotential and slow reaction kinetics compared to the other at the anode, thus becoming the rate limiting reaction [43]. This leads to the higher amount of Pt required for cathode than anode side, and research efforts have been focusing on reducing or eliminating the Pt loading on the cathode catalysts. Also, the slow kinetics and the expensive Pt-based catalysts have become a major obstacle towards more extensive usage of PEMFC for households and automobiles. Great efforts have been made to develop new materials as ORR catalysts, but few materials have reached the requirement of high economical feasibility, high discharging efficiency, and long life.

1.3.1 Metal and its alloys for ORR

1.3.1.1 ORR on metal surface

The electrocatalytic reduction of O_2 and its mechanism on a Pt electrode have been widely studied. It is a multi-electron process with a number of elementary steps, involving different reaction intermediates. A simplified version of the mechanism is shown in Figure 1.2 [13, 70]. The mechanism indicates that O_2 can be reduced either directly to water (direct 4-electron reduction) electrochemically with the rate constant k_1, or to adsorbed hydrogen peroxide ($H_2O_{2,ad}$) with the rate constant k_2 (series 2-electron reduction). $H_2O_{2,ad}$ can be further reduced to water with the rate constant k_3, chemically decomposed on the electrode surface (k_4), and/or desorbed into the electrolyte solution (k_5). Some experimental results suggest that a series pathway via an $(H_2O_2)_{ad}$ intermediate is the most possible pathway. For example, only a very small amount of H_2O_2 could be observed during ORR, and the electron transfer number is close to 4.

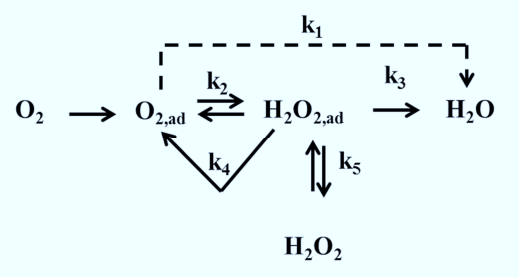

Figure: 1.2 ORR mechanisms on Pt [70]. Reproduced from *J. Electroanal. Chem.* 69 **(1976),** 195.

Pt based ORR electrocatalysts have extensively employed because of their relatively low overpotential and high current density. The electrocatalytic reduction of O_2 on Pt strongly depends on O_2 adsorption energy, the dissociation energy of the O-O bond, and the binding energy of OH on the Pt surface. The electronic structure of the Pt catalyst (Pt d-band vacancy) and the Pt-Pt interatomic distance (geometric effect) can strongly affect these energies [13, 71]. Figure 1.3((a), (b)) shows RRDE measurements on a Pt surface, demonstrates that O_2 reduction on Pt is a significant 4-electron transfer process from O_2 to H_2O in both acid and alkaline aqueous electrolytes. Markovic et al. carried out ORR on different Pt(*hkl*) low-index single crystal electrode, the ORR kinetics on Pt surfaces varies with the crystal plane and electrolyte types [72, 73]. The ORR activity of Pt(*hkl*) in H_2SO_4 (Fig. 1.3(a)) increases in the order of Pt(111) < Pt(100) < Pt(110). Also, the ORR activity of

Pt is significantly higher in H_2SO_4 than KOH electrolyte explaining that the adsorption of anion species also affects the kinetics of ORR on all three surfaces. The ORR activity of Pt(*hkl*) in KOH (Fig. 1.3(b)) increases in the order of Pt(100) < Pt(110) < Pt(111).

The structure sensitive ORR activity also studied on Au(*hkl*) electrode surface by Adzic et al [74]. The typical RDE measurements are shown in Figure 1.3((c), (d)). The ORR activity of Au(*hkl*) in both acidic and alkaline solution increases in the order of Au(111) < Au(110) < Au(100). Au(100) exhibits the highest activity for O_2 reduction in both acid and alkaline electrolytes [74].

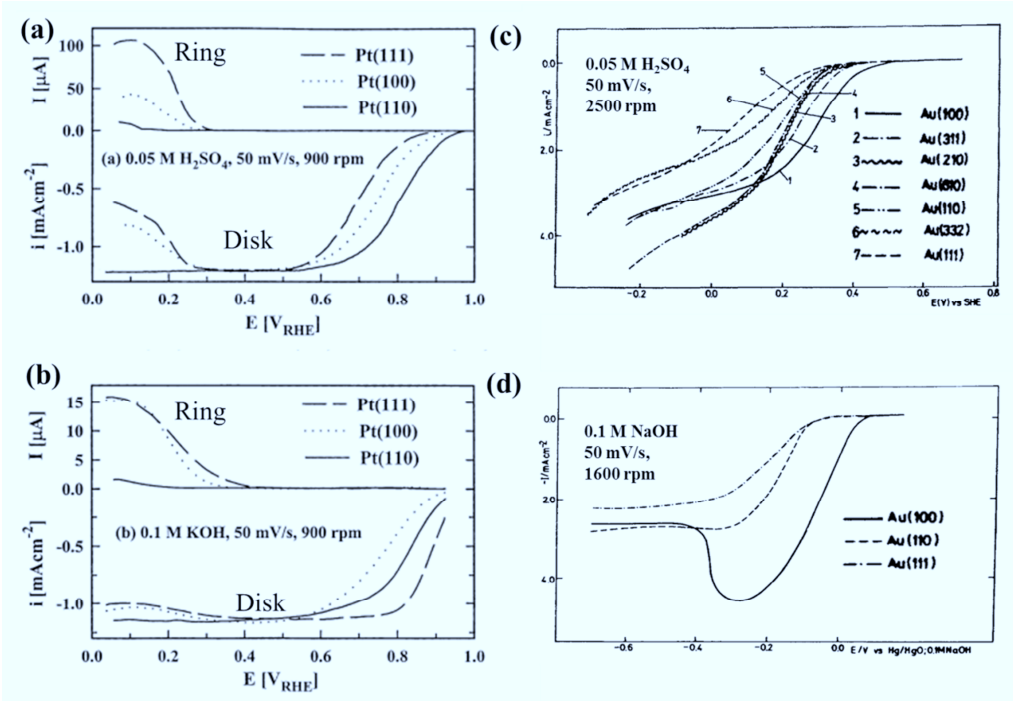

Figure: 1. 3((a), (b)) Disk and ring (IR) currents during O_2 reduction on Pt(*hkl*) (a) in 0.05 M H_2SO_4 [72], (b) in 0.1 M KOH [73]. Reprinted from *J. Phys. Chem.* 99 **(1995),** 3411 and *J. Phys. Chem.*100 **(1996),** 6715. (c) polarization curves for O_2 reduction on Au*(hkl*) in 0.05 M H_2SO_4, (d) in 0.1 M NaOH solution. Reproduced from *Mate. Chem. Phys.* 22 **(1989)**, 349 [74].

The results given above are the direct evidences for supporting the sensitivity of ORR to the surface structure. A low activity of Pt(111) may originate from strong adsorption of (bi)sulfate anion on (111) plane: (bi)sulfate anion is weakly solvated leading to direct chemical bonding with the metal surfaces [75]. It should be noted that although bisulfate adsorption on Pt(*hkl*) surfaces inhibits the reduction of molecular O_2, probably by blocking

the initial adsorption of O_2, it does not affect the reaction pathway, since no H_2O_2 is detected on the ring electrode for any of the surfaces in the kinetically controlled potential region. The Pt (*hkl*) in alkaline system shows, the potential range where O_2 reduction is under combined kinetic-diffusion control (E > 0.75 V), the ORR activity increases in the order of Pt(100) < Pt(110) < Pt(111). It may result from the structure-sensitive adsorption of OH_{ad} species; i. e. the (111) surface has the lowest coverage by OH_{ad} and weakest Pt-OH_{ad} interaction [72-75].

The surface structure sensitivity of ORR on Au(*hkl*) was also attributed to the adsorption of anion is widely studied [54, 55], a critical role of adsorbed OH was proposed, which was different from Pt surface [72-75]. Prieto et al. suggested that the surface structure sensitivity of ORR on Au(*hkl*) can be ascribed as the different adsorption properties of HO_2^-. The surface structure sensitivity of ORR is related to the sensitivity of adsorption of anions, reactant or intermediates [76]. These results clearly demonstrate that each crystallographic orientation gives an electrode surface with distinct electrochemical properties, and that meaningful study of O_2 reduction on Au can be done only with single crystal electrodes.

Theoretical calculations on O and OH binding energy on several metals (Fig. 1.4) have predicted that Pt have the highest catalytic activity among other metals in the order of Pt > Pd > Ir > Rh, which is in agreement with the experimental results [13, 77, 78]. Metals with a somewhat lower oxygen binding energy than Pt should have a higher rate of oxygen reduction. DFT calculations have shown that Pt alloys with, for example, Ni, Co, Fe, and Cr (where Pt will segregate to the surface) have smaller oxygen binding energies than pure Pt [77, 79]. The OH binding energies are not reduced to the same extent on these surfaces. On a Pt monolayer over a monolayer of Ni, Co, or Fe on a Pt substrate, DFT calculations give O and OH binding energies of (ΔE_{OH}, ΔE_O) (1.15 eV, 1.89 eV), (1.06 eV, 2.00 eV), and (0.85 eV, 2.06 eV), respectively. This is to be compared to the adsorption on a pure Pt surface: (ΔE_{OH}, ΔE_O) (1.05 eV, 1.57 eV). Yu et al. [77, 79] have shown that a Pt skin on top of Pt_3Co(111) has an oxygen binding energy that is 0.38 eV less than that on pure Pt(111). It is not just the oxygen binding energy that determines the activity of a surface for oxygen reduction; the OH bonding energy is also important. It can be observed in Figure 1.4 that the O and OH binding energies are roughly linearly correlated for the elemental surfaces. There are, however, ample possibilities for finding new systems where bonding of O and OH do not follow the same correlation and could lead to completely new catalysts for this important reaction [77].

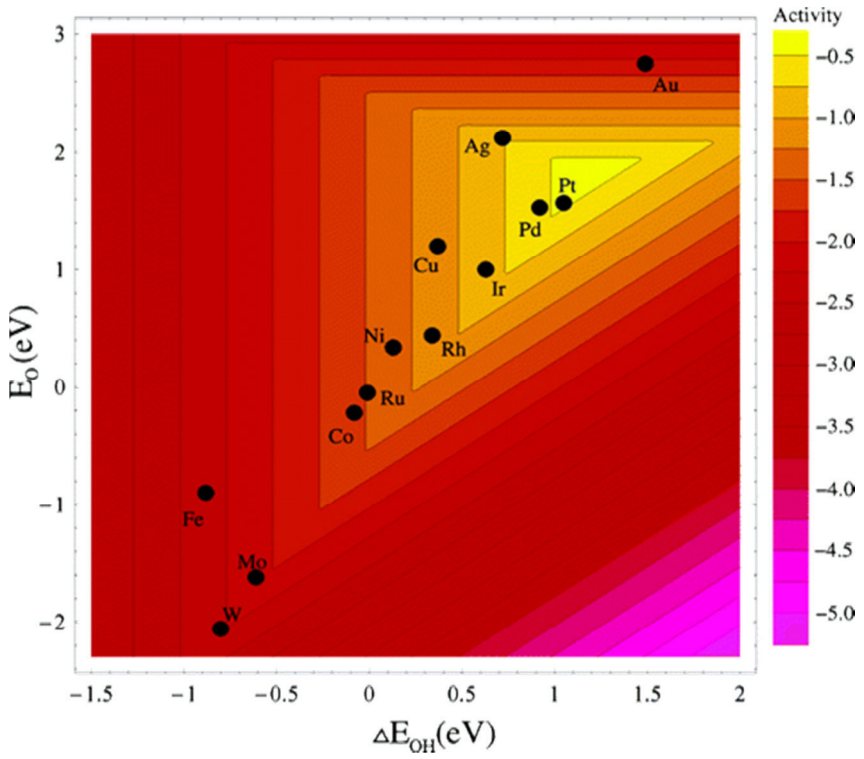

Figure: 1.4 Trends in O_2 reduction activity plotted as a function of the O and OH binding energy [77]. Reprinted from *J. Phys. Chem. B* 108 **(2004),** 17886.

1.3.1.3 ORR on Metal alloys

As explained above the ORR activity of Pt single crystal surfaces is highly dependent on surface orientation and composition, which may affect by a number of factors such as alloy nature and its preparation procedure, and environmental conditions such as electrochemical potential and pH. A more active catalyst would have a higher current density at a given potential. Apart from Pt, only Au and Ir are thermodynamically stable in the bulk metallic format potentials greater than 0.9 V. There are notable examples whereby non-precious metals have been stabilised in non-metallic forms, such as metal organic complexes, enzymes and oxides or N-functionalised graphene-based materials [62, 80]. Although they can exhibit activity close to or even better than that of Pt, they still suffer from poor stability especially in acidic solution, or a low density of active sites. Given the above challenges, most research efforts in relation to ORR catalysis are focussed upon improving the activity of Pt. This is achieved by forming a structure with a Pt over-layer on a core with a different composition. Typically, the core consists of Pt alloyed with a less noble late transition 3d metal such as Fe, Co, Ni, and Cu, although it might contain other Pt group metals such as Pd

or Au [23-56]. The Pt over layer provides kinetic stability against the dissolution of the less noble solute component. At the same time, the electronic structure of the Pt surface is modified by the underlying alloy, resulting in improved ORR activity [81].

The relationship between bulk and surface composition of Pt-transition metal alloy catalysts has been discussed both in theoretical and experimental reports. On the subject of the Pt alloy catalysts, considerable progress has been made on PtM (M=Fe, Co, Ni, Cu, Cr, etc.) [23-56] alloys, which has been proved experimentally to have higher catalytic activity than pure Pt [81], as shown in Figure 1.5. The enhanced ORR activity is explainable by the change in electronic structure (the increased Pt d-band vacancy) and in geometric effect (Pt-Pt interatomic distance). Alloying causes a lattice contraction, leading to a more favourable Pt-Pt distance for the dissociative adsorption of O_2. After alloying d-band vacancy could be increased, producing a strong metal-O_2 interaction than weakening the O-O bonds [13, 27, 32, and 69].

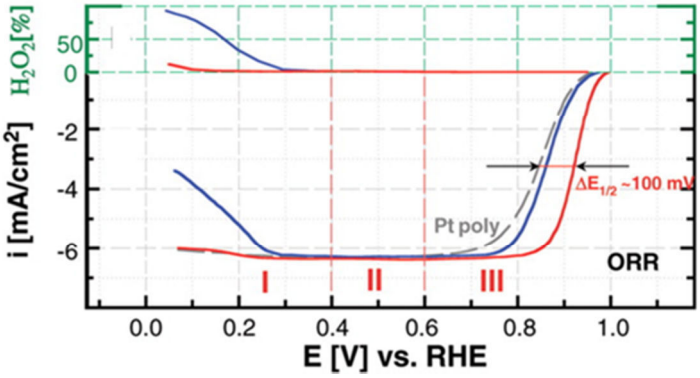

Figure: 1.5 Oxygen reduction and hydrogen peroxide production on $Pt_3Ni(111)$ (red curve), Pt(111) (blue curve), and polycrystalline Pt (gray curve) surfaces. The arrows are showing the positive potential shift of 100 mV in electrode half-potential (ΔE_{112}) between ORR polarization curves measured on Pt-poly and $Pt_3Ni(111)$ surfaces. I, II, and III represent potential region of H_{ad} adsorption/desorption processes, double-layer region, and region of OH_{ad} layer formation, respectively [81]. Reprodcued from *Science*, 315 **(2007),** 493-497.

Stamekovic et al. [27] established the relationship between the d-band center and ORR activity (Fig. 1.6) on (a) Pt-skin (see inset in Fig. 1.6(a)) and (b) Pt-skeleton (see inset Fig. 1.6(b)) forms on different Pt_3M alloys to evaluate the efficient and stable metal alloys for ORR. Two important differences between the Pt-skeleton and Pt-skin layers are (1) the

morphology of the Pt surface atoms is different, that is, the Pt-skeleton surface is more corrugated; and (2) Pt-skin surface possess oscillating concentration profle, in the case of the Pt-skeleton surface, a bulk-like alloy concentration profle is present up to the subsurface atomic layer [27].

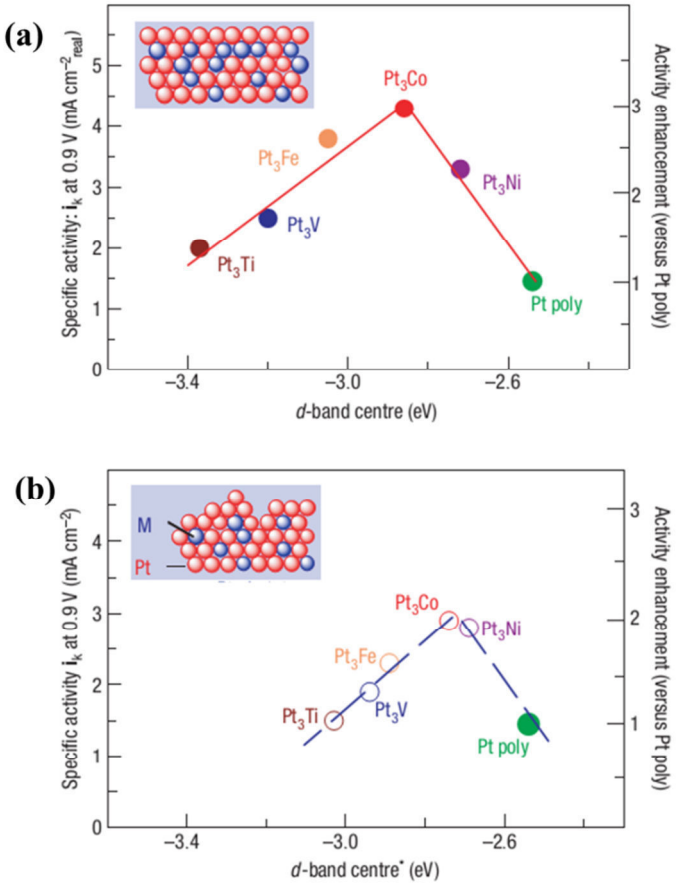

Figure: 1.6 Relationships between the catalytic properties and electronic structure of Pt_3M alloys. Relationships between experimentally measured specific activity for the ORR on Pt_3M surfaces in 0.1 M $HClO_4$ at 333K versus the d-band centre position for the Pt-skin (a) and Pt-skeleton (b) surfaces. (b) Shows the d-band centre values* (* denotes in UHV condition), which may deviate in the electrochemical environment due to dissolution of non-Pt atoms [27]. Reprodcued from *Nature Mater.,* 6 **(2007)**, 241.

They have studied the cyclic Voltammogram (CV) of Pt skin and Pt skeleton surfaces, the fractional surface coverages for the adsorption of underpotentially deposited hydrogen and hydroxyl species ($2H_2O \rightarrow OH_{ad} + H_3O^+ + e^-$) and observed that, on the Pt-skin surface there is a clearly discernible positive shift in OH_{ad} formation (E > 0.7 V) relative to pure Pt,

whereas the onset of OH_{ad} adsorption on the Pt-skeleton surface falls in between the two. In agreement with the onset of OH_{ad} adsorption, the oxide reduction peak obtained in the cathodic sweep for the Pt-skeleton surface lies between the one for pure Pt and the Pt skin, confirming that the OH_{ad} chemisorption energy increases as the d-band centre moves closer to the Fermi level, that is, the decrease in fractional coverage by OH_{ad} follows the same trend: Θ_{OH}-skin < Θ_{OH}-skeleton < Θ_{OH}-Pt. In accordance with the adsorption processes, the activity of the ORR increases in the order Pt < Pt-skeleton < Pt-skin.

The volcano-type relation has presented with Pt_3Co at the maximum activity for both surfaces. When the d-band center is too close to the Fermi level (i.e. metals surfaces binds too strongly with O_2 and ORR intermediates), the catalytic activity is restricted by the free surface active site availability while the ORR is difficult to proceed when the d-band center is too far from the Fermi level (i.e. metals surfaces binds too weakly with O_2 and ORR intermediates) [27]. Therefore, an effective catalyst must be well-balanced between those two opposing effects. However, it should be underlined that the catalytic activity is not only dependent on the d-band center; it also depends on the morphology of the alloy surface (i.e. geometrical effect) [13, 27]. Unfortunately, dissolution of the transition metal alloys in the PtM catalysts is a major drawback because these transition metals are electrochemically soluble at a potential range between 0.3 to 1.0 V vs. SHE in low pH media [22, 71].

1.3.2 Non-precious metal or metal oxide/nitride/carbide catalysts for ORR

Although Pt is the best ORR catalyst, it is not possible to utilize for commercial applications. As a result of this, the worldwide researchers were searching for an alternative electrocatalyst for ORR based on nonprecious metals [8, 38, 82-88] their alloys, metal oxides [89-91], metal nitrides [57, 91], metal oxynitrides [92, 93], metal carbides [57, 94, 95]. There are still some significant draw-backs exist for noncarbon-based supports. (i) the electronic conductivity, almost all the noncarbon materials have lower electronic conductivity when compared to carbon materials (ii) solubility, majority of the noncarbon support materials have higher solubility than carbon materials in aqueous environments, especially in the acidic environment (iii) electrochemical and chemical stability, some of the noncarbon support materials, such as WC, are easier to oxidize at O_2 electrode potentials than carbon materials, leading to failure (iv) thermal stability, some of the noncarbon support materials such as conductive polymers are not stable at higher temperatures, that is, >100^{o}C and (v) low surface area, it seems that almost all noncarbon supports have lower surface area when compared to

carbon materials [91]. Large surface area is often a necessary factor for efficient FC catalyst, determining the catalyst activity. Therefore, to make practically feasible noncarbon supported Pt-based catalysts, there are some requirements such as electronic conductivity, solubility, chemical/electrochemical and thermal stability, and surface area needed for the material improvements [91].

1.3.2.1 Metal Oxides

The oxide-based ORR catalysts are potential substitutes for Pt. There are numerously conductive or semi-conductive oxides have been studied as catalyst support materials or as secondary supports to modify and promote the catalyst support for PEM FCs, including indium tin oxide (ITO) [96], TiO_x [97], WO_x [98], IrO_2 [99], SnO_2 [100], Fe_3O_4 [101], Cu_2O [102], MnO_2 [103], Co_3O [104, 105], etc. It has demonstrated that these metal oxides shown higher catalytic activity [98, 99, 106-108] and durability [109, 110] of PEMFC catalysts. Although many different oxide materials have examined in these studies, it is not possible to extract absolute ORR activities referenced to either oxide surface area (i.e., specific activity) or mass (i.e., mass activity).

Masuda et al. [111] investigated the Pt decorated CeO_x nano composites, in which CeO_x as co-catalyst to promote ORR and to reduce the amount of Pt. Figure 1.7 shows that the ORR current at the Pt−CeO_x/C electrode started to flow at a more positive potential than that at the Pt/C electrode by 50−80 mV, showing the enhancement of the ORR rate by the addition of CeO_x to Pt. The onset potential of ORR at the Pt/C electrode coincides with the Pt oxide reduction potential observed in the Ar-saturated solution, suggesting that the Pt surface of the Pt/C was partially covered with Pt oxide near the onset of ORR. On the other hand, Pt oxide formation seemed to be inhibited at the Pt−CeO_x/C electrode. Thus, it appears that the enhancement of ORR at the Pt−CeO_x/C is attributed to the suppression of Pt oxide formation [100]. It was demonstrated that the role of CeO_x in the enhancement of the ORR rate at the Pt/C catalyst was clarified by in situ X-ray absorption fine structure (XAFS) measurements at the Pt L_3 and Ce L_3 edges of the Pt−CeO_x/C catalyst as well as at the Pt L_3 edge of the conventional Pt/C catalyst in O_2-saturated H_2SO_4 solution. It was shown that Pt oxide formation was suppressed by the presence of CeOx as Ce^{3+} was oxidized to Ce^{4+} instead of Pt at the Pt oxide formation potential. The inhibition of Pt oxide formation is considered to be the primary factor for enhancement of the ORR rate because ORR activity of the Pt oxide surface is much lower than that at the bare Pt surface [111].

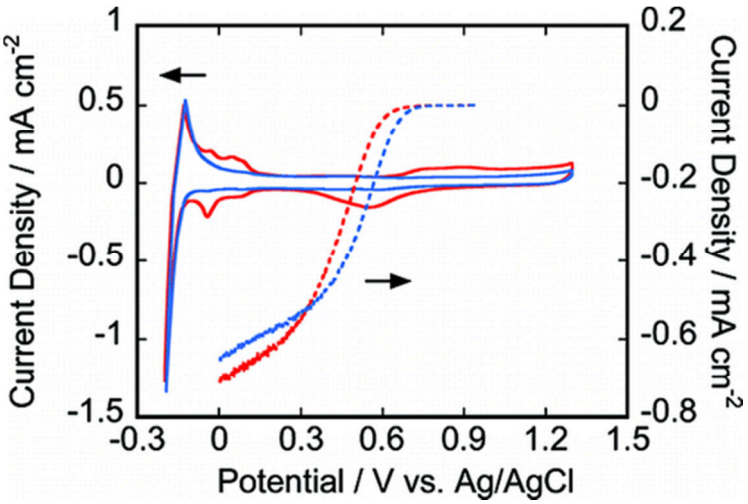

Figure: 1.7 CVs (solid line) and linear sweep voltammograms (LSVs) (broken line) of the Pt/C (red line) and Pt−CeO_x/C (blue line) drop-cast glassy carbon electrodes measured in a 0.5 M H_2SO_4 solution saturated with Ar (CVs) and O_2 (LSVs) with a scan rate of 50 mV/s. LSVs in the O_2-saturated solution were obtained using a rotating disk electrode configuration at 2000 rpm. Reproduced from *J. Phys. Chem. C* 116 **(2012)**, 10098 [111].

1.3.2.2 Metal nitrides and oxy-nitrides

Transition-metal nitrides and oxynitrides are appropriate materials for catalysis applications, some of which possess catalytic activity that are alike to those of noble metals like Pd and Pt [57, 112-114]. Because of its higher electrical conductivity and prominent oxidation and corrosion resistances, [115, 116] transition metal nitrides should be an efficient catalyst for PEMFCs, exclusively for high temperature PEMFCs. The formation of nitrides favourably modifies the catalyst electronic structure such that the contraction of d-bands in group 4–6 nitrides results in a greater electron density near Fermi level. It facilitates the donation of electrons to adsorbates such as O_2 [92, 117]. The ORR activity of $Co_xMo_{1-x}O_yN_z$/C is (x=0.0, 0.25, 0.5, and 0.75) [92] shown in Figure.1.8. The bimetallic oxynitride $Co_{0.50}Mo_{0.50}O_yN_z$ had better activity than binary Mo_2N and CoO, which suggests that Co substitution into Mo_2N reduced its reduced it overpotential against ORR by ca. 0.2 V. The number of transferred electrons calculated to be n=4 by Koutecky-Levich plot. It is suggested that strategies for tuning the metal oxidation states within the oxynitride phase are likely to lead to further enhancements in ORR activity of $Co_xMo_{1-x}O_yN_z$/C.

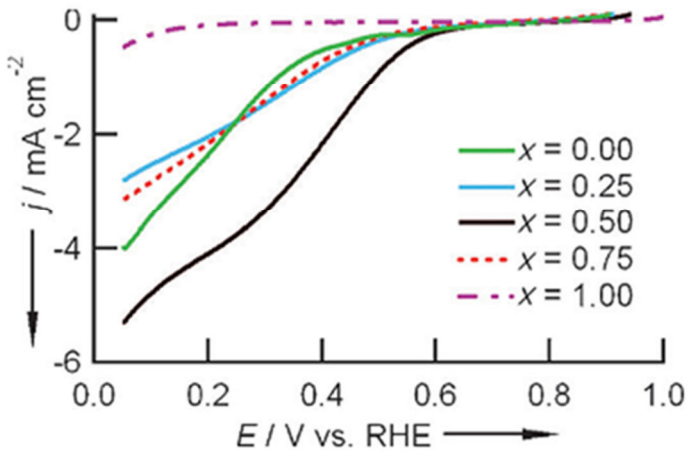

Figure: 1.8 RDE curves of $Co_xMo_{1-x}O_yN_z/C$ with different Co/Mo ratios synthesized at 823 K, measured in O_2-saturated 0.1 M $HClO_4$ [92]. Reproduced from *Angew. Chem. Int. Ed.* 52 (**2013)**, 10753.

1.3.2.3 Metal carbides

Carbides are compounds composed of carbon and a less electronegative element. According to chemical bonding types, all carbides exhibit some level of covalent character. There are several types of carbides such as Boron carbide (B_4C), Titanium carbide (TiC), Silicon carbide (SiC) and Tungsten carbide (WC) has studied as the electrocatalyst for ORR [91]. Since the 1970s [118] it has shown that the transition metal carbides (TMCs), particularly WC, demonstrated Pt-like catalytic properties [119] because, near the Fermi level, the electronic density of states of WC resembles that of noble metal Pt [118]. During synthesis or post-treatments of metal carbides, at their surface, the chemical composition and the catalytic properties can be easily modified [120]. As shown in Fig.1.9 the W_2C nanocrystals have no ORR activity in acidic solution (Figure 1.9(i)). This means that the pure W_2C could not be used as electrocatalysts for ORR. However, the addition of W_2C nanocrystals with Pt/C significantly improved the ORR activity (Figure 1.9(iii)), which is better than that on pure Pt/C electrocatalysts (Figure 1.9(ii)). The ORR started at 1.0 V on the W_2C/Pt/C electrode instead of the 0.88 V on Pt/C electrode [121, 122]. It is due to the unique properties of W_2C [123], such as their stability in acid solutions at anodic potentials [107], their selectivity [124], and specifically strong resistance to catalytic poisons. However, the

mechanism of the ORR activity enhancement induced by adding W_2C to Pt is not yet clear. Experimental results show that most possibility of ORR enhancement is due to the synergistic effect between tungsten carbide nanoparticles and Pt at the interface [122].

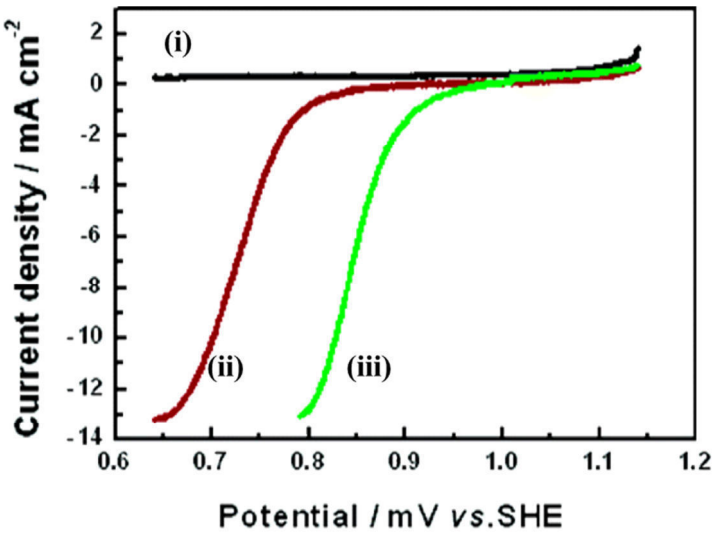

Figure: 1.9 Linear sweep curves of O_2 reduction on different catalysts in O_2 saturated 0.5 M H_2SO_4 solution at 25 °C: (i) 80 µg of W_2C; (ii) 80 µg of Pt; (iii) 40 µg of Pt + 80 µg of W_2C; sweep rate, 2 mV s^{-1} [122]. Reproduced from *J. Phys. Chem. B* 109 (**2005**), 22705.

1.3.3 Carbon and N-, B-doped carbon materials for ORR

Carbon based materials such as nanotubes and graphene are currently at the forefront of materials research because they show outstanding electrocatalytic activity due to their unique electrical and chemical properties. The doping of these carbon nanostructures with the heteroatom like N, B, P, S and I [125-132] have drawn much attention, when a heteroatom bonded with a carbon framework, it introduces a defect nearby sites due to difference in bond length and atomic size, and thereby can induces uneven charge distribution. Moreover, usually the heteroatom is covalently bonded with a carbon framework; hence its catalytic activity will not languish even for long-time operation. Dai and co-workers experimentally reported that N doped carbon nanotube arrays possess high electrocatalytic activity for ORR [127]. Also, vast of experimental results has demonstrated that the co-doping of B and N with carbon [133-140] (Fig. 1.10) has enhanced ORR activity.

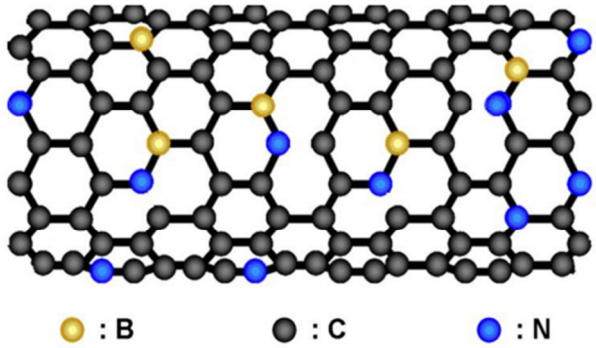

Figure: 1.10 Schematic of B and N co doped carbon nanotube

As shown in Figure 1.11, of the four electrodes the vertically aligned B and N doped carbon (VA-BCN) showed highest ORR activity than VA carbon nanotubes (VACNT), VA N doped CNT (VA-NCNT) and VA B doped CNT (VA-BCNT). Therefore, the N–B doped carbon alloys can be considered as a good candidate for an efficient and cheap ORR catalyst. In fact, N and B co-doped carbon materials have shown better durability than that of commercial Pt/C catalysts [135-138]. Unfortunately, the mechanism of ORR and even clear identification of the ORR active sites in the N–B doped carbon alloys remain elusive.

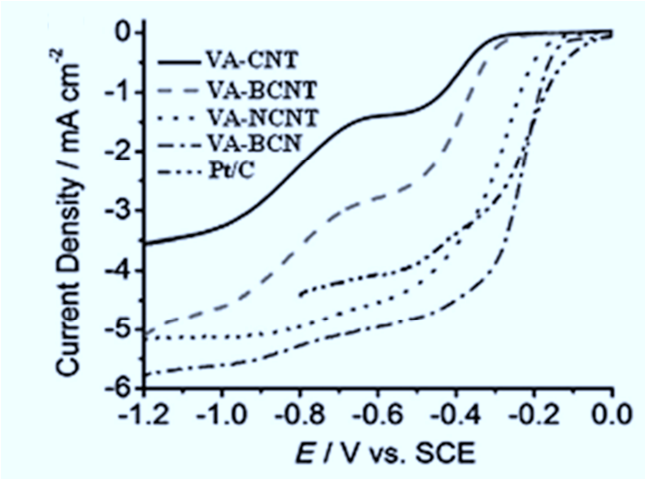

Figure: 1.11 Linear sweep voltammetry curves of various electrodes in O_2 saturated 0.1 M KOH electrolyte at a scan rate of 10 mV sec^{-1} and a rotation rate of 1000 rpm [140]. Reproduced from *Angew. Chem. Int. Ed.*, 50 (**2011**), 11756.

In the case of N doped graphene clusters it was demonstrated that the active sites for ORR are neighbouring C atoms positioned nearby graphite as N atom [135]. In the case of

the N–B doped graphene it has demonstrated that the ORR active sites are boratabenzene-like B atoms located near the graphite-like N atoms [130, 141]. In both cases, the graphite-like N atom near the zigzag edge activates the neighbouring C and B atoms. However, namely pyridine-like and pyrrole-like active center (Fig. 1.12) possess electrocatalytic properties for the ORR in the case of N doped graphene clusters $C_{45}NH_{20}$ and $C_{45}NH_{18}$ [137, 141]. In the latter case, the catalytic reaction occurs not at the edge of the finite cluster or one-dimensional carbon nanoribbon, but on the surface of the N doped graphene sheet. It was demonstrated that the catalytic activity of the N-doped graphene monolayer decreases with increase in the local concentration of N atoms [136]. As a result, the N atoms bonded with three C atoms are more active than the N atoms bonded with two carbon atoms [136]. On the other hand, as discussed above; the co-doping of N doped graphene clusters with B atoms promotes their ORR activity [140].

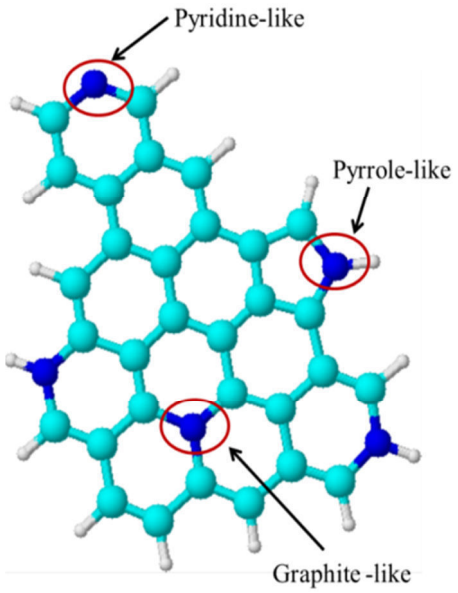

Figure: 1. 12 Local geometry for various nitrogen atoms in graphite. Cyan, blue, and white balls represent C, N, and H atoms, respectively.

Therefore, one can suggest that the ORR activity might be enhanced when all the C atoms in N doped graphene are substituted by B atoms. In the extreme case when all C atoms in graphene are substituted by N and B one can obtain the h-BN monolayer, which has a geometric structure similar to graphene. Recently a promising ‘chemical blowing’ method has been developed for the mass production of BN nanosheets [142]. Such material is

considerably cheaper than Pt and consists of abundant elements [142, 143]. Can h-BN act as a catalyst for ORR? The answer to this question is opened an innovative way for the development of an essentially new class of ORR catalysts, based on traditionally believed inert materials [144, 145].

1.4 Hydrogen production

Hydrogen (H_2) is the cleanest fuel and is considered to be one of the most promising energy carriers. It is currently produced from fossil fuels but must be produced from water for hydrogen to be considered as a fuel. Electrocatalysis of water is the most promising method to produce large amounts of hydrogen from water, hydrogen evolution reaction (HER) [146] and has been investigated drastically. The generation of H_2 from water demonstrates an environmentally responsible, carbon-free alternative route, however, it is challenging to carry out the H_2 evolution reaction (HER, $2H^+ + 2e^- \rightarrow H_2$) without the use of noble metal catalysts [147-151]. The cathode is the crucial part of an electrolyzer where to be HER taking place. The kinetics of the HER is not straightforward due to its reliance on the electrochemical conditions: it consists of simultaneous multiple pathways where the H atoms bound to the catalyst surface because of different surface crystalline facets. The electrochemical potential strongly influences these multiple pathways. According to the two-electron-reaction models, cathodic H_2 evolution in acidic aqueous media is assumed to take place in two steps [150, 152, and 153]: first, the ‘‘discharge step’’ in which an electron transfer to a proton at the catalyst surface on the cathode provides an intermediate state of a H atom bound to an active site (Volmer reaction),

$$H^+_{(aq)} + e^- \rightarrow H_{ads} \tag{1.6}$$

second, the electrochemical desorption step (Heyrovsky reaction),

$$H_{ads} + H^+_{(aq)} + e^- \rightarrow H_{2(g)} \tag{1.7}$$

or the recombination step (Tafel reaction),

$$H_{ads} + H_{ads} \rightarrow H_{2(g)} \tag{1.8}$$

At the electrode surface, the adsorption and removal of H atoms are competitive processes. An effective HER catalyst should have the ultimate exchangeability between binding and releasing of the H atoms. As explained by the volcano plot (Fig. 1.13) in which the activity of H_2 evolution as a function of the metal hydrogen (M–H) bond strength displays an ascending order followed by a descending order, peaking at Pt [154-157]. It has also demonstrating that neither too strong nor too weak binding would favor the overall reaction because it is difficult to remove the product or to adsorb the reactant as a result of strong or weak M-H binding. This volcano plot apparently recommends that the H binding energy (HBE) can be a good descriptor for pinpointing the effective HER electrocatalysts. An efficient HER electrocatalyst should have reduced the overpotential significantly.

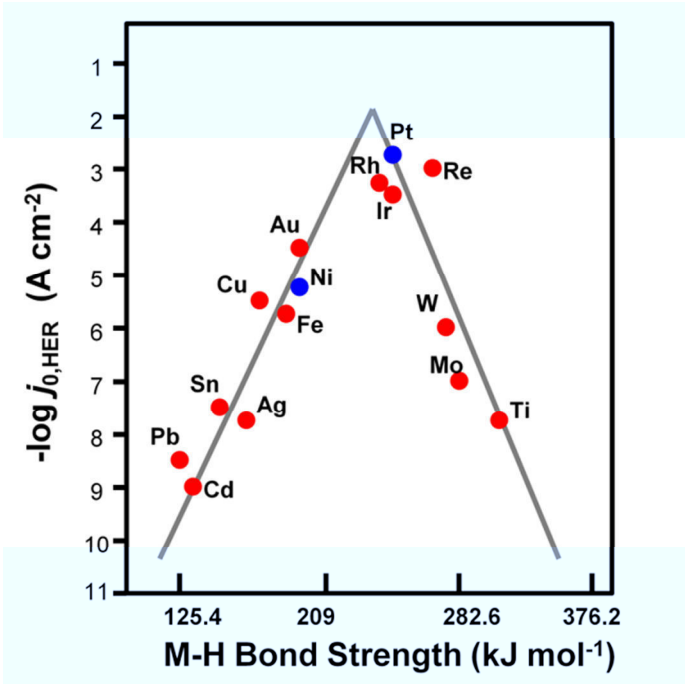

Figure: 1.13 Volcano plot for the H_2 evolution reaction [155, 156]. Reproduced from *J. Electroanal. Chem.*, 39 **(1972),** 163 and *Electrochim. Acta*, 45 **(2000)**, 4075.

1.4.1 Metals and its alloys for HER

An efficient HER catalyst should have a free energy for adsorbing H atom close to $\Delta G_H \sim 0$ [158], which has designated by theoretical models using density functional theory calculations. This concept has ascribed as if the H atom does not efficiently bind to the catalyst or if it forms a strong bond with the catalyst then it would reduce the catalytic

activity due to an inefficient proton–electron-transfer step and H_2 release, respectively [159]. Along with the HBE of the HER catalyst, various types of other factors such as, roughness, conductivity, stability of the catalyst, the attachment of catalysts on electrodes, and charge transfer through the solid–liquid interface can restrict its performance [159]. A commonly used electrocatalyst is Pt metal, owing to its low overpotential (0.02 V at 1 mA cm^{-2}) under acidic conditions [146-150]. Discovery of noble metal free electrocatalyst is the foremost task in front of the development and implementation of HER catalyst. It has found that the first-row transition metals are very efficient owing to their stability, abundance in nature, and low cost to address this challenge. Various types of Ni alloys ought to be demonstrated as an alternative for Pt due to their low cost, high abundance, low overpotential, and stability in alkaline electrolyzers [152, 159-163]. Figure 1.14 displays the HER activity of nanoparticles of Pt, which is known to be a highly active electrocatalyst for the HER in which neither bare Ti foil nor glassy carbon (GC) showed significant HER activity over this range of electrode potentials. The HER overpotentials on Ni_2P nanoparticle films observed at cathodic current densities of 20 and 100 mA cm^{-2} were 130, and 180 mV, respectively. Ni-based catalyst can achieve high productivity and less energy consumption in acidic media [162, 163], however still, there are some significant complications like, reduced corrosion stability in acidic medium [159] for the industrial applications.

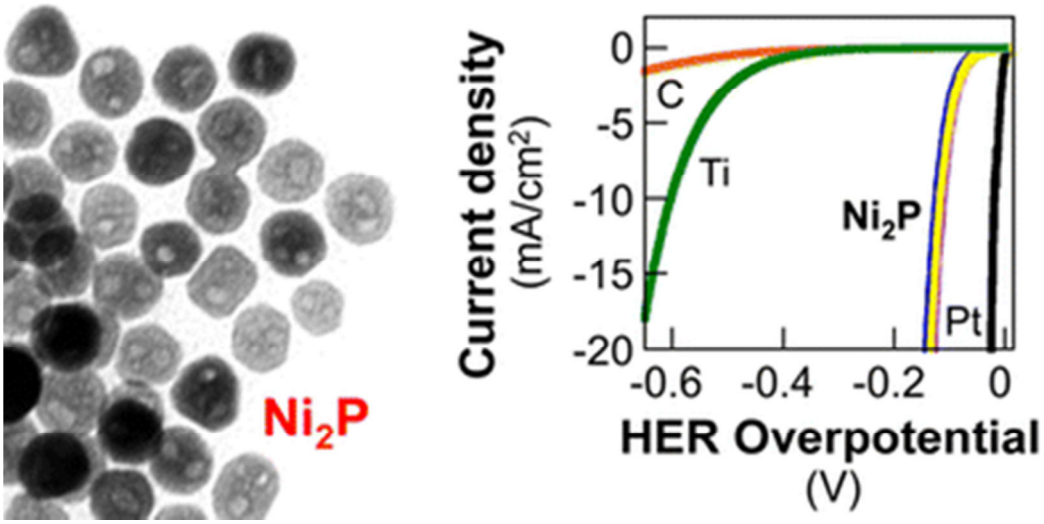

Figure: 1.14 TEM image, Polarization data for three individual Ni_2P electrodes in 0.5 M H_2SO_4, along with glassy carbon, Ti foil, and Pt in 0.5 M H_2SO_4, for comparison [163]. Reproduced from *J. Am. Chem. Soc.,* 135 **(2013)**, 9267.

1.4.2 Transition metal chalcogenides, carbides and nitrides for HER

The above conditions have also been applicable for other non-noble-metal catalysts. Nevertheless, group VI transition metal chalcogenides [164-168], nitrides and carbides [169-171] reveal some general properties, such as corrosion resistance, high stability, high melting point, high mechanical strength, etc., which have attracted much attention during the past few decades in the perspective of their latent applications as electrocatalysts, catalyst supports, lithium-ion battery materials, and solar cells [159].

1.4.2.1 Chalcogenides

Chalcogenide materials such as molybdenum sulfides [158, 164, 165, and 172-174] and tungsten sulfides [175, 176] have also been anticipated as an efficient electrocatalyst for H_2 evolution reaction. Hinnemann et al. described that the HBE of MoS_2 is positioned close to the noble metal group on the volcano plot [174], and this was successively confirmed by experimental results [172, 176] as shown in Fig. 1. 15. The overpotential for HER on both MoS_2 and WS_2 catalysts observed at the cathodic current density of 20 mA cm^{-2} was 100 mV.

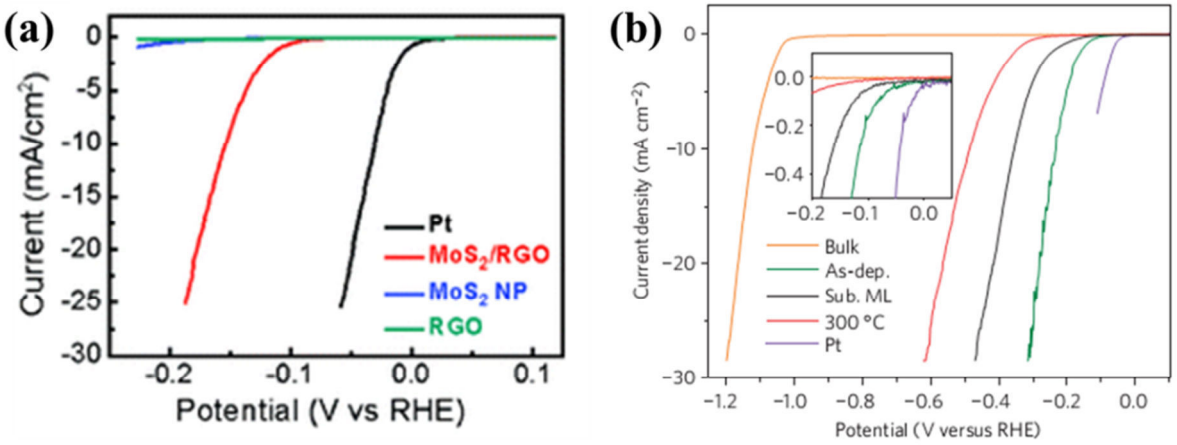

Figure: 1.15 Polarization curves of (A) several MoS_2 catalysts [172] and (B) Polarization curves of bulk and as-exfoliated WS_2 (as-deposited film of 1T phase, sub-monolayer as exfoliated film, and 2H phase after annealing at 300^{o}C) along with those corresponding to Pt nanoparticles and bulk WS_2 powder for comparison [176]. Reproduced from *J. Am. Chem. Soc.*, 133 **(2012)**, 7296 and *Nat. Mater.,* 12 **(2013)**, 850.

Many of experimental and theoretical results demonstrate that the metallic like sulfur edges of 2H XS_2 crystals are electro catalytically active [173, 174 and 177]. The strain can significantly influence the free energy of adsorption of H_2 on the surface of the WS_2 due to the zigzag like local lattice distortions at the edge, and facilitate HER. The highest concentration of exposed edges has directed to evaluate the XS_2 nanoparticles or complexes as electrocatalysts for H_2 evolution [178]. However, these XS_2 materials still suffering from overpotential of 200 to 100 mV vs. SHE.

1.4.2.2 Carbides and Nitrides

Transition metal carbides (TMC) and nitrides often called as interstitial alloys. It is obvious that the addition of carbon or nitrogen interstitial atoms by charge transfer processes and/or consequent structural modification would modify the electronic structure of metal hosts. One of the primary interests in the application of these interstitial alloys is as alternative catalysts to replace the group VIII noble metals especially in electrocatalysis [158]. They show remarkable catalytic activities, which have been attributed to their distinct electronic structure, induced by the presence of non-metal elements in the metal lattice. The carbides and nitrides of Mo and W can adsorb H atoms and promote the H_2 evolution [158]. In the case of tungsten carbide (WC), this phenomenon has been explained by the filling of the d-states at the Fermi level of W by the alloying carbon [178]. The catalytic activity of metal carbides and nitrides has determined by the surface structure and chemical composition. Metal-Nitrogen (M-N) bond can form by the modification of the density of states of the d-band structure of metal. The resulting smaller deficiency in the d-band occupation of the metal causes the nitride surface to exhibit an electron donating ability [158]. Accordingly, for reactions involving the donation of d electrons, such as the HER, metal nitrides would have a higher catalytic activity than the parent metals. In general HER on metal carbides and nitrides is a relatively slow process compared to Pt because at low pH, which undergoes continuous oxidation and is covered by an insulating oxide layer, it can inhibit any electrocatalytic activity. To date, electrodes such as WC, W_2C, Mo_2C, NiMo nitride and Mo_2C–Mo_2N composites have exhibited good HER efficiencies [159]. It has demonstrated that WC or W_2C and Mo_2C are much more active as HER catalysts than other carbides and all nitride materials, whereas the electrochemical stability of metal carbides is of high concern for long-term operation [178]. It has the excellent resistance to the oxidation at low pH. Nevertheless, the reported HER

catalytic activities of WC and W_2C, expressed in terms of exchange current density (i_o), are still 2−3 orders of magnitude below many Pt-group metals [178] as shown in volcano plot Fig. 1.16. It shows the exchange current density values determined from the Tafel plots for these surfaces plotted versus the corresponding DFT-calculated HBE values. The importance of this finding is that other metal-modified carbide surfaces might be effectively screened for HER activity based on their DFT-calculated HBE values.

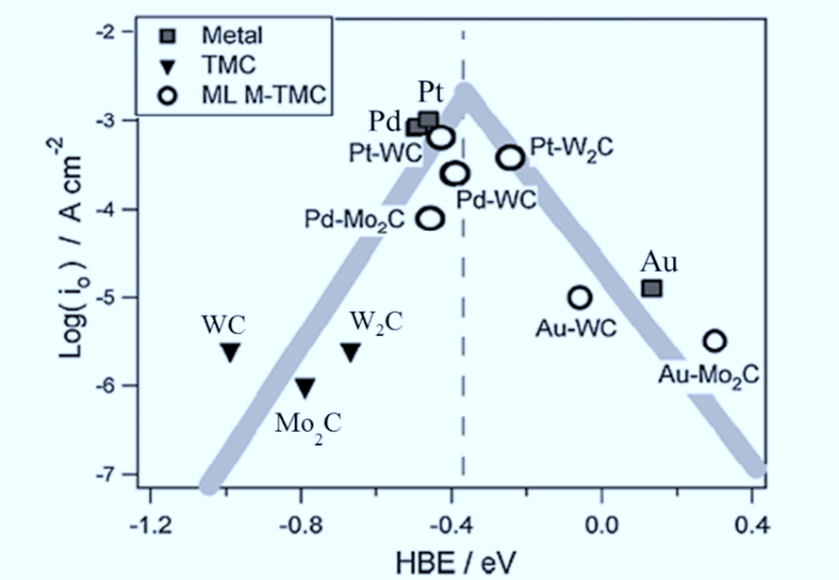

Figure: 1.16 Volcano relationships between exchange current density and the HBE for metal modified carbide surfaces [179]. Reproduced from *J. Am. Chem. Soc.,* 134 **(2012),** 3025.

1.4.3. Silicon based materials for HER

Si is an attractive candidate for a tandem-system photocathode, because it is earth-abundant and relatively cathodically stable. Si also has the appropriate band energetics to serve as the photocathode for water-splitting [180-184]. The Si surface, however, has poor kinetics for the HER and requires a catalyst to achieve efficient solar energy conversion [185]. There are several accounts in the literature of Si-based photocathodes, but most devices have relied on noble metal catalysts such as Pt or Pd, [186-195] that are too rare and expensive to be viable options for a low-cost water-splitting device. Masuda et al. (Figure 1.17) investigated in detail the construction processes of organic monolayers with viologen moiety, not only with a monoviologen layer but also with multiviologen layers, on n-and p-type

Si(111) electrodes and the electrochemical characteristics of the modified n- and p-Si(111) electrodes in the dark and under illumination, respectively. Electrochemical HER rates in the dark and under illumination were significantly enhanced by the Pt deposition. HER rate increased with the increase of the number of viologen/Pt layers, showing that all attached viologen moieties and Pt particles served as electron mediator and catalyst for HER, respectively [196].

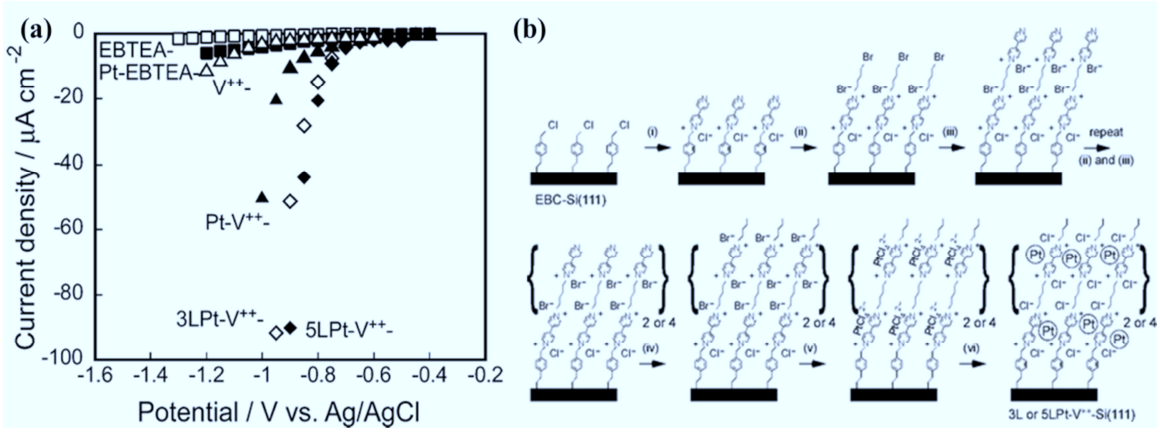

Figure: 1.17(a) Steady-state I−V curves of the n-type EBTEA− (empty rectangle), Pt−EBTEA− (filled rectangle), V^{2+}− (empty triangle), Pt−V^{2+}− (filled triangle), 3L Pt−V^{2+}− (empty diamond), and 5L-Pt−V^{2+}−Si(111) (filled diamond) electrodes in the dark in 0.1 M Na_2SO_4 aqueous solution [196]. (b) Steps for Construction of a Multiviologen layer on H−Si(111) (V^{2+}−Si(111)) and deposition of Pt (Pt−V^{2+}−Si(111)). Reproduced from *J. Phys. Chem. C* 112 **(2008)**, 10923.

Recently, Si wire arrays have attracted attention for solar-energy-conversion applications, because the use of wire arrays allows light absorption and charge-carrier collection, facilitating the use of readily grown, relatively low diffusion-length material while still offering the potential for high energy-conversion efficiencies [197-203]. Lewis and coworkers fabricated Pt film decorated n^+p-Si microwire arrays, in which the surfaces of the p-type Si microwires were heavily doped with phosphorus. This hetero structure was capable of increasing the band bending, which would otherwise be unobtainable in a typical semi-conductor–liquid junction, thus increasing the photovoltage up to 0.54 V [203]. On the other hand, sluggish H_2 evolution reaction (HER) kinetics on the Si surface has led to an extensive search for highly active, non-Pt based electrocatalysts.

1.5 Boron Nitride

The h-BN lattice has a layered hexagonal structure that is very similar to graphite. The planar networks of B_3N_3 hexagons are regularly stacked on top of each other [144]. B–N bonding has a partial ionic character due to this the B atoms in one layer are located on top of the N atoms of the neighboring layers and vice versa [145]. In graphite, however, layers are shifted with respect to each other, thus C atoms in one layer are located on middle top of the hexagonal ring in the neighboring layers. Both graphite and h-BN materials are strongly bonded within the layers and has the week interaction between the layers. In spite of similarities in structures, the physical and chemical properties of graphite and h-BN are very different [144]. Graphite is black in color and possesses electron conductivity. Whereas h-BN is a white color dielectric material with a wide band gap of 5–6 eV and it has thermal properties, such as thermal stability, thermal conduction, and thermal transport, and chemical inertness with respect to less dissolution and chemical reactivity [210-212]. It is unlikely that O_2 and other ORR intermediates can be adsorbed on the h-BN surface. It is even more unlikely that O_2 could activate on such a support [144].

1.5.1 Electron tunneling properties

A FC cathode catalyst must provide an electron transport to the active sites of the ORR. As a result of its dielectric properties, it is impossible to provide an electron transport. These are the main reasons why h-BN has never considered as an ORR catalyst for FCs. However, the low-dimensional h-BN systems, such as h-BN monolayers and h-BN nanoribbons have the significantly different electronic properties, compare to h-BN bulk. Recently, it was shown, that the h-BN nanoribbons become semiconducting due to doping-like conducting edge states and vacancy defects [213]. The band gap in an h-BN monolayer can be considerably reduced by vacancy and impurity defects [213, 214] or by decorating a BN sheet with H atoms [215]. Recently, Brintnell with colleagues demonstrated an electron tunneling effect through h-BN sheets deposited on a gold substrate [216] as shown in Fig. 1.18. Moreover, it was demonstrated experimentally that an h-BN monolayer deposited on the transition metal support can be a conductor under certain conditions [217].

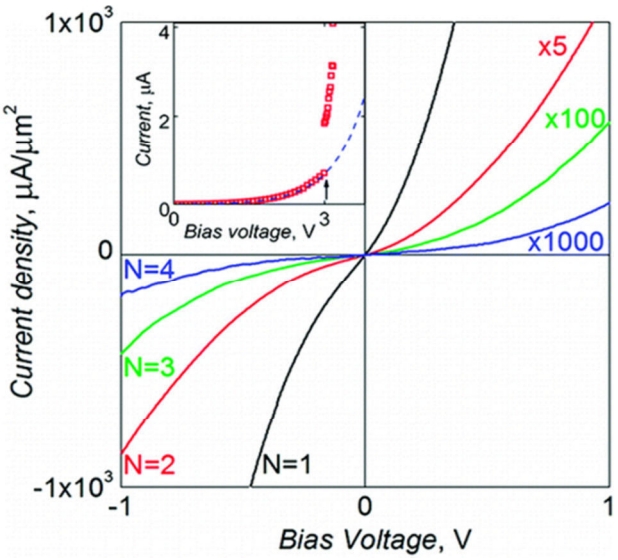

Figure: 1.18 Characteristic I–V curves for graphite/BN/graphite devices with different thicknesses of BN insulating layer: black curve, monolayer of BN; red, bilayer; green, triple layer; and blue, quadruple layer. Note the different scale for the four curves. Current was normalized by the realistic area of the tunnelling barrier, which ranged 2–10 μm^2 depending on the particular device. The inset shows a typical I–V curve where a breakdown in the BN is observed at +3 V, the thickness of the flake is 4 layers of BN (1.3 nm). The dotted line indicates the continuation of the exponential dependence [216]. Reproduced from *Nano Lett.*, 12 **(2012),** 1707.

1.5.2 Possibility of CO oxidation

Additionally, it can also act as an electrocatalyst for CO oxidation [218, 219] and CO_2 capture [220]. Gao et al. theoretically studied the CO oxidation reaction on a free and h-BN supported gold atom [218] as shown in Figure 1.19. The pristine h-BN surface and the h-BN surfaces with boron and nitrogen vacancies have been considered. They have found that O_2 binds stronger than CO on Au/h-BN and Au/VN@h-BN support, but weaker than CO on Au and VN@h-BN adsorption centers. The excess of the positive or negative charge on Au can considerably change its catalytic properties and enhance the activation of the adsorbed O_2. Co-adsorption of CO and O_2 on Au, Au/VN@h-BN, and Au/VB@h-BN results in an additional charge transfer to O_2. These finding leads to a very important conclusion that Au supported on the h-BN surface (pristine or defected) cannot be considered as a pseudo-free

atom [218]. The support effects have to be taken into account, even when the interaction of Au with the support is weak.

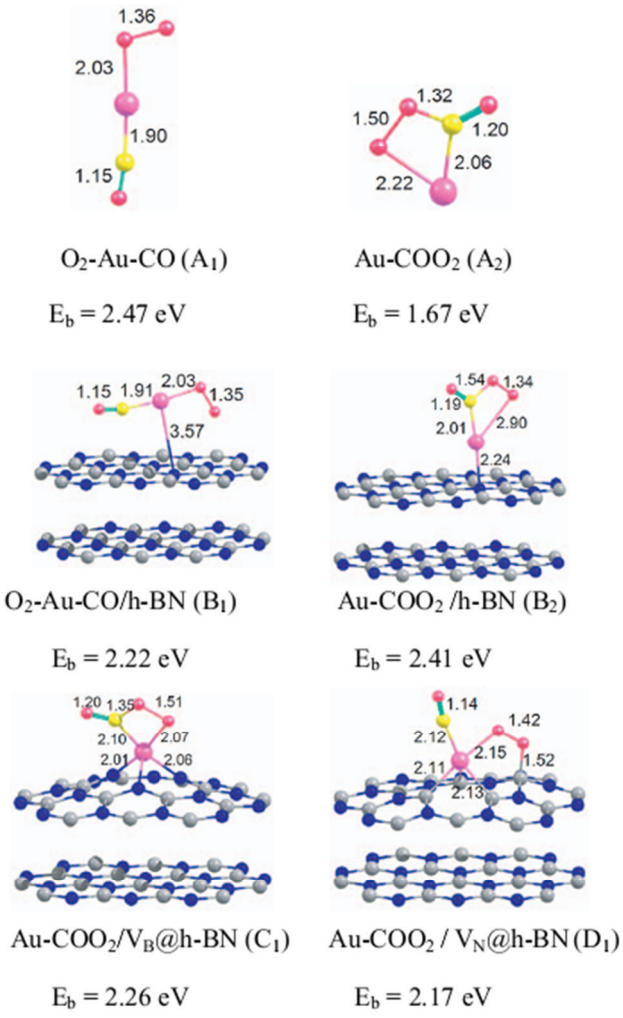

Figure: 1.19 Co-adsorption of CO and O_2 on a free Au atom (A_1, A_2); a Au atom supported on the defect-free h-BN surface (B_1, B_2) and Au trapped by boron (C_1) and nitrogen (D_1) vacancy defects on a h-BN surface. Only part of the slab is shown. The interatomic distances are given in Å [218] (the symbol @ denotes at). Reproduced from *J. Chem. Phys.,* 138 **(2013)**, 034701.

1.5.3 Possibility of CO_2 capture

Sun et al. theoretically investigated that the adsorption/desorption of CO_2 on boron nitride (BN) nanosheets and nanotubes (NTs) with different charge states [220]. The results show that the process of CO_2 capture/release can be simply controlled by switching on/off the charges carried by BN nanomaterials. CO_2 molecules form weak interactions with uncharged

BN nanomaterials and are weakly adsorbed. When extra electrons are introduced to these nanomaterials (i.e., when they are negatively charged), CO_2 molecules become tightly bound and strongly adsorbed as shown in Figure 1.20. Once the electrons are removed, CO_2 molecules spontaneously desorb from BN absorbents. This study demonstrates that BN nanomaterials are excellent absorbents for controllable, highly selective, and reversible capture and release of CO_2.

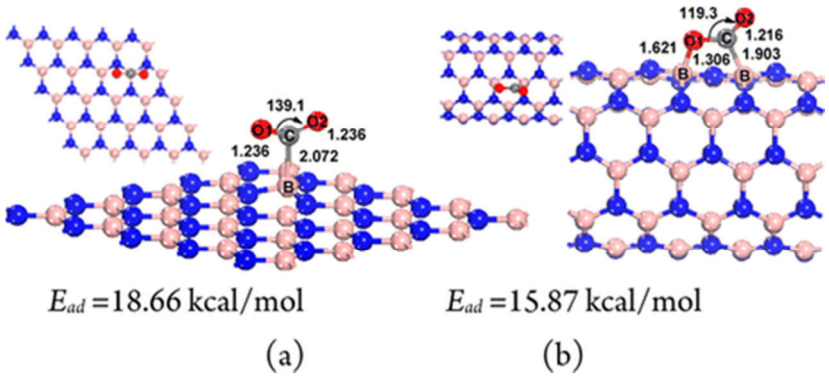

Figure: 1.20 Top and side views of chemisorbed CO_2 on $1e^-$ charge carrying state of a (a) 5×5 BN sheet and (b) BNNT (5,5). Atom color code: blue, nitrogen; pink, boron; gray, carbon; red O_2 [220]. Reproduced from *J. Am. Chem. Soc.,* 135, **(2013)**, 8246.

1.5.4 Possibility of adsorption and desorption of Oxygen

Theoretical calculations confirm that the electronic properties of an h-BN monolayer supported on 3d, 4d and 5d transition metal surfaces can be strongly modified as a result of mixing of the dz^2 metal orbitals with N-p_z and B-p_z orbitals of the h-BN monolayer [221]. Such mixing is responsible for a substantial modification of the electronic properties of h-BN monolayer supported on 3d, 4d, and 5d transition metal surfaces [221, 222] and also affects the catalytic activity of small metal particles supported on h-BN [145, 222-224]. Recently, it has been presented theoretically based on density functional theory that the possibility of ORR activity of monolayer h-BN functionalized Ni(111) support [222]. It has shown that Ni(111) substrate (Fig. 1.21 & 1.22) can apparently change capability of h-BN to adsorb simple molecules and activate O-O bond in O_2 and OOH species [222], showing h-BN/Ni(111) is a good candidate for ORR catalyst. However, Nickel is not stable in the potential region close to the onset of ORR and, therefore, not a good substrate to prove the theoretical prediction of possible electrocatalytic activity of BN for ORR.

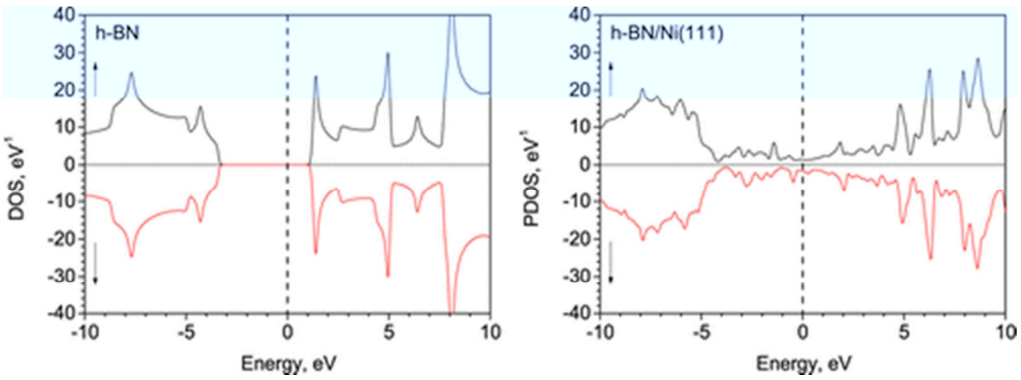

Figure: 1.21 (Left) Spin-polarized DOS calculated for free monolayer h-BN and (right) partial DOS (PDOS) projected on the B and N atoms for the h-BN/Ni(111) system. The position of the Fermi level is indicated by a dashed vertical line at 0 eV. Arrows directed upward and downward indicate the spin-up and spin-down DOS, respectively [222]. Reproduced from *J. Phys. Chem. C* 117 (**2013**), 21359.

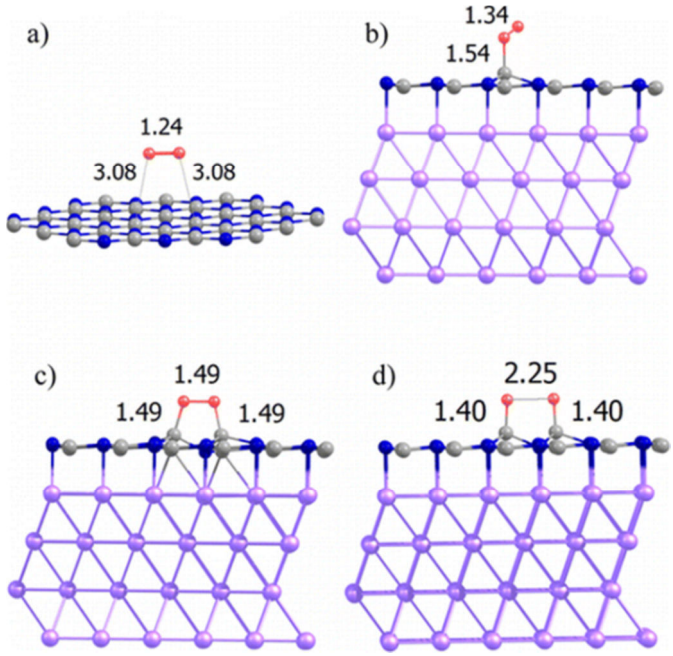

Figure: 1.22 Optimized structures of molecular O_2 (a) physisorb on free monolayer h-BN and ((b), (c)) chemisorbed on the h-BN/Ni(111) surface in the (b) on-top (doublet spin state) and (c) bridge (singlet spin state) configurations. (d) Dissociative adsorption of O_2 on h-BN/Ni(111). Distances are given in angstroms [222]. Reproduced from *J. Phys. Chem. C* 117 (**2013**), 21359.

1.5.5 Adsorption of Hydrogen

There are wide ranges of theoretical and experimental studies have been reported in elsewhere claiming that the BN can adsorb H_2 comparatively better than carbon nanotubes (CNTs) [225-229]. Because, it has the ionic character of B-N bond, which may induce an extra dipole moment and hence H_2 strongly adsorbs on BN. In fact, this feature may applicable for all ionic materials because the induced dipole moment of H_2 is sensitive to local electric field [228-230]. The adsorption of H_2 on BN is a chemisorption process [229]. Also, it have been reported that the doping of transition metals with BN can enhance the H_2 uptake capacity [231, 232] up to 8%. Durgun et al. theoretically investigated the H_2 absorption capacity of Ti-covered single walled boron nitride nanotube (SWBNT) [232] as shown in Figure 1.23. A single Ti atom functionalized SWBNT can bind up to four H_2 molecules, one is dissociated and the remaining three are molecularly absorbed. Accordingly, the H_2 storage capacity of the system ranges between 3.9 and 5.7 wt % [232].

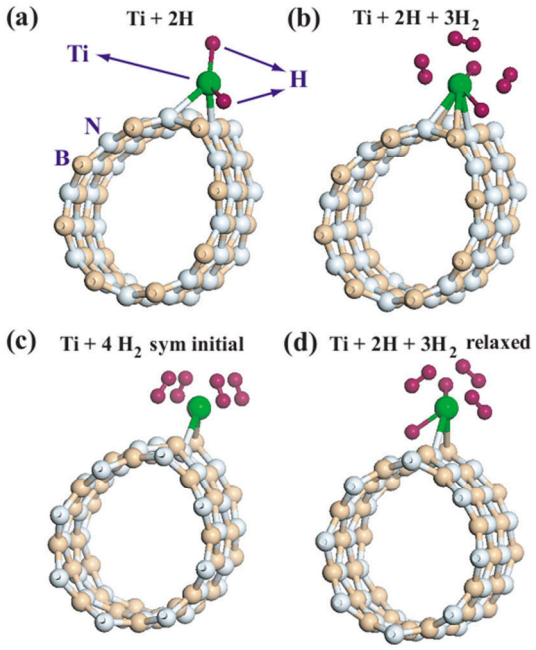

Figure: 1. 23 (Color online) The configuration of H_2 molecules absorbing to (8,0) SWBNT + Ti system. (a) First H_2 molecule dissociates into two H atom.(b) Subsequent three H_2 are molecularly absorbed around Ti. (c) Possible (unrelaxed) symmetric configuration similar to that of SWNT + Ti with four H_2 molecularly absorbed around Ti [232]. (d) The resulting configuration occurring upon the relaxation of (c). Reproduced from *Phys. Rev. B* 76 **(2007)**, 073413.

1.6 Objectives and outline of the present thesis

Fuel cells (FCs) are anticipated as one of the best possible energy conversion devices in future society due to their high energy density, high efficiency, and negligible emission of exhaust gases. The cathodic oxygen reduction reaction (ORR) has been extensively studied because it is the most crucial process in FCs. Although the thermodynamic potential of ORR is 1.23 V vs. SHE, currently there exists a large overpotential even when Pt, which is the best electrocatalyst, is used.

Hydrogen is the cleanest fuel and is considered to be one of the most promising energy carriers. It is currently produced from fossil fuels but must be produced from water for hydrogen to be considered as a really clean fuel. Electrocatalysis of water is the most promising method to produce large amounts of hydrogen from water.

Although Pt has high electrocatalytic activity for ORR and hydrogen evolution reaction (HER), its scarcity and high cost inhibit large-scale applications. Hence, it is important to develop non-precious metal catalysts as efficient electrocatalysts for practical applications and many electrocatalysts have been developed to reduce the overpotential of ORR and the HER. One of the most interesting electrocatalysts is nitrogen- and/or boron-doped carbon. Boron nitride (BN) has a similar structure to graphite but is an insulator and, therefore, has not been considered as an electrocatalysts. Recent theoretical works suggests that BN can be a good ORR electrocatalyst if defects are introduced and/or it is placed on a suitable substrate.

In the present thesis, I have proved that BN acts as good electrocatalysts for ORR and HER, opening a new possibility to design efficient Pt free catalysts for fuel cell technology and hydrogen production based on materials, which have never been considered as catalysts in the past.

The structure of present thesis is as follows:

In Chapter 1, the introduction of FCs, ORR and HER are given. The electrocatalytic activity of various catalysts such as precious metals, non-precious metals, and metal free catalyst for ORR and HER are briefly reviewed. The electron tunnelling properties and possible catalytic activities of traditionally inert materials are also reviewed.

In Chapter 2, the description of the experimental details such as materials, catalyst preparation methods, electrochemical measurements, and characterization techniques are given.

In Chapter 3, the electrocatalytic activities of various types of h-BN such as BN nanotube (BNNT), BN nanosheets (BNNS), and sputter deposited BN, coated on Au, glassy carbon (GC) and Pt electrodes, for ORR are examined. The overpotential for ORR at Au electrode is reduced by ca. 100, ca. 270, and ca.150 mV by coating with BNNT, BNNS, and sputter deposited BN, respectively, showing the enhancement of electrocatalytic activity. Rotating disk electrode (RDE) and rotating ring disk electrode (RRDE) studies shows that O_2 is reduced to H_2O_2 by 2-electron reduction. On the other hand, ORR activity of GC electrode is not enhanced and that of Pt is reduced by the BNNS modification, suggesting that the BN-Au substrate interaction plays an important role for BN to become ORR active.

In Chapter 4, the electrocatalytic reactivity of BNNS decorated with Au nanoclusters (Au-NCs) on Au for ORR is examined. The overpotential of ORR at Au electrode is significantly reduced by 300 mV by the modification of BNNS decorated with Au-NCs. The enhanced catalytic activity of BNNS decorated with Au-NCs is attributed to the electron transfer at the interface between Au and neighbouring B- and/or N- atoms. The number of electrons involved in ORR determined from the slope of Koutecky-Levich plot is about 3 and RRDE measurements suggest the partial production of H_2O_2 by 2-electron reduction and H_2O by 4-electron reduction. This is in contrast to the results at the bare and BNNS modified Au electrodes, where only H_2O_2 is formed by 2-electron reduction. Electrocatalytic activity for ORR is enhanced even at the GC electrode when it is modified by BNNS decorated with Au-NCs, confirming the importance of Au-BN interaction for the enhancement of electrocatalytic activity.

In Chapter 5, the electrocatalytic evolution of hydrogen at Au, GC and Pt modified by BNNS and BNNS decorated with Au- and Ni-NCs are investigated. HER at Au, GC and Pt electrodes are enhanced, not much changed, and reduced, respectively, by BNNS modification as for ORR. HER at Au, GC and Pt electrodes are all enhanced by the modification of BNNS decorated with Au-NCs (Au/BNNS). HER activity of Au electrode modified by Au/BNNS is very high with only ca. 50 mV more overpotential than Pt. Modification by BNNS decorated with Ni-NCs (Ni/BNNS) also showed enhanced HER

activity but much less than by the Au/BNNS modification, showing the important role of Au-BN interaction for the enhancement of HER as well. Interestingly, hydrogen oxidation reaction (HOR), i.e., reverse reaction of HER, at Au electrode is not enhanced by BNNS and Au- or Ni/BNNS modification, showing the unique feature of this catalyst.

In Chapter 6, the general conclusion of the present thesis and future prospects are given.

1.7 References

(1) W. Vielstich, A. Lamm, and H. A. Gasteiger, eds., *Handbook of FCs: Fundamentals, Technology, Applications*, Wiley, **(2003)**.

(2) J. W. Gosselink, *Int. J. H_2 Energy,* 27 **(2002),** 1125.

(3) S. Srinivasan, *FCs: from fundamentals to applications*; Springer, **(2006)**.

(4) J. M. Andujar, and F. Segura, *Renewable & Sustainable Energy Rev.,* 13 **(2009),** 2309.

(5) H. J. Neef, *Energy,* 34 **(2009),** 327.

(6) A. Kirubakaran, S. Jain, and R. K. Nema, *Renewable & Sustainable Energy Rev.,* 13 **(2009),** 2430.

(7) J. Malzbender, R.W. Steinbrech, and L. Singheiser, *Fuell Cells,* 9 **(2009)** 785.

(8) M. Winter, and R. J. Brodd, *Chem. Rev*., 104 **(2004)**, 4245.

(9) B. C. H. Steele, and A. Heinzel, *Nature*, 414 **(2001)**, 345.

(10) H. A. Gastieger, and N. M. Morkovic, *Science*, 324 **(2009)**, 48.

(11) M. K. Debe, *Nature,* 486 **(2012),** 43.

(12) J. Greeley, and N. M. Morkovic, *Energy Environ. Sci.,* 5 **(2012),** 9246.

(13) N. M. Morkovic, and P. N. Ross, *Surf. Sci. Rep.*, 45 **(2002),** 117.

(14) W. Sheng, H. A. Gasteiger, and Y. S. Horn, *J. Electrochem., Soc.,* 157 **(2010)** B159.

(15) D. Strmcnik, M. Uchimura, C. Wang, R. Subbaraman, N. Danilovic, D. van der Vlit, A. P. Paulikas, V. R. Stamenkovic, and N. M. Markovic, *Natrure Chem.,* 5 **(2013)**, 300.

(16) V. R. Stamenkovic, N. M. Markovic, and P.N. Ross, *J. Electroanal. Chem.,* 500 **(2001)**, 44.

(17) H. Uchida, K. Izumi, and M. Watanabe, *J. Phys. Chem. B,* 110 **(2006)**, 21924.

(18) R. M. Q. Mello, and E. A. Ticianelli, *Electrochim. Acta*, 42 **(1997)**, 103.

(19) N. M. Markovic, S. T. Sarraf, H. A. Gasteiger, and P. N. Ross, *J. Chem. Soc., Faraday Trans.*, 92 (**1996),** 3719.

(20) T. J. Schmidt, P. N. Ross, and N. M. Markovic, *J. Electroanal. Chem.,* 524 **(2002)**,

252.

(21) B. E. Conway, and B. V. Tilak, *Electrochim. Acta,* 47 **(2002),** 3571.

(22) T. R. Rolf, *Pt Metals Rev.,* 41 **(1997),** 102.

(23) N. M. Markovic, T. J. Schmidt, V. R. Stamenkovic, and P. N. Ross, *Fuel Cells* 1 **(2001)**, 105.

(24) D. Wang, H. L. Xin, R. Hovden, H. Wang, Y. Yu, D. A. Muller, F. J. Disalvo, and H. D. Abruna, *Nature Mater.*, 12 **(2012),** 81.

(25) J. Greeley, et al. *Nature Chem.* 1**(2009),** 552.

(26) M. H. Shao, K. Shoemaker, A. Peles, K. Kaneko, and L. Protsailo, *J. Am. Chem. Soc*. 132 **(2010)**, 9253.

(27) V. R. Stamenkovic, B. S. Mun, M. Arenz, K. J. J. Mayrhofer, C. A. Lucas, G. Wang, P. N. Ross, and N. M. Markovic, *Nature Mater.,* 6 **(2007)**, 241.

(28) H. Yano, M. Kataoka, H. Yamashita, H. Uchida, and M. Watanabe, *Langmuir,* 23 **(2007)**, 6438.

(29) E. Antolini, J. R. C. Salgado, and E. R. Gonzalez, *J. Power Sources*, 160 **(2006)**, 957.

(30) J. Kim, Y. Lee, and S. H. Sun, *J. Am. Chem. Soc.,* 132 **(2010),** 4996.

(31) A. R. Malheiro , J. Perez, and H. M. Villullas, *J. Electrochem. Soc.*, 156 **(2009),** B51.

(32) V. R. Stamenkovic, B. S. Mun, K. J. J. Mayrhofer, P. N. Ross, and N. M. Markovic, *J. Am. Chem. Soc.,* 128 **(2006)**, 8813.

(33) S. J. Hwang, S. J. Yoo, S. Jang, T. H. Lim, S. A. Hong, and S. K. Kim, *J. Phys. Chem. C,* 115 **(2011),** 2483.

(34) M. K. Min, J. H. Cho, K. W. Cho, and H. Kim, *Electrochim. Acta*, 45 **(2000)**, 4211.

(35) V. R. Stamenkovic, T. J. Schmidt, P. N. Ross, and N. M. Markovic, *J. Phys. Chem. B,* 106 **(2002),** 11970.

(36) H. L. Xin, et al. *Nano Lett.,*12 **(2012)**, 490.

(37) J. B. Wu, et al. *J. Am. Chem. Soc.,* 132 **(2010),** 4984.

(38) J. Zhang, H. Z. Yang, J. Y. Fang, and S. Z. Zou, *Nano Lett.,*10 **(2010),** 638.

(39) P. Strasser et al., *Nature Chem.,* 2 **(2010)**, 454.

(40) P. Mani, R. Srivastava, and P. Strasser, *J. Phys. Chem. C,* 112 **(2008)**, 2770.

(41) R. Srivastava, P. Mani, N. Hahn, and P. Strasser, *Angew. Chem. Int. Ed.,* 46 **(2007)**, 8988.

(42) M. K. Jeon, Y. A. Zhang, and P. J. McGinn, *Electrochim. Acta,* 55 **(2010)**, 5318.

(43) Y. Kang, and C. B. Murray, *J. Am. Chem. Soc.,* 132 **(2010)**, 7568.

(44) J. M. Kim and A. A. Gewrich, *J. Phys. Chem. B,* 110 **(2006)**, 2565.

(45) N. Ohta, K. Nomura and I. Yagi, *J. Phys. Chem. C,* 116 **(2012)**, 14390.

(46) R. R. Adzic and J. X. Wang, *J. Phys. Chem. B,* 102 **(1998)**, 8988.

(47) F. Y. Cheng and J. Chen, *Chem. Soc. Rev.,* 41 **(2012)**, 2172.

(48) Z. Shi, J. J. Zhang, Z. S. Liu, H. J. Wang and D. P. Wilkinson, *Eloctrochim. Acta,* 51 **(2006)**, 1905.

(49) Y. Suzuku and K. Yamshida, *Chem. Phys. Lett.,* 486 **(2010)**, 48.

(50) E. Yeager, *Electrochem., Acta* 29 **(1984)**, 1527.

(51) A. Eichler and J. Hafner, *Phys. Rev. Lett.,* 79 **(1997)**, 4481.

(52) R. R. Adzic and J. X. Wang, *Solid State Ionics,* 150 **(2002)**, 105.

(53) J. H. Shao, P. Liu and R. R. Adzic, *J. Am. Chem. Soc.,* 128 **(2006)**, 7408.

(54) J. Omura, H. Yano, M. Watanabe and H. Uchida, *Langmuir,* 27 **(2011)**, 6464.

(55) S. Tong, H. Noguchi,T. Masuda and K. Uosaki, *Electrochem. Commun*., 34 **(2013)**, 33.

(56) A. Damjanovic, *Modern aspects of Electrochemistry*, 5 **(1969)**, 369.

(57) Y. J. Wang, D. P. Wilkinson, and J. Zhang, *Chem. Rev*., 111 (**2011**), 7625.

(58) D.-H. Lim, W.-J. Lee, J. Wheldon, N. L. Macy, and W. H. Smyrl, *J. Electrochem. Soc.,* 157 **(2010)**, B862.

(59) R. R. Adzic, J. Zhang, K. Sasaki, M. B. Vukmirovic, M. Shao, J. X. Wang, A. U. Nilekar, M. Mavrikakis, J. A.Valerio, and F. Uribe, *Top. Catal.,* 46 **(2007)**, 249.

(60) K. Lee, J. Zhang, H. Wang, and D. P. Wilkinson, *J. Appl. Electrochem*., 36 **(2006),** 507.

(61) P. Serp, M. Corrias, and P. Kalck, *Appl. Catal. A,* 253 **(2003)**, 337.

(62) I. E. L. Stephens, A. S. Bondarenko, U. Grønbjerg, J. Rossmeisl and Ib. Chorkendorff. *Energy Environ. Sci.,* 5 **(2012)**, 6744.

(63) E. Antolini, *Appl. Catal., B* 88 **(2009),** 1.

(64) T. J. Schmidt, H. A. Gasteiger, G. D. Stab, P. M. Urban, D. M. Kolb, and R. J. Behm, *J. Electrochem. Soc.,* 145 **(1998)**, 2354.

(65) E. Passalacqua, F. Lufrano, G. Squadrito, A. Patti, and L. Giorgi, *Electrochim. Acta,* 46 **(2001),** 799.

(66) S. D. Knights, K. M. Colbow, J. St-Pierre, and D. P. Wilkinson, *J. Power Sources,* 127 **(2004),** 127.

(67) S. Zhang, X. Yuan, H. Wnag, W. Merida, H. Zhu, J. Shen, S. Wu, and J. Zhang, *Int. J. Hydrogen Energy*, 34 **(2009),** 388.

(68) E. Yeager *J. Mol. Catal.,* 38 **(1986)**, 5.

(69) A. J. Bard, L. R. Faulkner, *Electrochemical methods: fundamentals and applications*, New York: Wiley, **(1980)**.

(70) H. S. Wroblowa, Y. C. Pan, and G. Razumney, *J. Electroanal. Chem.,* 69 **(1976),** 195.

(71) A. Stassi, C. D'Urso, V. Baglio, A. Diblasi, V. Antonucci, A.S.Arico, A.M. Castroluna, A. Bonesi, and W. E. Triaca, *J. Appl. Electro. Chem.,* 36 **(2006)**, 1143.

(72) N. M. Markovic, H. A. Gasteiger, and P. N. Ross, *J. Phy. Chem.,* 99 **(1995),** 3411.

(73) N. M. Markovic, H. A. Gasteiger, and P. N. Ross, *J. Phy. Chem.,* 100 **(1996),** 6715.

(74) R. R. Adzic, S. Strbac and N. Anastasijevic, *Materials Chemistry and Physics,* 22 **(1989)**, 349.

(75) D. V. Tripkovic, D. Strmcnik, D. V. D. Vliet, V. Stamenkovic, and N. M. Markovic, *Faraday Discuss.,* 140 **(2009)**, 25.

(76) A. Prieto, J. Hernandez, E. Herrero, and J. M. Feliu, *J. Solid state Electrochem.,* 7 **(2003)**, 599.

(77) J. K. Nørskov, J. Rossmeisl, A. Logadottir, L. Lindqvist, J. R. Kitchin, T. Bligaard, and H. Jonsson, *J. Phys. Chem. B,* 108 **(2004),**17886.

(78) H. A. Hansen, V. Viswanathan, and J. K. Nørskov, *J. Phys. Chem. C,* 118 **(2014)**, 6706.

(79) Y. Xu, A. V. Ruban, and M. Mavrikakis, *J. Am. Chem. Soc.,* 126 **(2004)**, 4717.

(80) Y. Shao-Horn, W. C. Sheng, S. Chen, P. J. Ferreira, E. F. Holby and D. Morgan, *Top. Catal*., 46 **(2007)**, 285.

(81) V. R. Stamenkovic, B. Fowler, B. S. Mun, G. Wang, P. N. Ross, C. A. Lucas, and N. M. Markovic, *Science,* 315 **(2007)**, 493.

(82) A. Kongkanand, S.Kuwabata, G. Girishkumar, and P. Kamat, *Langmuir,* 22 (**2006)**, 2392.

(83) J. Zhang, K. Sasaki, E. Sutter, and R. R. Adzic, *Science,* 315 (**2007**), 220.

(84) B. Lim, M. J. Jiang, P. H. C. Camargo, E. C. Cho, J. Tao, X. M. Lu, Y. M. Zhu, and Y. N. Xia, *Science,* 324 (**2009**), 1302.

(85) F. Colmati, E. Antolini, E. and R. Gonzalez, *J. Power Sources,* 157 (**2006**), 98.

(86) W. Chen, J. M. Kim, S. H. Sun, and S. W. Chen, *J. Phys. Chem. C,* 112 (**2008**), 3891.

(87) Y. Xu, H. Wang, R. Zhu, C. Liu, X. Wu, and B. Zhang, *Chem. Asian J.,* 8 (**2013**), 1120.

(88) G. Wu, and P. Zeleny, *Acc. Chem. Res.,* 46 (**2013**), 1878.

(89) C. Yuan, H. B. Wu, Y. Xie, and X. W. Lou, *Angew. Chem. Int. Ed.* 53 **(2014),** 1488.

(90) X. Yu, and S. Ye, *J. Power Sources,* 172 (**2007**), 145.

(91) Y. Y. Shao, J. Liu, Y. Wang, and Y. H. Lin, *J. Mater. Chem.,* 19 (**2009**), 46.

(92) B. Cao, G. M. Veith, R. E. Diaz, J. Liu, E. A. Stach, R. R. Adzic, and P. G. Khalifah, *Angew. Chem. Int. Ed.,* 52 (**2013**), 10753.

(93) Y. Maekawa, A. Ishihara, J. H. Kim, S. Mitsushima, and K.-i. Ota, *Electrochem. Solid-*

State Lett., 11 (**2008**), B109-B112.

(94) G. Zhong, H. Wang, H. Yu, and F. Peng, *Fuel Cells*, 13 (**2013**), 387.

(95) Y. Liu, T. G. Kelly, J. G. Chen, and W. E. Mustain, *ACS Catal.,* 3 **(2013),** 1184.

(96) H. Chhina, S. Campbell and O. Kesler, *J. Power Sources*, 161 **(2006),** 893.

(97) T. Ioroi, Z. Siroma, N. Fujiwara, S. Yamazaki and K. Yasuda, *Electrochem. Commun.,* 7 **(2005),** 183.

(98) K. W. Park, K. S. Ahn, Y. C. Nah, J. H. Choi and Y. E. Sung, *J. Phys. Chem. B*, 107 **(2003),** 4352.

(99) A. C. Chen, D. J. La Russa and B. Miller, *Langmuir,* 20 **(2004),** 9695.

(100) M. S. Saha, R. Y. Li and X. L. Sun, *Electrochem. Commun.,* 9 **(2007),** 2229.

(101) Z. S. Wu, S. Yang, Y. Sun, K. Parvez, X. Feng, and K. Müllen, *J. Am. Chem. Soc*., 134 **(2012),** 9082 and references therein.

(102) X. Y. Yan, X. L. Tong, Y. F. Zhang, X. D. Han, Y. Y. Wang, G. Q. Jin, Y. Qina, and X. Y. Guo, *Chem. Commun.*, 48 **(2012)**, 1892.

(103) W. Xiao, D. Wang, and X. W. Lou, *J. Phys. Chem. C,* 114 **(2010),** 1694.

(104) Y. Liang, Y. Li, H. Wang, J. Zhou, J. Wang, T. Regier, and H. Dai, *Nature Mater*., 10 **(2011)**, 780.

(105) Y. Liang, Y. Li, H. Wang, J. Zhou, Y. Li, J. Wang, T. Regier, and H. Dai, *J. Am. Chem. Soc.,* 134 **(2012),** 3517.

(106) Z. G. Chen, X. P. Qiu, B. Lu, S. C. Zhang, W. T. Zhu, and L. Q. Chen, *Electrochem. Commun.,* 7 **(2005),** 593.

(107) H. M. Villullas, F. I. Mattos-Costa, and L. O. S. Bulhoes, *J. Phys. Chem. B*, 108 **(2004),** 12898.

(108) Z. Jusys, T. J. Schmidt, L. Dubau, K. Lasch, L. Jorissen, J. Garche, and R. J. Behm, *J. Power Sources,* 105 **(2002)**, 297.

(109) S. Shanmugam, and A. Gedanken, *Small*, 3 **(2007)**, 1189.

(110) J. A. Tian, G. Q. Sun, L. H. Jiang, S. Y. Yan, Q. Mao and Q. Xin, *Electrochem. Commun*., 9 **(2007),** 563.

(111) T. Masuda, H. Fukumitsu, K. Fugane, H. Togasaki, D. Matsumura, K. Tamura, Y. Nishihata, H. Yoshikawa,K. Kobayashi,T. Mori, and K. Uosaki. *J. Phys. Chem. C,* 116 **(2012)**, 10098.

(112) R. B. Levy, and M. Boudart, *Science,* 181 **(1973),** 547.

(113) B. Dhandapani, T. S. Clair, and S. T. Oyama, *Appl. Catal. A,* 168 **(1998**), 219.

(114) E. Furimsky, *Appl. Catal. A,* 240 **(2003),** 1.

(115) S. T. Oyama, *The Chemistry of Transition Metal Carbides and Nitrides*; Springer: London, **(1996)**.

(116) B. Avasarala, T. Murray, W. Li, and P. Haldar, *J. Mater. Chem.,* 19 **(2009)**, 1803.

(117) D. J. Ham, and J. S. Lee, *Energies,* 2 **(2009)**, 873.

(118) R. B. Levy, and M. Boudart, *Science,* 181 **(1973),** 547.

(119) H. H. Hwu and J. G. G. Chen, *J. Vac. Sci. Technol. A*, 21 **(2003)**, 1488.

(120) N. Keller, B. Pietruszka and V. Keller, *Mater. Lett.,* 60 **(2006),** 1774.

(121) H. H. Hwu, and J. G. Chen, *J. Phys. Chem. B,* 107 **(2003),** 2029.

(122) H. Meng, and P. K. Shen, *J. Phys. Chem. B,* 109 **(2005),** 22705.

(123) S. Shanmugam, D. S. Jacob, and A. Gedanken, *J. Phys. Chem. B*, 109 **(2005),** 19056.

(124) T. C. Xiao, A. Hanif, A. P. E. York, J. Sloan, and M. L. H. Green, *Phys. Chem. Chem. Phys*., 4 **(2002),** 3522.

(125) S. Maldonado, and K. J. Stevenson, *J. Phys. Chem. B,* 109 **(2005)**, 4707.

(126) R. A. Sidik, A. B. Anderson, N. P. Subramanian, S. P. Kumaraguru, and B. N. Popov, *J. Phys. Chem. B,* 110 **(2006)**, 1787.

(127) K. Gong, F. Du, Z. Xia, M. Durstock, and L. Dai, *Science*, 323 **(2009)**, 760.

(128) L. Zhang, and Z. Xia, *J. Phys. Chem.C,* 115 **(2011)**, 11170.

(129) D. S. Yang, Bhattacharjya, S. Inamdar, J. Park, and J. S. Yu, *J. Am. Chem. Soc.,* 134 (**2012**), 16127.

(130) T. Ikeda, M. Boero, S.-F. Huang, K. Terakura, M. Oshima, J.-i. Ozaki and S. Miyata, *J. Phys. Chem. C,* 114 **(2010),** 8933.

(131) Z. Yao, H. G. Nie, Z. Yang, X. M. Zhou, Z. Liu, S. M. Huang, *Chem. Commun.,* 48 (**2012**), 1027.

(132) Y. Jiao, Y. Zheng, M. Jaroniec, S. Z. Qiao, *J. Am. Chem. Soc.,* 136 **(2014),** 4394.

(133) J.-i. Ozaki, T. Anahara, N. Kimura and A. Oya, *Carbon*, 44 **(2006),** 3358.

(134) J.-i. Ozaki, N. Kimura, T. Anahara and A. Oya, *Carbon*, 45 **(2007)**, 1847.

(135) T. Ikeda, M. Boero, S.-F. Huang, K. Terakura, M. Oshima and J.-i. Ozaki, *J. Phys. Chem. C,* 112 **(2008),** 14706.

(136) L. Yu, X. Pan, X. Cao, P. Hu and X. Bao, *J. Catal.,* 282 **(2011),**183.

(137) L. Zhang and Z. Xia, *J. Phys. Chem. C*, 115 **(2011)**, 11170.

(138) L. Qu, Y. Liu, J.-B. Baek and L. Dai, *ACS Nano*, 4 **(2010),** 1321.

(139) X. Wang, Z. Hou, T. Ikeda, S.-F. Huang, K. Terakura, M. Boero, M. Oshima, M.-A. Kakimoto, S. Miyata, *Phys. Rev. B: Condens. Matter Mater. Phys.,* 84 **(2011),** 245434.

(140) S. Wang, E. Iyyamperumal, A. Roy, Y. Xue, D, Yu, and L. Dai, *Angew. Chem*., 123

(**2011**), 11960; *Angew. Int. Ed*., 50 **(2011),** 11756.

(141) J. B. Xu and T. S. Zhao, *RSC Adv.,* 3 **(2013)**, 16.

(142) X. Wang, C. Zhi, L. Li, H. Zeng, C. Li, M. Mitome, D. Golberg, and Y. Bando, *Adv. Mater.,* 23 **(2011),** 4072.

(143) X. Wang, A. Pakdel, C. Zhi, K. Watanabe, T. Sekiguchi, D. Golberg, and Y. Bando, *J. Phys.: Condens. Matter*, 24 **(2012),** 314205.

(144) J. Furthmuller, J. Hafner and G. Kresse, *Phys. Rev. B: Con-dens. Matter Mater. Phys.,* 50 **(1994),** 15606.

(145) A. Lyalin, A. Nakayama, K. Uosaki, and T. Taketsugu, *Phys. Chem. Chem. Phys*., 15 (**2013**), 2809.

(146) M. H. Miles, *J. Electroanaly. Chem*., 60 **(1975),** 89.

(147) N. M. Markovic, B. N. Grgur, and P. N. Ross, *J. Phys. Chem. B* 101 **(1997)**, 5405.

(148) A. Anani, A. Visitin, K. Petrov, S. Srinivasan, J. J. Reilly, J. R. Johnson, R. B. Schwarz and P. B. Desch, *J. Power Sources*, 47 **(1994)**, 261.

(149) K. Watanabe and T. Kikuoka, *J. Appl. Electrochem.*, 25 **(1995),** 219.

(150) J. Greeley, and N. M. Markovic, *Energy Environ. Sci.,* 5, **(2012)**, 9246.

(151) J. B. Goodenough, *J. Solid State Electrochem.,* 16 **(2012)**, 2019.

(152) J. O. M. Bockris and E. C. Potter, *J. Electrochem. Soc.*, 99 **(1952)**, 169.

(153) V. S. Bagotsky, *Fundamentals of electrochemistry*, John Wiley & Sons, Inc., Hoboken, New Jersey, 2nd edn, **(2006)**.

(154) M. H. Miles and M. A. Thomason, *J. Electrochem. Soc.,* 123 **(1976),** 1459.

(155) S. Trasatti, *J. Electroanal. Chem.*, 39 **(1972),** 163.

(156) B. Conway and G. Jerkiewicz, *Electrochim. Acta*, 45 **(2000)**, 4075.

(157) J. K. Norskov, T. Bligaard, A. Logadottir, J. R. Kitchin, J. G. Chen, S. Pandelov and J. K. Norskov, *J. Electrochem. Soc.,* 152 **(2005),** J23.

(158) Y.-H. Fang, G.-F. Wei and Z.-P. Liu, *J. Phys. Chem. C*, 117 **(2013),** 7669.

(159) W.-F. Chen, J. T. Muckerman, and E. Fujita, *Chem. Commun.*, 49 **(2013)**, 8896.

(160) D. M. Soares, O. Teschke, and I. Torriani, *J. Electrochem. Soc.,* 139 **(1992),** 98.

(161) J. Tamm, L. Tamm, and J. Arol'd, *Russ. J. Electrochem.,* 40 **(2004),** 1343.

(162) W.-F. Chen, K. Sasaki, C. Ma, A. I. Frenkel, N. Marinkovic, J. T. Muckerman, Y. Zhu, and R. R. Adzic, *Angew. Chem. Int. Ed.,* 51 **(2012),** 6131.

(163) E. J. Popczun, J. R. McKone, C. G. Read, A. J. Biacchi, A. M. Wiltrout, N. S. Lewis, and R. E. Schaak, *J. Am. Chem. Soc*., 135 **(2013),** 9267.

(164) A. B. Laursen, S. Kegnaes, S. Dahl and I. Chorkendorff, *Energy Environ. Sci.*, 5 **(2012),**

5577.

(165) D. Merki and X. L. Hu, *Energy Environ. Sci.,* 4 **(2011),** 3878.

(166) S. S. Chou, M. De, J. Kim, S. Byun, C. Dykstra, J. Yu, J. Huang and V. P. Dravid, *J. Am. Chem. Soc.,* 135 **(2013)**, 4584.

(167) D. Merki, S. Fierro, H. Vrubel and X. L. Hu, *Chem. Sci.,* 2 **(2011),** 1262.

(168) H. Vrubel, D. Merki and X. Hu, *Energy Environ. Sci.*, 5 **(2012),** 6136.

(169) D. J. Ham and J. S. Lee, *Energies*, 2 **(2009),** 873.

(170) T. G. Kelly and J. G. Chen, *Chem. Soc. Rev.,* 41 **(2012)**, 8021.

(171) Z. Yan, M. Cai and P. K. Shen, *Sci. Rep.,* 3 **(2013),** 1646.

(172) Y. Li, H. Wang, L. Xie, Y. Liang, G. Hong, and H. Dai, *J. Am. Chem. Soc.*, 133 **(2012)**, 7296.

(173) T. F. Jaramillo, K. P. Jorgensen, J. Bonde, J. H. Nielsen, S. Horch, and Ib. Chaokendorff, *Science*, 317 **(2007),** 100.

(174) B. Hinnemann, P. G. Moses, J. Bonde, K. P. Jørgensen, J. H. Nielsen, S. Horch, I. Chorkendorff and J. K. Nørskov, *J. Am. Chem. Soc.,* 127 **(2005),** 5308.

(175) Z. Z. Wu, B. Z. Fang, A. Bonakdarpour, A. K. Sun, D. P. Wilkinson and D. Z. Wang, *Appl. Catal., B*, 125 **(2012),** 59.

(176) D. Voiry, H. Yamaguchi, J. Li, R. Silva, D. C. B. Alves, T. Fujita, M. Chen, T. Asefa, V. B. Shenoy, G. Eda, and M. Chhowalla, *Nat. Mater.,* 12 **(2013)**, 850.

(177) M. V. Bollinger, J. V. Lauritsen, K. W. Jacobsen, J. K. Nørskov, S. Helveg, and F. Besenbacher, *Phy. Rev. Lett.,* 87 **(2001)**, 196803.

(178) L. I. Johansson, *Suf. Sci. Rep.,* 21 **(1995)**, 179.

(179) D. V. Esposito, S. T. Hunt, Y. C. Kimmel and J. G. Chen, *J. Am. Chem. Soc.,* 134 **(2012),** 3025.

(180) R. Memming and G. Schwandt, *Surface Science,* 4 **(1966)**, 109.

(181) Y. Nakato, S.Tonomura, and H. Tsubomura, *Ber. Bunsen. Phys.Chem.,* 80 **(1976)**, 1289.

(182) R. N. Dominey, N. S. Lewis, J. A. Bruce, D. C. Bookbinder, and M. S. Wrighton, *J. Am. Chem. Soc.,* 104 **(1982)**, 467.

(183) Y. Nakato, H. Yano, S. Nishiura, T. Ueda, and H. Tsubomura, *J. Electroanal. Chem. Interfacial Electrochem.,* 228 **(1987)**, 97.

(184) R. N. Dominey, N. S. Lewis, J. A. Bruce, D. C. Bookbinder and M. S. Wrighton, *J. Am. Chem. Soc.,* 104 **(1982)**, 467.

(185) S. Y. Reece, J. A. Hamel, K. Sung, T. D. Jarvi, A. J. Esswein, J. J. H. Pijpers, and D. G. Nocera, *Science*, 334 **(2011)**, 645.

(186) Y. Nakato, and H. Tsubomura, *J. Photochem.,* 29 **(1985)**, 257.

(187) J. D. Porter, A. Heller, and D. E. Aspnes, *Nature,* 313**(1985)**, 664.

(188) A. Meier, I. Uhlendorf, and D. Meissner, *Electrochim. Acta,* 40 **(1995),** 1523.

(189) Y. Nakato, H. Yano, S. Nishiura, T. Ueda, and H. Tsubomura, *J. Electroanal. Chem.,* 228 **(1987),** 97.

(190) Y. Nakato, and H. Tsubomura, *Electrochim. Acta,* 37 **(1992)**, 897.

(191) Y. Nakato, K. Ueda, H. Yano, and H. Tsubomura, *J. Phys. Chem.,* 92 **(1988),** 2316.

(192) Y. Nakato, K. Ueda, and H. Tsubomura, *J. Phys. Chem.,* 90 **(1986),** 5495.

(193) S. Kaneko, K. Uosaki, and H. Kita, *J. Phys. Chem.,* 90 **(1986)**, 6654.

(194) I. Lombardi, S. Marchionna, G. Zangari, and S. Pizzini, *Langmuir,* 23 **(2007)**, 12413.

(195) J. Kye, M. Shin, B. Lim, J.-W. Jang, I. Oh, and S. Hwang, *ACS Nano,* 7 **(2013),** 6017.

(196) T. Masuda, K. Shimazu, and K. Uosaki, *J. Phys. Chem. C,* 112 **(2008)**, 10923.

(197) A. P. Goodey, S. M. Eichfeld, K. K. Lew, J. M. Redwing, and T. E. Mallouk, *J. Am. Chem. Soc.,* 129 **(2007)**, 12344.

(198) E. C. Garnett, and P. D. Yang, *J. Am. Chem. Soc.,* 130 **(2008)**, 9224.

(199) B. M. Kayes, H. A. Atwater, and N. S. Lewis, *J. Appl. Phys.,* 97 **(2005),**114302.

(200) S. W. Boettcher, J. M. Spurgeon, M. C. Putnam, E. L.Warren, D. B. Turner-Evans, M. D. Kelzenberg, J. R. Maiolo, H. A. Atwater, and N. S. Lewis, *Science,* 327 **(2010),** 185.

(201) B. Tian, T. J. Kempa, and C. M. Lieber, *Chem. Soc. Rev.,* 38 **(2009),** 16.

(202) H. P. Yoon, Y. A. Yuwen, C. E. Kendrick, G. D. Barber, N. J. Podraza, J. M. Redwing, T. E. Mallouk, C. R. Wronski, and T. S. Mayer, *Appl. Phys. Lett.,* 96 (2010), 213503.

(203) S. W. Boettcher, E. L. Warren, M. C. Putnam, E. A. Santori, D. Turner-Evans, M. D. Kelzenberg, M. G. Walter, J. R. McKone, B. S. Brunschwig, H. A. Atwater, and N. S. Lewis, *J. Am. Chem. Soc.,* 133 **(2011)**, 1216.

(204) W. Sheng, H. A. Gasteiger, and Y. Shao-Horn, *J. Electrochem. Soc.,* 157 **(2010)**, B1529.

(205) D. Strmcnik, K. Kodama, D. van der Vliet, J. Greeley, V. R. Stamenkovic and N. M. Markovic, *Nat. Chem.,* 1 **(2009)**, 466.

(206) H. B. Gray, *Nat. Chem.*, 1 **(2009)**, 7.

(207) B. E. Conway and B. Timothy, *Electrochim Acta*, 47 **(2002)**, 3571.

(208) D. Stmcnik, D. Tripkovic, D. van der Vliet, V. R. Stamenkovic and N. M. Markovic, *Electrochem. Commun.*, 10 **(2008)**, 1602.

(209) Y. H. Li, J. Xing, Z. J. Chen, Z. Li, F. Tian, L. R. Zheng, H. F. Wang, P. Hu, H. J. Zhao and H. G. Yang, *Nat. Commun.*, 4 **(2013)**, 1.

(210) J. C. Wu, Z. Lin, F. J. W. Pan, and M. Rei, *Appl. Catal., A* 219 **(2001)**, 117.

(211) C. A. Lin, J. C. S. Wu, F. J. W. Pan, and C. T. Yeh, *J. Catal.,* 210 **(2002)**, 39.

(212) H. Sumiya, S. Sato, and S. Yazu, U.S. Patent 5, 332, 629, **(1994)**.

(213) H. Zeng, C. Zhi, Z. Zhang, X. Wei, X. Wang, W. Guo, Y. Bando and D. Golberg, *Nano Lett.,* 10 **(2010)**, 5049.

(214) S. Azevedo, J. R. Kaschny, C. M. de Castilho and F. de Brito Mota, *Eur. Phys. J. B*, 67 **(2009)**, 507.

(215) J. Zhou, Q. Wang, Q. Sun and P. Jena, *Phys. Rev. B: Condens. Matter Mater. Phys.*, 81 **(2010)**, 085442.

(216) L. Britnell, R. V. Gorbachev, R. Jalil, B. D. Belle, F. Schedin, M. I. Katsnelson, L. Eaves, S. V. Morozov, A. S. Mayorov, N. M. R. Peres, A. H. Castro Neto, J. Leist, A. K. Geim, L. A. Ponomarenko and K. S. Novoselov*, Nano Lett.*, 12 **(2012),**1707.

(217) A. B. Preobrajenski, A. S. Vinogradov, N. Møartensson, *Surf. Sci.*, 582 **(2005)**, 21.

(218) M. Gao, A. Lyalin, and T. Taketsugu, *J. Chem. Phys.,* 138 **(2013)**, 034701.

(219) S. Lin, X. Ye, R. S. Johnson and H. Guo, *J. Phys. Chem. C,* 117 **(2013),** 17319.

(220) Q. Sun, Z. Li, D. J. Searles, Y. Chen, G. M. Lu, and A. Du, *J. Am. Chem. Soc.,* 135, **(2013)**, 8246.

(221) R. Laskowski, P. Blaha and K. Schwarz, *Phys. Rev. B,* 78 (**2008**), 045409

(222) A. Lyalin, A. Nakayama, K. Uosaki, and T. Taketsugu, *J. Phys. Chem. C,* 117 (**2013**), 21359.

(223) M. Gao, A. Lyalin, and T. Taketsugu, *Catalysts,* 1 **(2011),** 18.

(224) M. Gao, A. Lyalin, and T. Taketsugu, *J. Phys. Chem. C,* 116 **(2012)**, 9054.

(225) P. Wang, S. Orimo, T. Matsushima, and H. Fujii, *Appl. Phys. Lett.*, 80 **(2002),** 318.

(226) R. Ma, Y. Bando, H. Zhu, T. Sato, C. Xu, and D. Wu, *J. Am. Chem. Soc.,* 124, **(2002)**, 7672.

(227) C. C. Tong, Y. Bando, X. X. Ding, S. R. Qi, and D. Golberg, *J. Am. Chem. Soc.*, 124 **(2002)**, 14550.

(228) S.-H. Jhi, and Y.-K. Kwon, *Phys. Rev. B,* 69 **(2004)**, 245407.

(229) G. Mpourmpakis, and G. E. Froudakis, *Catalysis Today*, 120 **(2007),** 341.

(230) Q. Weng, X. Wang, C. Zhi, Y. Bando, and D. Golberg, *ACS Nano*, 7 **(2013),** 1558.

(231) S. A. Shevlin, and Z. X. Guo, *Appl. Phys. Lett.*, 89 **(2006)**, 153104.

(232) E. Durgun, Y.-R. Jang, and S. Ciraci, *Phys. Rev. B,* 76 **(2007)**, 073413.

Chapter 2

EXPERIMENTAL

2.1 Chemicals

Ultrapure reagent grade H_2SO_4, isopropyl alcohol (IPA), and acetone were purchased from Wako Pure Chemicals. Water was purified using a Milli-Q system (Yamato, WQ-500). Boron Nitride (BN) (10 μm) powder (99%) was purchased from High Purity Chemicals (BBIO3PB4). n-Si (111) wafers (P-doped, resistivity of 1-10 Ω) were donated by Shin-Etsu Semiconductor. Glassy carbon (GC) (10 x 10 x 1 mm) was purchased from BAS (No. 012825). $HAuCl_4$, $NaBH_4$, $NiCl_2$, Ethanol were purchased from Wako pure chemicals.

2.2 Substrate preparation

1 cm^2 size of n-type Si(111) was precleaned by sonication in acetone and Milli-Q water about 5 min each and then thoroughly rinsed with conc. sulfuric acid and Milli-Q water. The precleaned n-type Si(111) fixed in the holder, a 150 nm thickness of Au and Pt were sputter deposited on it by radio frequency (RF) magnetron sputtering (JSP-8000, ULVAC, 450 W RF power) in an Ar (20 sccm) atmosphere. The rotation rate of substrate holder was 10 rpm and the deposition rate was 0.1 Å sec^{-1}. Before the metal deposition on n-type Si(111) a 20 nm thick Ti was deposited as an adhesion layer. These metal deposited substrates were used as working electrode for electrochemical measurements. A gold single crystal prepared by the Clavilier method [1, 2] using a gold wire (99.999% pure, ϕ= 1 mm, Tanaka Precious Metal) was used as a substrate for atomic force microscopic (AFM) measurements.

2.3 Sample preparation

2.3.1 Sonication assisted solvent dispersion of boron nitride nanotubes (BNNT)

Boron nitride nanotubes (BNNTs) donated by Dr. Golgberg, NIMS [3] are dispersed as follows. Micrometer size BN nanotubes were dispersed in IPA by sonication with the output power of 270 W (As one, 60-70 Hz). 3 mg/ml as initial concentration of BN nanotubes were taken in a glass bottle and treated in ultrasonic bath for 48 hr at room temperature. This

resulted milky white dispersion of BN. The resultant dispersion was centrifuged at 1500 rpm for 45 min. After, centrifugation the top two thirds of the dispersion was collected by pipette. For the electrochemical measurements, 5 µl of the BN dispersion spin coated on working electrode substrates like Au, Pt and GC initially at 500 rpm for 2 min and then at 1500 rpm for 1 min. Then the substrates were dried at 100^{o}C in an electronic furnace for 30 min and used as working electrode for electrochemical measurements.

2.3.2 Sonication assisted solvent exfoliation of boron nitride nanosheets (BNNS)

BNNS were prepared as follows. Sonication assisted liquid exfoliation method was used to obtain BNNS [4-7] as shown in Figure 2.1. 60 mg of BN powder was taken in a glass bottle contains 20 ml of IPA (3 mg/ml as initial concentration). It was then treated in an ultrasonic bath for 96 hr with the output power of 270 W at room temperature. The resulted milky white solution was then centrifuged at 1500 rpm for 45 min.

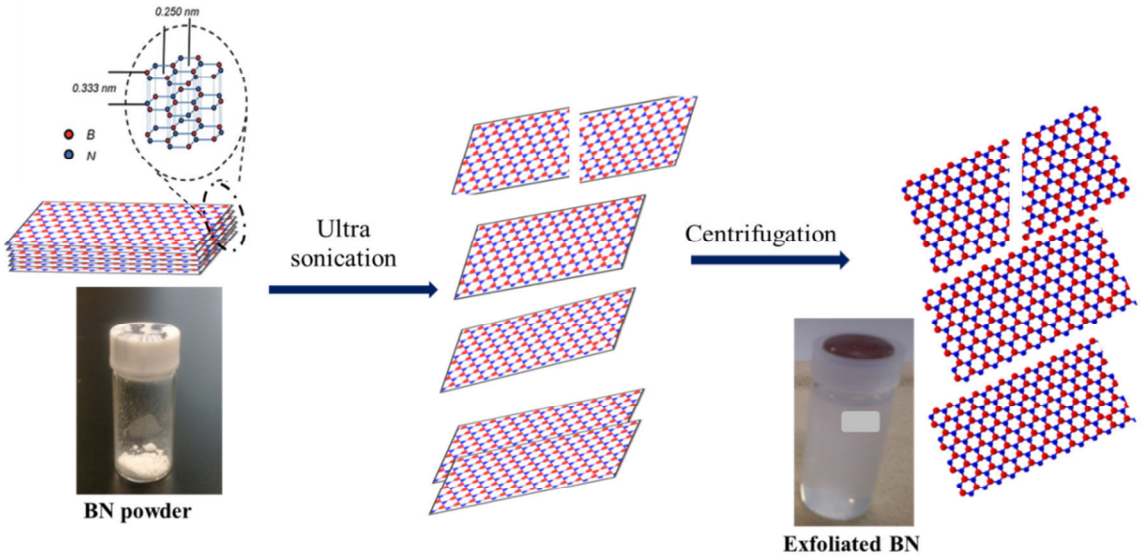

Figure: 2.1 Schematic of liquid exfoliation of BN nanosheets.

After centrifugation the top two thirds of the dispersion were collected by pipette. For the electrochemical measurements, 5 µl of the BN dispersion was pipetted out and dropped on working electrode substrates like Au, Pt and GC then it was spin coated initially at 500 rpm for 2 min and then at 1500 rpm for 1 min. Then substrates were dried at 100^{o}C in an electronic furnace for 30 min and used as working electrode for electrochemical measurements.

2.3.3 Sputter deposition

BN thin films [8, 9] were deposited on the Au thin film and Au(111) single crystals by RF magnetron sputtering using a commercially available BN target (ϕ= 4 inch, 99% purity, Jsputter) in Ar atmosphere (20 sccm) at room temperature with the substrate holder rotation rate of 10 rpm and the deposition rate of 0.1 Å sec^{-1}. Amount of deposited BN films were controlled by varying the deposition time; 50, 100, and 500 sec. The schematic of Au and BN sputter deposition is shown in Figure 2.2.

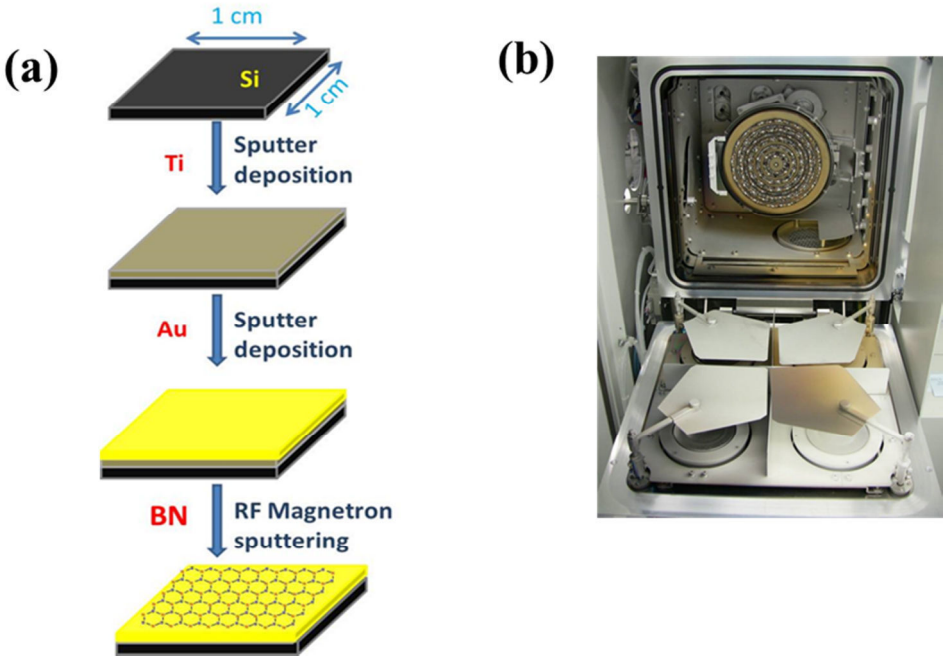

Figure: 2.2(a) Schematic of sputter deposition and (b) open view of the chamber

2.3.4 BNNS decorated with metal nanoclusters

BNNS were prepared by Hummer's method [10, 11]. Briefly, 2 g of BN powder was dispersed in 9 ml of conc. HNO_3 in a conical flask by sonication about 30 min and then the dispersion was kept in an ice bath with constant stirring. 18 ml of conc. H_2SO_4 was added drop by drop into the dispersion with continuous stirring then 10 mg of $KMnO_4$ ($KMnO_4$ crystals was powdered by mortar) powder was added slowly ca. 1 hr. The reaction mixture was left in an ice bath with continuous stirring for 5 days. Afterwards the reaction mixture was diluted, rinsed and washed thoroughly with ultrapure water and dried it at 100^{o}C for 24

hr. And then the BN sample was taken in an alumina boat, thermally treated at 1050^{o}C in an Ar atmosphere in a quartz tubular furnace ca. 1 hr. 60 mg of thermally treated BN nano sheets were sonicated in 20 ml of IPA ca. 3 h. The resulted solution was stirred with 4 ml of 10 mM $HAuCl_4$ or $NiCl_2$ solution added at room temperature in N_2 atmosphere ca. 30 min. Then 2 ml of 50 mM $NaBH_4$ solution added drop by drop to the above reaction mixture, the solution turned into black colour and continued the stirring for 4 hr [12-14]. The obtained material was filtered and washed several times with water and ethanol, after filtration BNNS decorated with Au-nanoclusters (Au/BNNS) (pink colour) or BNNS decorated with Au-nanoclusters (Ni/BNNS) (greenish blue colour) materials were obtained and dried in a vacuum chamber overnight at 100^{o}C.

3 mg/ml of Au or Ni decorated BNNS were dispersed in IPA by sonication ca. 30 min. Surface modification by Au-BNNS and Ni-BNNS were carried out by spin coating of 5 µl of dispersion of BNNS decorated with Au- or Ni-NCs on Au, Ni, Pt or GC substrates, initially at 500 rpm for 2 min and then at 1500 rpm for 1 min. Then the substrates were dried at 100^{o}C in an electronic furnace for 30 min and used as working electrode for electrochemical measurements.

2.4 Scanning Electron Microscopy (SEM), Transmission Electron Microscopy (TEM) and Atomic Force Microscopy (AFM) measurements

SEM with field emission scanning electron microscope (FE-SEM: S-4800, Hitachi). 5 µl of Liquid exfoliated BNNS were spin coated on Au substrate as described in section 2.3.2 and dried at 100^{o}C in an electronic furnace ca. 30 min. The morphology and coverage of spin coated BN nanosheets were observed by SEM. The sample morphologies were characterized by accelerating voltage of 2-5 kV and emission current in the range of 10 mA.

TEM is used for characterization of the internal microstructure of BNNS and BNNS decorated with Au- or Ni-NCs. High resolution transmission microscopy (HRTEM) was carried out by JEOL-JEM-2100F with power of 200 keV. A drop of liquid exfoliated BNNS and ethanol dispersed Au and/or Ni- nanoclusters decorated BNNS were dropped on mesh type Cu grid and dried at 100^{o}C in an electronic furnace ca. 10 min. Closely packed atomic arrangements, defects, zigzag and armchair edge structures were observed by HRTEM. Fast Fourier transform (FFT) and Electron energy loss spectroscopy (EELS) used to measure the structure and composition of BN using the same instrument.

The thickness and current trace of the liquid exfoliated BNNS were measured using AFM (Agilent 5500). 1 µl of liquid exfoliated BNNS was dropped on Au (111) surface and dried at 100^{o}C in an electronic furnace 10min. For conducting AFM, Pt coated silicon nitride cantilever (PPP-FM, typical spring constant: 2.8 N/m, resonance frequency: 75 kHz, Nanosensors) was used. Bias voltage for conductance measurement was +0.4 V.

2.5 Raman measurements

Raman scattering measurements of bulk BN and liquid exfoliated BNNS were carried out using Horiba-Join-Yvon, model-T64000 with Ar-Kr laser (514.5 nm, 0.1 W) with exposure time of 10 s. Resolution is 0.5 nm and the magnification was 90 X 20 (objective length X eye piece length). Raman spectrum was carried out between 800 cm^{-1} to 1800 cm^{-1}. It was reported that the Raman peak is usually shifted in higher Raman shift in monolayers and lower Raman shift in bilayers with respect to its position in bulk h-BN [15]. It was also widely studied that BN has a characteristic peak near to 1370 cm^{-1} is attributed to the B-N vibrational mode (E_{2g}) within h-BN layers [15].

2.6 X-ray diffraction (XRD), X-ray photoelectron spectroscopy (XPS) analysis

BNNS and Au decorated BNNS was investigated by XRD analysis under ambient conditions in an X'Pert Pro system (PANalytical) using monochromatic Cu-Kα radiation λ=1:5406 Å. Scan angle is 10 to 90 degree. Scan speed is 2 degree min^{-1}. And the step of scan is 2 degree. The average crystallite size of Au clusters was calculated using the Debye Scherrer formula,

$$d = K\lambda / \beta \cos(\theta) \qquad (2.1)$$

where d is the crystallite size, λ is the wavelength of the X-ray radiation, K is usually taken as 0.89, 2θ is the Bragg angle, and β is the line width at half-maximum height.

BNNS and Au- and/or Ni-NCs decorated BNNS were also investigated by XPS analysis (Thermo Electron Co.) using an Al-Kα X-ray source (15 keV). The take-off angle between the sample surface and the analyzer was 90^{o}. Boron 1s spectrum was measured from 180 eV to 196 eV, Nitrogen 1s spectrum was measured from 392 eV to 410 eV, Au 4f

spectrum was measured from 80 eV to 94 eV, and Ni 2p peak was measured from 845 eV to 885 eV.

2.7 Electrochemical Measurements

2.7.1 Oxygen reduction reaction

2.7.1.1 Rotating Disk Electrode (RDE) measurements

The rotating disk electrode is one of the potential equipment's to study the kinetics of ORR [16-20]. The configuration of the disk electrode is shown in Fig. 2.3. The metal disk electrode is embedded into Teflon. During the rotation the spinning disk pulls the fluid at the electrode surface because of the centrifugal force, and throws away the electrolyte solution outward from the center in a radial direction [16]. The diffusion rate of the electrolyte solution and the thickness of the diffusion layer are controlled by the rotation rate. Rotation brings the fresh analyte to the electrode surface, if the rotation rate increases the thickness of reactant's diffusion layer also increase, results increase in current density. As a result of this one can obtain rotation rate dependent diffusion limiting current with respect to potential. A diffusion limiting current usually can be observed in the higher overpotential region.

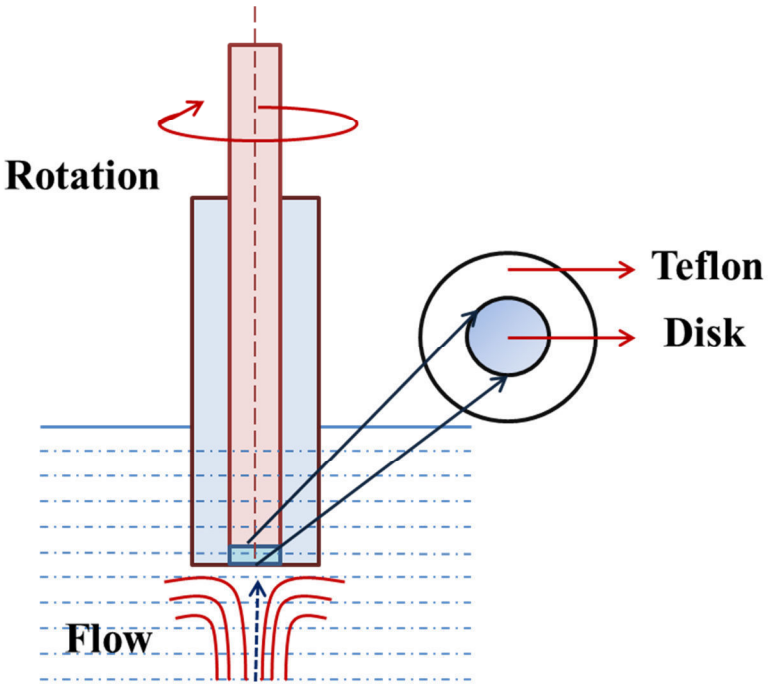

Figure: 2.3 Configuration of rotating disk electrode.

The relationship between the diffusion limiting current and the rotation rate at a given potential (Levich equation) is given by equation (2.2).

$$i_L = 0.620\text{n}FAD^{2/3} v^{-1/6} C\omega^{1/2} \quad (2.2)$$

where i_L is the diffusion limited current, n is the number of electrons transferred in the overall reaction process, F is the Faraday constant (96490 C mol^{-1}), A is the surface area of the disk electrode, v is the kinematic viscosity (0.01cm^2s^{-1}), D is the diffusion coefficient of oxygen molecules, C is the bulk concentration of the oxygen (1.1 x 10^{-6} mol cm^{-3}), ω is the rotation rate [16-20].

The kinetic current (i_k) in the absence of any mass transfer [21] is given by equation (2.3)

$$1/i = 1/i_k + 1/i_L \quad (2.3)$$

$$i_k = \text{n}\, F\text{A}kC \quad (2.4)$$

Therefore, a linear plot of $1/i$ versus $1/\omega^{1/2}$, i.e., Koutecky-Levich plot, can be obtained and extrapolated to $1/\omega^{1/2} = 0$ to yield $1/i_k$ [20, 21]. Then, the rate constant k can be obtained from equation (2.4).

Electrochemical measurements were carried out in a typical three electrode configuration as shown in Figure 2.4. A Pt wire and a Ag/AgCl (sat. NaCl) electrodes were used as a counter and a reference electrode, respectively. The above prepared electrodes were used as working electrode. A potentiostat/function generator (Hokuto Denko, HSV-100) and a speed control unit (Hokuto Denko, HR-202) were used to control the potential and the rotation speed of rotating disk electrode (RDE) [16-20]. Graphtec recorder (model: midi Logger GL900) used to record the current potential (i-v) polarization curve. All the electrochemical measurements were carried out in a 0.5 M H_2SO_4 an aqueous solution at room temperature. The electrolyte solution was saturated with Ar or O_2 by passing the ultrapure Ar or ultrapure O_2 gas at least for 1 hr to achieve an O_2 free or O_2 saturated condition before electrochemical measurements. The RDE voltammograms were recorded for ORR for various BN structures on Au, Pt and GC electrode surfaces by varying the potential from 0.6 to -0.1 V with a scan rate of 10 mV sec^{-1} and the rotation speed was varied from 0 to 3000 rpm. All electrodes were pre-treated by cycling the potential between -0.1 and +1.5 V in

Ar saturated 0.5 M H_2SO_4 electrolyte solution at a sweep rate of 100 mV sec^{-1} for 100 cycles to remove any surface contaminants before the ORR activity. Geometric surface area (0.5 cm^2) was used to calculate the current density.

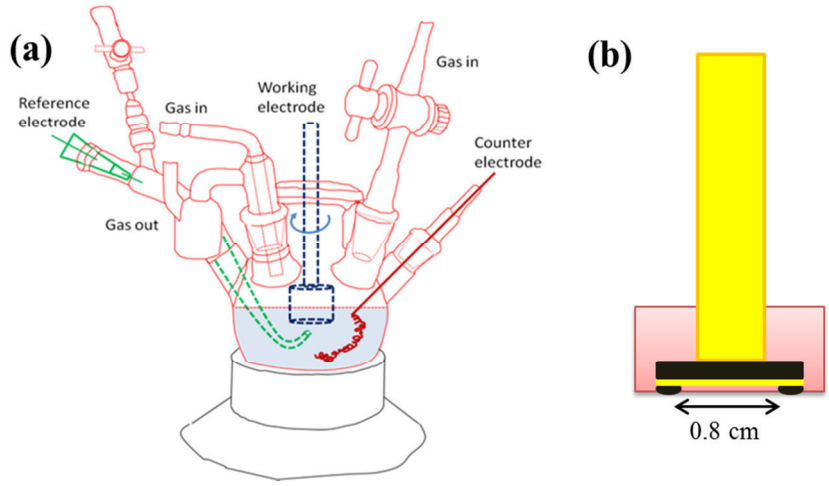

Figure: 2.4(a) Schematic of Electrochemical Cell. (b) Cross section view of working electrode.

2.7.1.2 Rotating Ring Disk Electrode (RRDE) Measurements

In the RRDE method, the O_2 reduction reaction occurring on the disk electrode produces intermediates, which can be detected on the ring and are used to presume the ORR mechanism [16, 22-24]. The difference between a rotating ring-disk electrode and a rotating disk electrode is the addition of a second working electrode in the form of a ring around the central disk of the first working electrode. The two electrodes are separated by an insulator and connected to the potentiostat. To operate such an electrode it is necessary to use a bipotentiostat or some potentiostat capable of controlling a four electrode system [16, 22-24].

The RRDE takes advantage in the form of laminar flow created during rotation. As the system is rotated the solution in contact with the electrode is pull towards the electrode surface as same as with a rotating disk electrode. As the solution flows to the side it crosses the ring electrode and back into the bulk of the solution. If the solution is flow in the radial direction then the solution can brought into the contact with the disk quickly followed by the ring in a very controlled manner as shown in Fig. 2.4. The resulting currents are dependent on

the electrodes respective potentials, areas, and spacing as well as the rotation rate and a given substrate [16].

This design makes a variety of experiments possible, for example a complex could be reduced at the disk and then oxidized back to the starting material at the ring. It is easy to predict what the ring/disk current ratios, if this process is entirely controlled by the flow of solution [16].

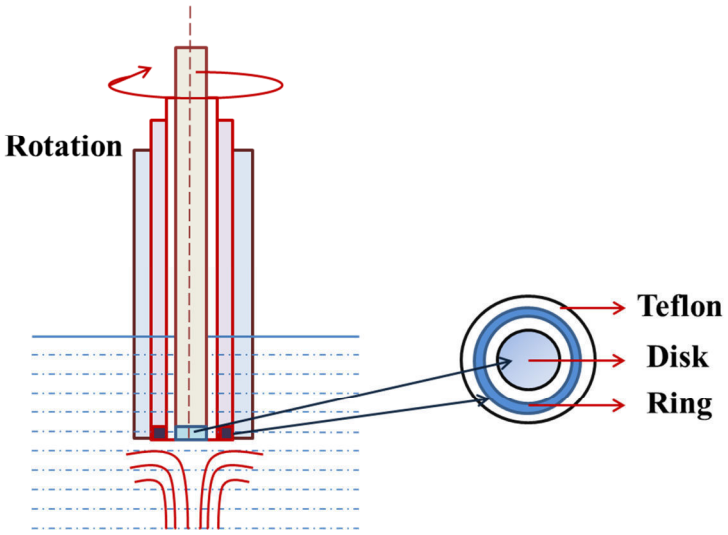

Figure: 2.4 Configuration of rotating ring disk electrode.

Collection efficiency: The collection efficiency of a RRDE system can be measured using a well-behaved redox system. The ferrocyanide/ferricyanide half reaction is a simple, single-electron, reversible half reaction that is often used as the basis for measuring collection efficiency. The RRDE is placed in a solution containing a 10 mM of $K_3Fe(CN)_6$ in a 1 M KNO_3 solution. The electrochemical measurements were carries out from +0.6 to -0.4 V at the rotation rate from 0 to 2400 rpm with the sweep rate of 10 mV sec^{-1}. When the potential swept slowly towards negative direction, a cathodic current is observed this corresponds to the reduction of ferricyanide to ferrocyanide at the disk as shown in Figure 2.5, equation (2.5).

$$Fe\,(CN)_6^{3-} + e^- \rightarrow Fe\,(CN)_6^{4-} \qquad (2.5)$$

As ferricyanide reduced at the disk electrode, the ferrocyanide generated by this process is swept (radially) outward away from the disk electrode and toward the ring electrode. The ring is held at a positive potential (+0.5 V) potential throughout the experiment. Some of the ferrocyanide generated at the disk travels close enough to the ring

electrode that it is oxidized back to ferricyanide. Thus an anodic current is observed at the ring electrode due to the oxidation of ferrocyanide to ferricyanide at the ring as shown in Fig. 2.5, equation (2.6)

$$Fe(CN)_6^{4-} + e^- \rightarrow Fe(CN)_6^{3-} \qquad (2.6)$$

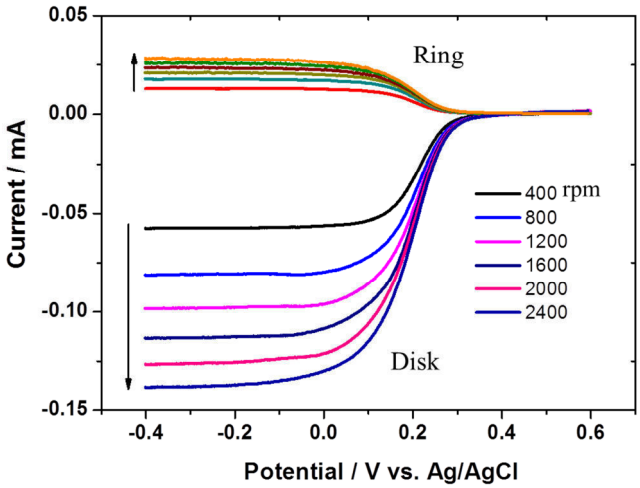

Figure: 2.5 Rotating ring disk voltammograms of ferro/ferricyanide system in in a solution containing a 10 mM of $K_3Fe(CN)_6$ in a 1 M KNO_3 solution at various rotating rate with the sweep rate of 10 mV sec^{-1}.

The collection efficiency was determined as N = I_{ring}/I_{disk} = 0.20, which was independent of disk potential and consistent with the theoretical collection efficiency provided by the manufacturer of the ring-disk electrode. The two-electron transfer reaction of O_2 reduction to H_2O_2, captured by the Pt ring, was analyzed in this work. The H_2O_2 produced at the disk is oxidized at the ring. The fraction of H_2O_2 formation $\chi_{H_2O_2}$ can be determined from the collection efficiency, ring and disk currents by the expression (2.7) [24].

$$\chi_{H_2O_2} = \frac{2I_{ring} / N}{I_{disk} + I_{ring} / N} \qquad (2.7)$$

A dual potentiostat/function generator (Hokuto Denko, HR-10113) and a speed control unit (Pine Research Instruments, AFMSRCE-2743) were used to control the potential and rotation rate of the rotating ring disk electrode (RRDE) (Pine Research Instruments, AFMSRCE-2743) [21-23]. Graphtec recorder (model: midi Logger GL900) used to record

the current potential (*i*-v) polarization curve. All the electrochemical measurements were carried out in a 0.5 M H_2SO_4 an aqueous solution at room temperature. The electrolyte solution was saturated with Ar or O_2 by passing the ultrapure Ar or ultrapure O_2 gas at least for 1 hr to achieve an O_2 free or O_2 saturated condition before electrochemical measurements. Pt electrode used as a ring electrode and Au and Pt electrodes were used as disk electrodes.

RRDE were recorded for ORR for BNNS and Au-NCs BNNS on Au electrode surfaces by varying the potential from 0.6 to -0.1 V and for Pt it was recorded from +1.0 to -0.1 V with a scan rate of 10 mV s^{-1} and the rotation speed was varied from 0 to 2500 rpm. All the measurements were carried out at room temperature. All electrodes were pre-treated by cycling the potential between -0.1 and +1.5 V in Ar saturated 0.5 M H_2SO_4 electrolyte solution at a sweep rate of 100 mV s^{-1} for 100 cycles to remove any surface contaminants before the ORR activity. Geometric surface area (disk: 0.19 cm^2 and ring: 0.008 cm^2) was used to calculate the current density.

2.7.2 Hydrogen Evolution and Oxidation Reaction (HER/HOR)

The linear sweep voltammograms (LSVs) were recorded for HER for BNNS and Au- and/or Ni-NCs decorated BNNS on Au, Pt and GC electrode surfaces by varying the potential from 0.2 to -0.9 V with a scan rate of 0.1 mV s^{-1}. All the electrochemical measurements were carried out in a 0.5 M H_2SO_4 an aqueous solution at room temperature. The electrolyte solution was saturated with Ar or O_2 by passing the ultrapure Ar or ultrapure H_2 gas at least for 1 hr to achieve an O_2 free condition before electrochemical measurements. The RDE voltammograms were recorded for HOR for BNNS and Au-decorated BNNS on Au and Pt electrode surfaces by varying the potential from -0.4 to 1 V with a scan rate of 1 mV s^{-1}. All electrodes were pre-treated by cycling the potential between -0.1 and +1.5 V in Ar saturated 0.5 M H_2SO_4 electrolyte solution at a sweep rate of 100 mV s^{-1} for 100 cycles to remove any surface contaminants before the HER activity. Geometric surface area (0.5 cm^2) was used to calculate the current density.

2.8 References

(1) J. Clavilier, R. Faure, G. Guinet, and R. Durand, *J. Electroanaly. Chem.,* 107 **(1980)**, 205.

(2) K. Uosaki, S. Ye, H. Naohara, Y. Oda, T. Haba, and T. Kondo, *J. Phys. Chem. B,* 101

(1997), 1051.

(3) D. Golberg, Y. Bando, C. Tang, and C. Zhi, *Adv. Mater.*, 19 **(2007**), 2413 and references therein.

(4) J. N. Coleman, M. Lotya, A. O'Neill, S. D. Bergin, P. J. King, U. Khan, K. Young, A. Gaucher, S. De, R. J. Smith, I. V. Shvets, S. K. Arora, G. Stanton, H. Y. Kim, K. Lee, G. T. Kim, G. S. Duesberg, T. Hallam, J. J. Boland, J. J. Wang, J. F. Donegan, J. C. Grunlan, G. Moriarty, A. Shmeliov, R. J. Nicholls, J. M. Perkins, E. M. Grieveson, K. Theuwissen, D. W. McComb, P. D. Nellist, and V. Nicolosi, *Science,* 331 (**2011**), 568.

(5) T. Sainsbury, A. Satti, P. May, Z. Wang, I. McGoven, Y. K. Gun'ko, and J. Coleman, *J. Am. Chem. Soc.,* 134 (**2012**), 18758.

(6) V. Nicolosi, M. Chhowalla, M. G. Kanatzidis, M. S. Strano, and J. N. Coleman, *Science,* 340 **(2013),** 1226419.

(7) W. Q. Han, L. Wu, Y. Zhu, K. Watanabe, and T. Taniguchi, *Appl. Phys. Lett*., 93 (**2008)**, 223103.

(8) W. Gessler, J. Haupt, A. Hoffmann, P. N. Gibson, and D. G. Rickerby, *Thin Solid Films*, 199 **(1991**) , 113.

(9) D. G. Rickerby, P. N. Gibbson, W. Gissler, and J. Haupt, *Thin Solid Films*, 209 (**1992)**, 155.

(10) W. S. Hummers, and R. E. Offeman, *J. Am. Chem. Soc.,* 70 **(1958),** 1339.

(11) H. Yin, H. Tang, D. Wang, Y. Gao and Z. Tang, *ACS Nano*, 6 **(2012)**, 8288.

(12) Y. Lin, C. E. Bunker, A. A. S. Fernando, and J. W. Connell, *ACS Appl. Mater. Interfaces,* 4 **(2012)**, 1110.

(13) L. Wang, C. Sun, L. Xu and Y. Qian, *Catal. Sci. Technol.,* 1 **(2011)**, 1119.

(14) L. Wang, L. Shen, X. Xu, L. Xu and Y. Qian, *RSC Adv.,* 2 **(2012)**, 10689.

(15) L. Britnell, R. V. Gorbachev, R. Jalil, B. D. Belle, F. Schedin, M. I. Katsnelson, L. Eaves, S. V. Morozov, A. S. Mayorov, N. M. R. Peres, A. H. C. Neto, J. Leist, A. K. Geim, L. A. Ponomarenko, and K. S. Novoselov, *Nano Lett.* 12 **(2012)**, 1707.

(16) A. J. Bard, L. R. Faulkner, "*Electrochemical Methods: Fundamentals and Applications*", 2nd Ed. **(2000)**, Wiley, New York.

(17) M. Kullapere, G. Jurmann, T. T. Tennno, J. J. Paprotny, F. Mirkhalaf, and K. Tammeveski, *J. Electroanal. Chem*., 599 (**2002)**, 183.

(18) K. E. Gubbins, and R. D. J. Walker, *J. Electrochem. Soc.*, 112 (**1965)**, 469.

(19) R. E. Davis, G. L. Horvath, and C. W. Tobias, *Electrochim. Acta*, 12 (**1967)**, 287.

(20) M. Harada, H. Noguchi, N. Zanetakis, S. Takakusagi, W. Song, and K. Uosaki, *Sci.*

Technol. Adv. Mater., 12 **(2011)**, 044606.

(21) N. M. Markovic, H. A. Gasteiger, and P. N. Ross, *J. Phys. Chem.*, 100 **(1996)**, 6715.

(22) N. M. Markovic, H. A. Gasteiger, and P. N. Ross, *J. Phys. Chem.*, 99 **(1995)**, 3411.

(23) O. Antoine and R. Durand, *J. Appl. Electrochem.*, 30 **(2000)**, 839.

(24) V. A. Sethuraman, J. W. Weidner, A. T. Haug, S. Motupally, and L. V. Protsailo, *J. Electrochem. Soc.,* 155 **(2008),** B50.

Chapter 3

ELECTROCATALYTIC ACTIVITY OF VARIOUS TYPES OF H-BN FOR OXYGEN REDUCTION REACTION

3.1 Introduction

Fuel cells (FCs) are considered to be one of the best possible energy conversion devices due to their high energy density, high theoretical efficiency, and negligible emission of exhaust gases [1]. The oxygen reduction reaction (ORR) has been extensively studied as it is the most crucial process in FCs [2-4]. Pt based ORR electrocatalysts are widely used because of their relatively low overpotential and high current density [5]. However, due to the high cost, less abundance, poor stability in electrochemical environment, and still sluggish kinetics of Pt based catalysts [5-10], there are worldwide research efforts to find precious metal free catalysts, such as non-precious metal [6-11], their alloys or oxides [12-14], metal oxides [15], metal nitrides [16, 17], metal oxynitrides [18, 19] and metal carbides [17, 20]. Non-precious metal or metal oxide catalysts are often suffered by dissolution, sintering, and agglomeration during fuel cell operation, resulting in the reduction of activity and durability [6-20]. This problem may be overcome by using metal-free carbon materials doped with N, B, P and/or I [21-29]. Particularly, N- and B-doped carbon materials have been demonstrated to be effective precious metal free ORR catalysts [27-28]. The enhanced catalytic activity of N-doped carbon against ORR was attributed to the electron accepting nature of N-species, which creates net positive charge on neighbouring carbon atoms, where O_2 is adsorbed [25, 26]. On the other hand, O_2 is considered to be adsorbed on B atom itself in the case of B-doped carbon due to electron accepting nature of B atom [27].

It was demonstrated that carbon electrode co-doped with B and N atoms has higher ORR catalytic activity than that doped with single element [27-29] and it was considered that B atoms stabilize the N impurity near the edge of the graphene cluster and make it more reactive [29]. When all the C atoms in graphene are substituted by B and N atoms as an extreme case, hexagonal boron nitride (h-BN) monolayer, which has a geometric structure similar to that of graphene, can be obtained [30]. Lyalin et al., have recently shown theoretically that N-doped h-BN monolayer can have electrocatalytic activity for ORR [30, 31]. However, since BN is an insulator with wide band gap (3.6 - 7.1 eV depending on

experimental methods) [32-34], it is known to be chemically inert [35, 36], it is essential to provide an electronic communication to the h-BN surface for BN based materials to be used as an effective electrocatalyst for ORR [30-31]. Recently, manipulation of the band structure of h-BN nano systems has attracted considerable interests because of possible applications of BN in nano electronics [34]. It has been demonstrated that the band gap in h-BN monolayer can be significantly reduced by B- and N-vacancies and impurity defects [37, 38]. Moreover, the atomically thin h-BN nanoribbons are shown to possess semiconducting properties due to doping like conducting edge states and vacancy defects [37]. More recently, electron tunnelling through ultrathin h-BN layers deposited on a gold surface was demonstrated as the current was exponentially dependent on the BN thickness [39]. Therefore, ultrathin BN nanosheet (BNNS) layers supported on conducting materials may act as an ORR active electrocatalyst as necessary conditions seem to be fulfilled.

Lyalin et al., have recently demonstrated that an inert h-BN monolayer can be functionalized and become catalytically active by nitrogen doping [31] and by attaching to a metal (Ni(111)) support [40] and readily bind to transition metal surfaces due to the mixing of the dz^2 metal orbitals with the N-p_z and B-p_z orbitals of h-BN [41,42]. Such mixing is responsible for a considerable modification of the electronic properties of h-BN monolayer supported on 3d, 4d, and 5d transition metal surfaces [40-42] and also affects the catalytic activity of small metal particles supported on h-BN [40-44]. It has been shown that Ni(111) substrate can dramatically change ability of h-BN to adsorb simple molecules and activate O-O bond in O_2 and OOH species [31], showing h-BN/Ni(111) is a good candidate for ORR catalyst. Nickel is, however, not stable in the potential region close to the onset of ORR and, therefore, not a good substrate to prove the theoretical prediction of possible electrocatalytic activity of BN for ORR. Thus, gold is selected as a substrate since it is very stable and also shows very low electrocatalytic activity for ORR in acidic solution.

3. 2 Results and Discussion

3.2.1 Theoretical investigations

Prof. Taketsugu's group performed the theoretical analysis of the electronic structure of the h-BN/Au(111) system and its ability to bind and activate the molecular oxygen. The catalytic activation of O_2 is the first and one of the most important steps for ORR [45]. The calculations are carried out based on DFT with the functional of Wu and Cohen [46]. The Au(111) surface is represented by the four-layer slab containing 7 ×7 unit cells of Au covered

by the 8×8 element of h-BN [30, 31]. It is demonstrated that h-BN monolayer weakly binds to the Au(111) surface with a binding energy of 0.06 eV per BN pair. Figure 3.1 shows the spin-polarized density of states (DOS) calculated for the free h-BN monolayer (Fig. 3.1(a)) and the h-BN monolayer supported on the Au(111) substrate (Fig. 3.1(b)). The calculation shows that the free h-BN monolayer has a wide band gap of 4.6eV (Figure 3.1(a)), which is within the highly dispersed experimental values [32, 33]. The calculated partial DOS (PDOS) of h-BN on Au(111) is slightly modified and a slight protrusion of the unoccupied BN states toward the Fermi level due to the interaction with Au is observed (Fig. 3.1(b)). A similar but much stronger effect resulting in formation of the gap states has been observed experimentally for h-BN adsorbed on Ni(111), Rh(111), and Pt(111) surfaces [47] and explained by the orbital mixing and electron sharing at the interface [41, 47, and 48]. Although O_2 can only physisorb on the h-BN/Au(111) in a triplet inactivated state similar to the adsorption on the unsupported h-BN, a metastable highly activated configuration of O_2 on h-BN/Au(111) with a binding energy of −0.05 eV is found, as shown in Fig. 3.1(c).

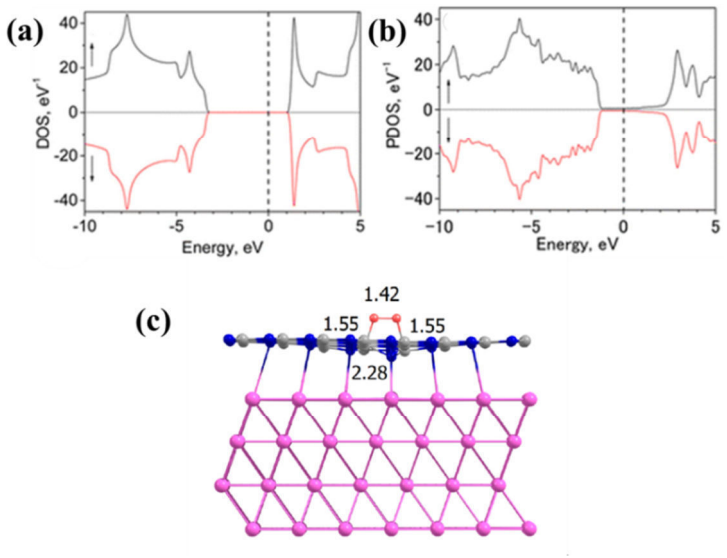

Figure: 3.1(a) Spin-polarized DOS calculated for the defect-free h-BN monolayer. (b) PDOS projected on B and N atoms for the h-BN/Au(111). The Fermi level is indicated by a dashed vertical line at 0 eV. Arrows directed upward and downward indicate the spin-up and spin-down DOS, respectively. (c) Optimized structure of the metastable O_2 on the h-BN/Au(111) surface with the distances given in angstrom.

In this case O_2 binds to two B atoms nearest to the N atom sitting on top of Au in the first metal layer. As a result of formation of the metastable O_2 on the h-BN/Au(111) surface,

the h-BN monolayer is strongly deformed and bends toward the metal surface. Therefore, adsorption of O_2 on h-BN/Au(111) can promote the local bonding of h-BN with Au(111). Since the above mentioned theoretical investigations suggest that BN on Au can act as an electrocatalyst for ORR, the ORR behaviour of Au modified by various types of BN were investigated as follows.

3.2.2 Gold electrode modified by boron nitride nanotubes (BNNT) and boron nitride nanosheets (BNNS)

3.2.2.1 TEM measurements of BNNT

TEM (a) and HRTEM images of (b-d) of the liquid exfoliated BNNT are shown in Figure 3.2. TEM images show that the BNNT walls were peel off after the sonication and producing a small amount of BN nanosheets. HRTEM images in Fig. 3.2(b-d) shows that the peeled of region of BNNT consists of multi-layered sheets with honeycomb lattice structure (hexagonal atomic structure). The fast Fourier transform (FFT) image of BNNT is shown inset in Fig. 3.2(b). The typical tubular structure with hexagonal atomic arrangements can be observed in FFT image. The multi-layered exfoliated BN sheets from BN nanotubes possess the zigzag and armchair edge structures [49] which are clearly observed in Fig. 3.2((c), (d)).

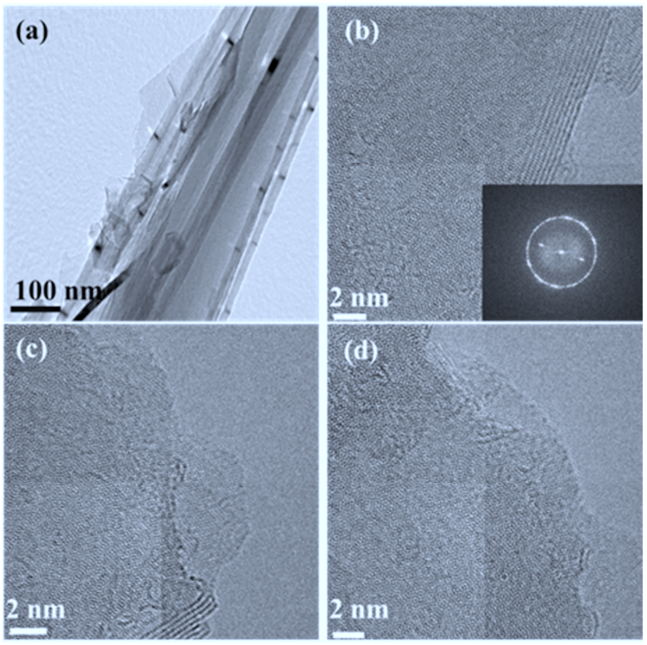

Figure: 3.2(a) TEM image of liquid exfoliated BNNT and (b-d) HRTEM images of liquid exfoliated BNNT. Inset in Fig. 3.2(b) is FFT of exfoliated BNNT.

3.2.2.2 SEM measurements of spin coated BNNT on Au

Fig. 3.3 shows SEM images of (a) bare Au surface prepared by RF magnetron sputtering and (b-d) the Au surface spin coated with IPA dispersed BNNT. BNNTs were observed all over the Au surface with some aggregation. The width and length of BNNTs were in the order of 100 nm and a few µm, respectively, as shown in Fig. 3.3(d).

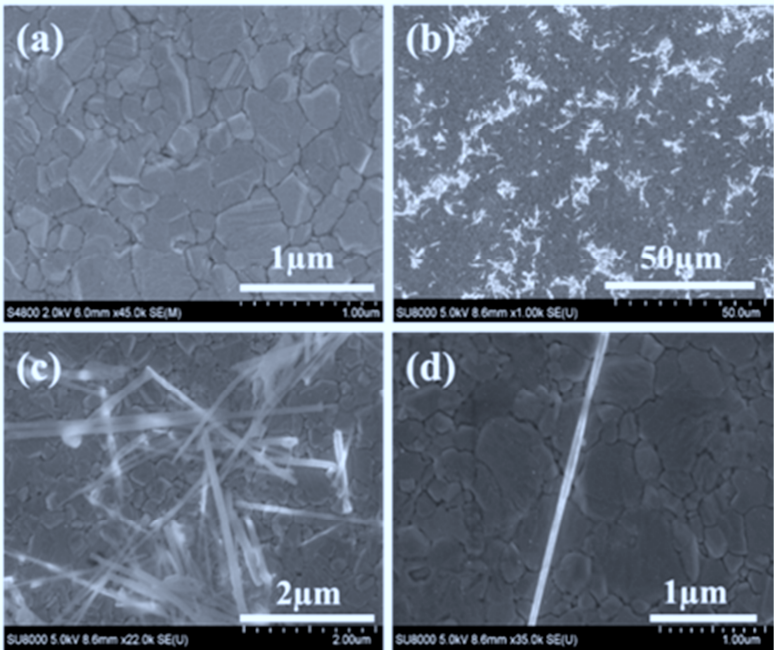

Figure: 3.3 SEM images of Au surface (a) without, (b-d) with spin coated dispersed BNNT.

3.2.2.3 TEM measurements and EELS spectrum of BNNS

TEM and HRTEM images of the liquid exfoliated BNNS are shown in Figure 3.4. HRTEM images in Fig. 3.4((c), (d)) shows that the BNNS consists of a single to a few layers with honeycomb lattice structure (hexagonal atomic structure) and the fast Fourier transform (FFT) image shown in Fig. 3.4(c) inset confirms that BNNS is composed of hexagonal atomic structure. Zigzag and armchair edge structures [49] are clearly observed in Fig. 3.4((c), (d)). Chemical composition and structure of the exfoliated BNNS were determined at the same time by electron energy loss spectroscopy. Observed spectrum shown in Figure 3.4(e) is similar to the previously reported EELS spectra which shows the characteristic K-edge absorptions of B- and N- atoms around 188-244 eV and 398-447 eV, respectively. A

sharp peak followed by wider band corresponding to 1s π* and 1s σ* transitions respectively, that is, the characteristics of sp^2 hybridization, indicating the hexagonal arrangements of BNNS [37].

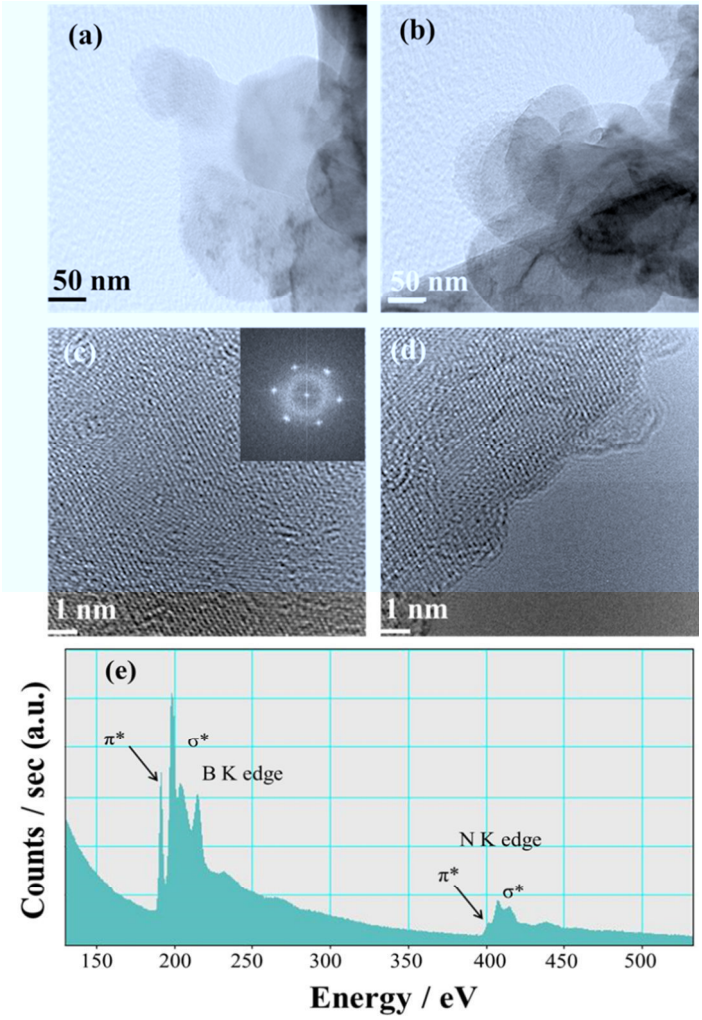

Figure: 3.4 TEM (a, b) and (b-d) HRTEM images of liquid exfoliated BNNS. Inset in (c) is the FFT of the image. (e) EELS spectrum of the exfoliated BNNS.

3.2.2.4 Raman measurements of BNNS

Raman spectrum of liquid exfoliated BNNS and bulk h-BN recoded at room temperature, excited by 514.5 nm laser. Figure 3.5 shows that the typical Raman spectra observed from bulk h-BN (Figure 3.5(a)) and liquid exfoliated BNNS (Figure 3.5(b)). At the lower frequency region a sharp peak at around 1376.7 cm^{-1} and 1369.4 cm^{-1} was observed for bulk and nanosheets of h-BN which is attributed to the B-N vibrational mode within h-BN

layers. Gorbachev et al. found that the Raman peak is usually shifted in upwards in monolayers and downwards in bilayers with respect to its position in bulk h-BN [50] as shown in Figure 3.5, suggest that the liquid exfoliation could make mono- to few layers of h-BN structures and the Raman shift is good agreement with the literatures [50].

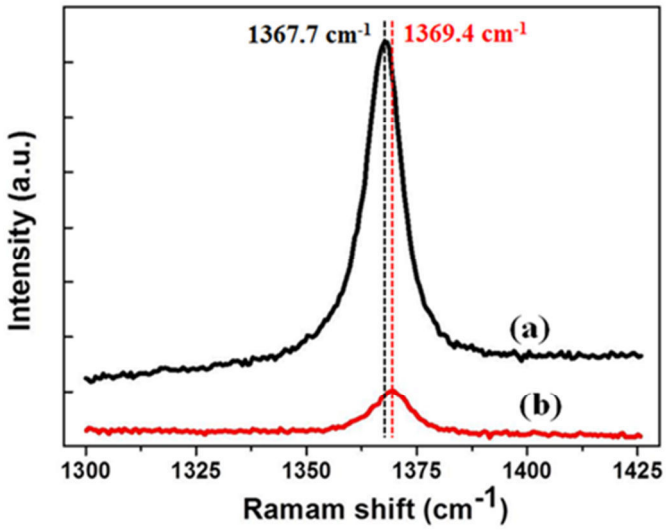

Figure: 3.5 Raman spectra of (a) BN powder and (b) BNNS deposited on Au.

3.2.2.5 SEM measurements of spin coated BNNS on Au

SEM images of BNNS modification spin coated on Au substrate are shown in Figure 3.6. Figure 3.6(a) shows that BNNS were uniformly distributed throughout the gold surface. The size of exfoliated BNNS was in the order of a few hundreds of nm in lateral dimension as shown in Fig 3.6((b), (c)).

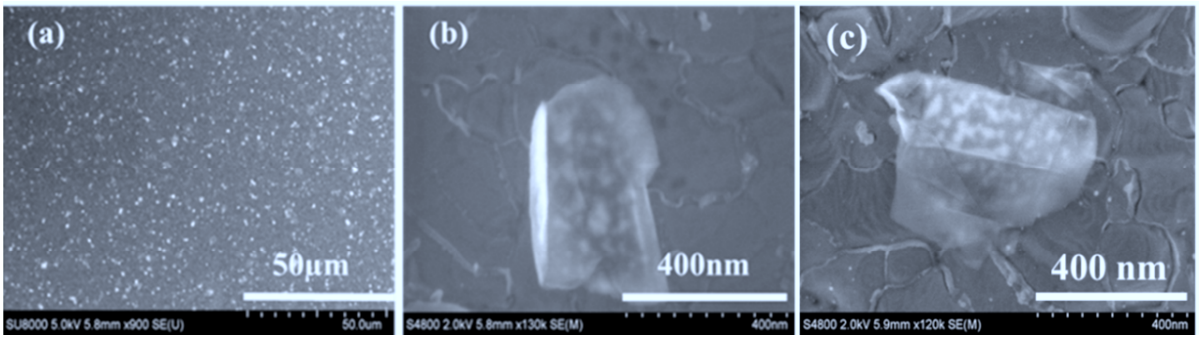

Figure: 3.6 SEM images of liquid exfoliated BNNS spin coated on Au substrate.

3.2.2.6 RDE measurements of BNNT and BNNS on Au

Figure 3.7 shows the LSVs of gold electrode (a) without, (b) with IPA dispersed BNNT, and (c) with liquid exfoliated BNNS, measured in an O_2 saturated 0.5 M H_2SO_4 solution with the rotation rate between 0 and 3000 rpm. Potential was scanned from +0.6 to -0.1 V at the scan rate of 10 mV sec^{-1}. At the bare Au, cathodic current due to ORR started to flow at around +0.25 V, increased as potential became more negative but no limiting current was observed in the potential region used in the present study.

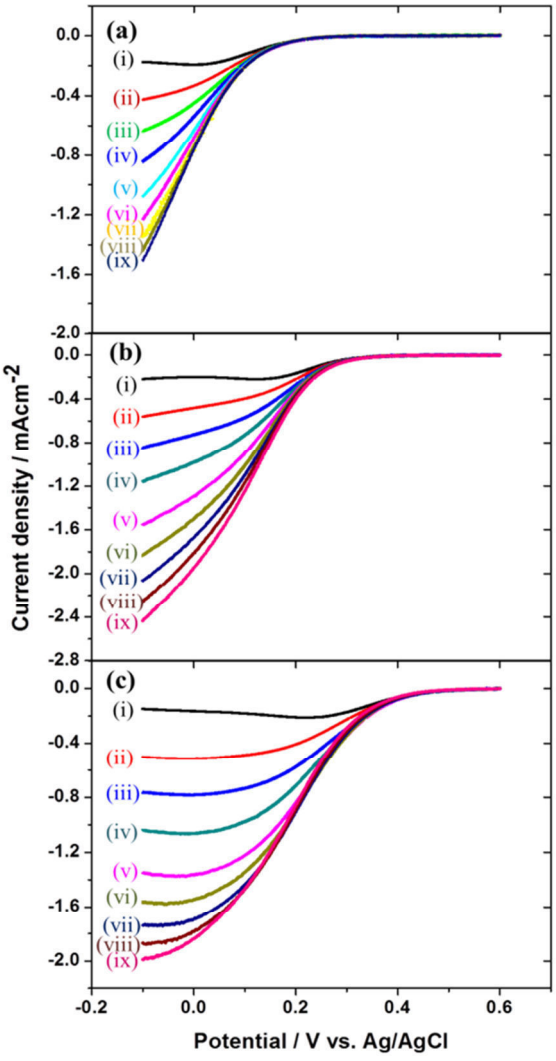

Figure: 3.7 LSVs of (a) bare, (b) BNNT modified, and (c) BNNS modified Au electrodes in O_2 saturated 0.5 M H_2SO_4 solution in rotating disk electrode (RDE) configuration with rotation rate of (i) 0, (ii) 100, (iii) 250, (iv) 500, (v) 1000, (vi) 1500, (vii) 2000, (viii) 2500, and (ix) 3000 rpm. Sweep rate: 10 mV sec^{-1}.

At the BNNT coated Au, the cathodic current observed at around +0.35 V and increased as potential became more negative but no limiting current was observed in the potential region used in the present study. It is clear that ORR activity was enhanced by BNNT modification. Further enhancement was observed at the BNNS coated Au where the cathodic current started to flow at around +0.52 V. In contrast to the bare Au and BNNT coated Au electrodes, the limiting current was observed at around +0.05 V.

Differences in the ORR activity can be seen more clearly in Fig. 3.8, which shows LSVs at (i) bare, (ii) BNNT coated, and (iii) BNNs coated Au electrodes with the rotation rate of 1500 rpm. The potentials at which ORR current of -0.02 mA cm^{-2} flowed was 0.22, 0.32, and 0.49 V at the bare, BNNT coated, and BNNS coated Au electrodes, respectively. Although overpotential for ORR was reduced by both BNNT and BNNS modifications, much larger effect was observed by BNNS modification (0.1 V reductions by BNNT vs. 0.25 V reductions by BNNS). This difference may be due to the very limited number of B- and/or N-edge structure in BNNT [37]. Theoretical calculations suggest the important role of edge structures as O_2 can be adsorbed in highly activated state at the edge of BN island. As shown in Fig. 2((b), (c)), BNNT has very high aspect ratio with very low fraction of the edge compared with that of BNNS (Fig. 4(c), (d)), resulting in very small number of active sites at BNNT. Furthermore, poor contact of BNNT with Au surface may also contribute to the lower activity as electronic communication between Au and BN is required to reduce O_2 and due to the curvature of BNNT, contact area and, therefore, the electronic communication of BNNT must be smaller than those of BNNS.

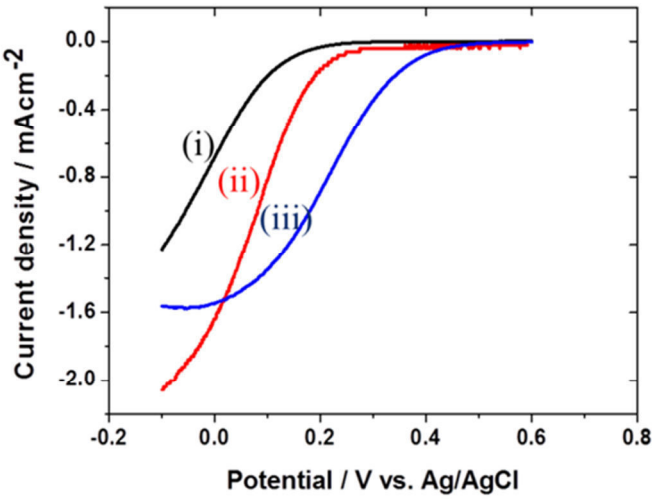

Figure: 3.8 LSVs of (i) bare, (ii) BNNT modified, and (iii) BNNS modified Au electrodes in O_2 saturated 0.5 M H_2SO_4 solution in RDE configuration with rotation rate of 1500 rpm. Sweep rate: 10 mV sec^{-1}.

3.2.3 Gold electrode modified by RF sputtered Boron Nitride (BN)

3.2.3.1 RDE measurements of various thickness of sputter deposited BN

To clarify the effects of contact between BN and Au and the thickness of BN, ORR activity of Au on which BN was sputter deposited was examined. Fig. 3.9(a) shows the rotation rate dependent LSVs of Au coated with BN sputter deposited for (a) 50, (b) 100 and (c) 500 s in O_2 saturated 0.5 M H_2SO_4 solution with various rotation rates. Potential was scanned from +0.6 to -0.1 V.

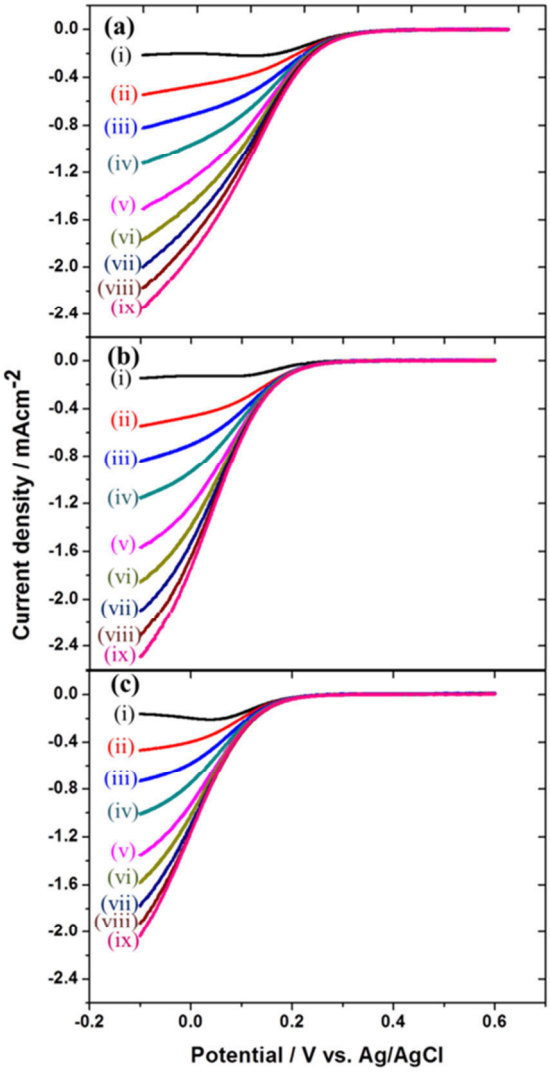

Fig. 3.9 LSVs of Au electrode on which BN was sputter deposited for (a) 50, (b) 100 and (c) 500 s in O_2 saturated 0.5 M H_2SO_4 solution in rotating disk electrode RDE configuration with rotation rate of (i) 0, (ii) 100, (iii) 250, (iv) 500, (v) 1000, (vi) 1500, (vii) 2000, (viii) 2500, and (ix) 3000 rpm. Sweep rate: 10 mV sec^{-1}.

By comparing with the results at the bare Au shown in Fig. 3.10, it is clear that ORR activity was enhanced in all the cases. To compare the results easier, LSVs of (i) bare and BN sputter deposited Au electrodes with sputtering time of (ii) 50, (iii) 100 and (iv) 500 s with rotation rate of 1500 rpm were shown in Fig. 3.10. The potentials at which ORR current of -0.02 mA cm^{-2} flowed was 0.37, 0.30, and 0.24 V at Au electrodes with RF sputtered BN for 50, 100, and 500 s, respectively. They were more positive than that at the bare Au, which is 0.15, 0.08, and 0.02 V for 50, 100, and 500 s sputter deposited BN. Thus, the ORR activity was less compared to those of BNNT and BNNS modified Au despite the expected better contact with Au substrate. The highest activity was observed when the deposition time was shortest, i.e., 50 s.

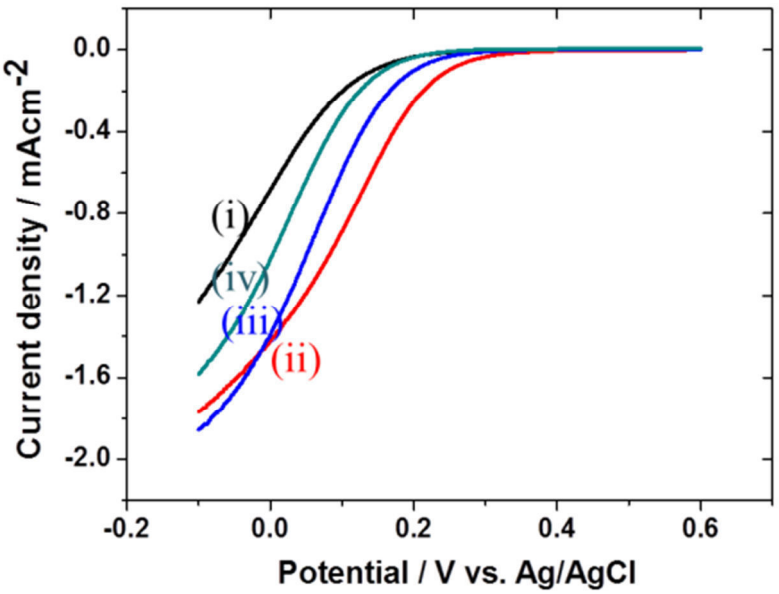

Figure: 3.10 LSVs of (i) bare and (ii – iv) BN sputter deposited Au electrode with sputtering time of (ii) 50, (iii) 100 and (iv) 500 s measured in O_2 saturated 0.5 M H_2SO_4 solution in RDE configuration with rotation rate of 1500 rpm. Sweep rate: 10 mV sec^{-1}.

3.2.3.2 AFM measurements

I, intended to deposit uniform BN films of 1, 2, and 10 nm thick by 50, 100, and 500 s deposition so that the thickness dependence of ORR activity can be studied quantitatively, BN nanoclusters of ca. 100 nm in diameter and 2-5 nm in height were deposited on Au surface as shown by AFM topography image in Fig. 3.11 regardless of deposition time [51, 52].

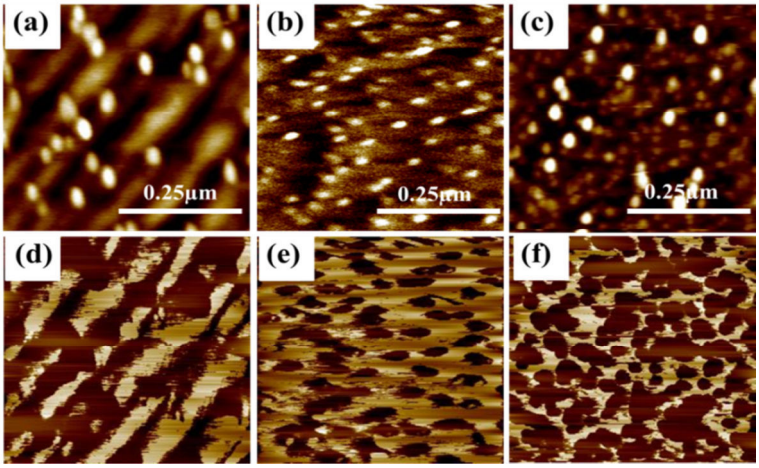

Figure: 3.11((a), (b), and (c)) AFM topography and ((d), (e), and (f)) conductance images of Au (111) surface on which BN was sputter deposited for 50 s, 100 s and 500 s respectively.

As the deposition time increased, the sizes of BN nanoclusters did not change much but the number of the clusters increased. Current image shows that no current flowed on the sputter deposited BN surface, showing it is insulating as BNNS [53]. Thus, ORR active site should be the edge of BN in this case as well and one expects the increase of active region and, therefore, ORR activity with the increase of the BN nanoclusters but experimental results showed other way round. Preparation of BN sputtered Au with much shorter deposition time and more careful surface analysis are under way to clarify the origin of deposition time dependence of ORR activity.

3.2.4 Quantitative comparisons

3.2.4.1 K-L plots

For a more quantitative analysis, one needs to obtain the potential dependent rate constant of ORR. The current potential relations can be analysed with the following Koutecky-Levich (K-L) [54, 55] equation:

$$1/i = 1/i_k + 1/B\omega^{1/2} \quad (3.1)$$

$$B = 0.620nFC_{O2}D^{2/3}v^{-1/6} \quad (3.2)$$

where n is the number of electrons transferred in the overall reaction process, F is the Faraday constant (96490 C mol^{-1}), v is the kinematic viscosity (0.01 cm^2 s^{-1}) [56], D is the

diffusion coefficient of oxygen molecule, C_{O2} is the bulk concentration of the oxygen (1.1 x 10^{-6} mol cm^{-3}) [57, 58], ω is the rotation rate, and i_k is the kinetic current without any mass transfer limitation, which is given by

$$i_k = nFAkC_{O2} \tag{3.3}$$

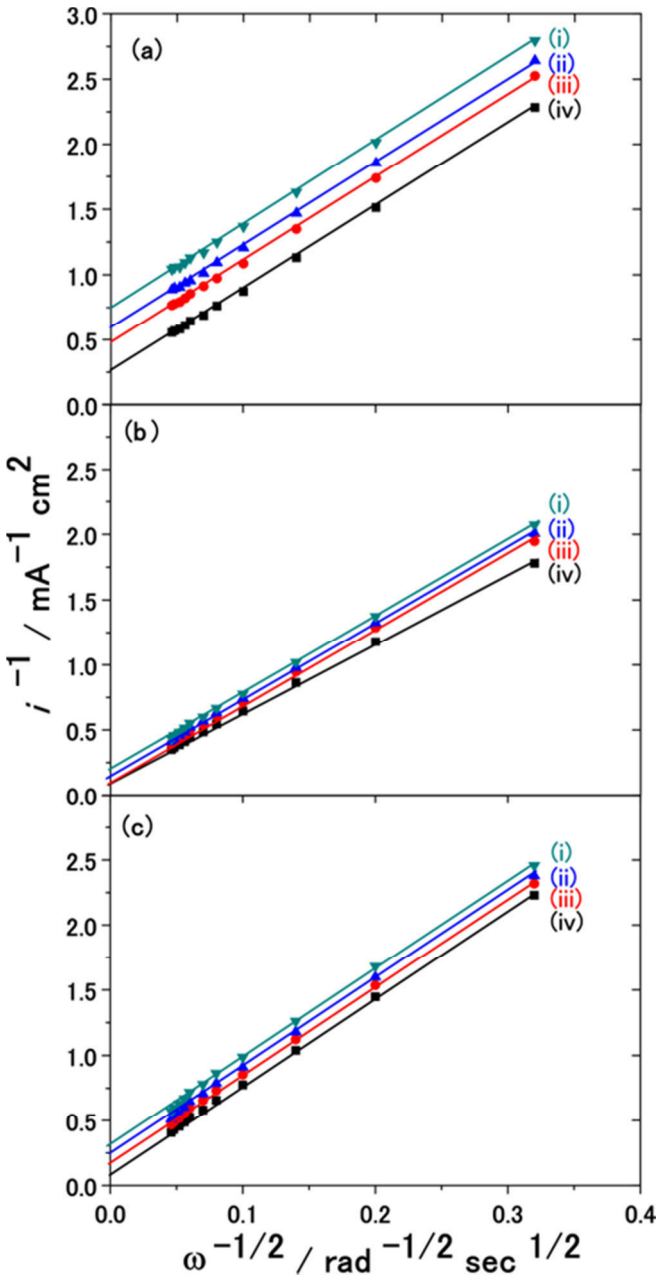

Fig. 3.12 Koutecky-Levich plots of (a) bare, (b) BNNT modified, and (c) BNNS modified Au electrodes in O_2 saturated 0.5 M H_2SO_4 solution at (i) -0.02, (ii) -0.04, (iii) -0.06, and (iv) -0.10 V.

Therefore, a linear plot of $1/i$ versus $1/\omega^{1/2}$ can be extrapolated to $1/\omega^{1/2} = 0$ to yield $1/i_k$. Then, the rate constant k can be obtained from equation (3.3). Fig. 3.12 shows the K-L plots for the (a) bare, (b) BNNT modified, and (c) BNNS modified Au electrodes using the results of Fig. 3.6. Linear relations were observed in all cases and the number of electrons transferred (n) was calculated to be ca. 2 from the slopes of the K-L plots in all the cases, indicating that O_2 is reduced to hydrogen peroxide at these electrodes as shown in equation (3.4). The kinetic current, i_k, at a given potential can be obtained from the intercept of the K-L plot.

$$O_2 + 2H^+ + 2e^- \rightarrow H_2O_2 \qquad (3.4)$$

3.2.4.2 Tafel plots

Tafel plots obtained from K-L plots are shown in Fig. 3.13. Single well-defined linear regions were observed at all electrodes except at the BNNS modified Au electrode where two well-defined linear regions were observed. The Tafel slopes and exchange current densities at bare, BNNT modified, BNNS modified, and BN sputter deposited (50, 100, 500 s) Au electrodes in O_2 saturated 0.5 M H_2SO_4 solution are summarized in Table 1.

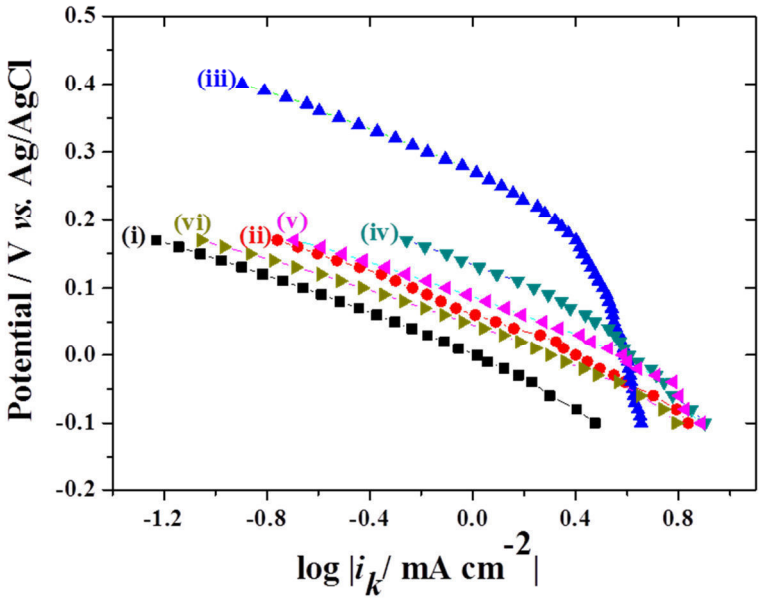

Fig. 3.13 Tafel plots of (i) bare, (ii) BNNT modified, (iii) BNNS modified, (iv) BN sputter deposited (50 s), (v) BN sputter deposited (100 s), and (vi) BN sputter deposited (500 s) Au electrodes in O_2 saturated 0.5 M H_2SO_4 solution derived from the intercepts of K-L plots at various potentials.

The exchange current density at the BNNS modified Au electrode (1.53×10^{-4}) is four orders of magnitude higher than that at the bare Au electrode (6.31×10^{-8}), suggest that the electron transfer rate at BNNS/Au is faster than at the bare Au electrode and which significantly increase the power output in the FC system. The slopes are obtained between -125 and -135 mV dec^{-1} at all electrodes except at the BNNS modified Au electrode where the slope is -86 mV dec^{-1} at low overpotential region (> +0.2 V). The slope at the BNNS modified Au electrode in high overpotential (< +0.2 V) region is -220 mV dec^{-1}. These results show that the ORR mechanism at the BNNS modified Au electrode is different from those at other electrodes. The Tafel slope at BNNS modified Au electrode in low overpotential region is close to that at Pt electrode, which is approximately -60 mV dec^{-1}.

Although more theoretical investigation is required to understand the unique behavior at the BNNS modified Au electrode, one possible explanation is the presence of relative large O_2 adsorption sites at the edge of BNNS, as the Tafel slope of -60 mV dec^{-1} at Pt electrode in low overpotential region considered to be due to high coverage of adsorbed oxygenated intermediate species at Pt electrode [58-60]. The Tafel slopes observed at other electrodes are close to -120 mV dec^{-1}, suggesting the first charge transfer step is the rate determining step [61]. Various values for the slope ranging from -120 to over 200 mV dec^{-1} in high overpotential region have been reported [62, 63]. Very large Tafel slope at BNNS modified Au electrode in high overpotential region, -220 mV dec^{-1}, is not easy to be explained but transition from relative small Tafel slope to very large slope should be related to the slow turn over of adsorbed O_2 to the next step. Thus, the increase of active, i.e., O_2 adsorption, sites by using BNNS of much smaller dimension may increase ORR activity.

Table 1 Kinetic parameters of various electrodes for ORR obtained from the results in Fig. 9.

Electrodes	Tafel slope (mV dec^{-1})	Exchange current density (mA cm^{-2})
Bare Au	-125	6.31×10^{-8}
BNNT/Au	-130	1.99×10^{-6}
BNNS/Au	-86, -220	1.53×10^{-4}
Sputtered BN (50 s)/Au	-135	1.58×10^{-5}
Sputtered BN (100 s)/Au	-133	1.99×10^{-6}
Sputtered BN (500 s)/Au	-132	1.58×10^{-7}

3.2.5 Rotating ring disk electrode measurements (RRDE)

As discussed above, two electron reduction process taking place at BNNS modified Au electrode. RRDE measurements were carried out to quantify the resultant product which is produced by the two electron reduction process. RRDE is powerful technique, where the species produced at the disk electrode is observed by the ring electrode at a given potential. The RRDE measurements of (i) bare and (ii) BNNS modified Au electrodes with the rotation rate of 1500 rpm are shown in Figure 3.14. Au and Pt are used as a disk and ring electrodes, respectively, and the ring electrode potential was kept at +0.9 V. The formation of hydrogen peroxide could be observed in ring currents as shown in Figure 3.14 ((i)' and (ii)').

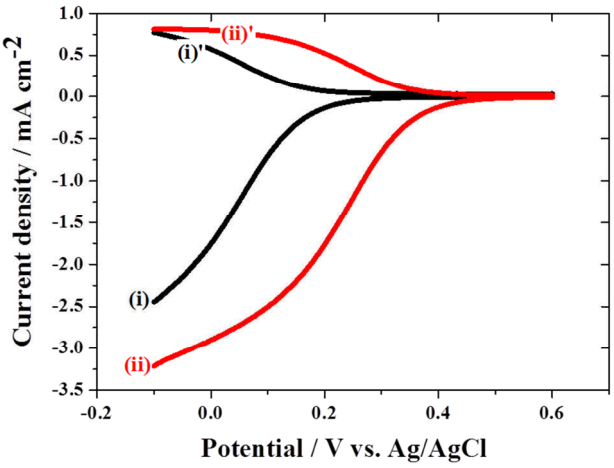

Figure: 3.14 Rotating ring disk electrode curves of (i) bare and (ii) BNNS modified Au, and corresponding ring currents are given as (i)' bare and (ii)' BNNS modified Au in O_2 saturated 0.5 M H_2SO_4 at the rotation rate of 1500 rpm. Sweep rate 10 mV sec^{-1}.

At the bare Au electrode, the ring current started to flow at +0.15 V, where the current at the disk electrode started to flow. At -0.1 V, the ring current reached a maximum and diffusion-limited behavior was observed in a more negative potential region. At the BNNS modified Au electrode, the reduction current at the disk electrode started to flow at +0.48 V and the oxidation current at the ring electrode started to flow at +0.43 V, showing higher electrocatalytic activity than that at the Au(disk) electrode. At +0.25 V, the ring current reached a maximum and diffusion-limited behavior was observed in a more negative potential region. However, the potential dependent current profiles at disk and ring electrodes indicated that the 2-electron reduction process taking place producing H_2O_2 at the BNNS

modified Au electrode as it is observed in bare Au electrode [64], which is reoxidized at the ring electrode. On bare Au, and BNNS modified Au shows the 100% collection co-efficiency [5, 65, 66] of H_2O_2 which was calculated from the equation (2.4).

$$\text{Disk: } O_2 + 2H^+ + 2e^- \rightarrow H_2O_2 \quad (3.5)$$

$$\text{Ring: } H_2O_2 \rightarrow O_2 + 2H^+ + 2e^- \quad (3.6)$$

Prof. Taketsugu also proposed the possible mechanism [45] at h-BN/Au(111) as follows. Free energy diagrams for ORR at the h-BN/Au(111) surface are obtained by accounting for entropy contribution, zero-point energy corrections, and solvent effects on the adsorption energies of O_2 and all ORR intermediates with the assumption of independent adsorption of ORR intermediates [30, 31]. Two processes, i.e., a four-electron process via OOH producing water and a two-electron process producing H_2O_2, shown below where *denotes the adsorption site are considered, and results are summarized in Fig. 3.15.

(1) Four-electron process to water:

$$O_2 + * \rightarrow O_2* \quad (3.7i)$$

$$O_2* + (H^+ + e^-) \rightarrow OOH* \quad (3.7ii)$$

$$OOH* \rightarrow O* + OH* \quad (3.7iii)$$

$$O* + (H^+ + e^-) \rightarrow OH* \quad (3.7iv)$$

$$2OH* + 2(H^+ + e^-) \rightarrow 2H_2O \quad (3.7v)$$

(2) Two-electron process to hydrogen peroxide:

$$O_2 + * \rightarrow O_2* \quad (3.8i)$$

$$O_2* + (H^+ + e^-) \rightarrow OOH* \quad (3.8ii)$$

$$OOH* + (H^+ + e^-) \rightarrow H_2O_2 \quad (3.8iii)$$

It is clear that while the dissociation of OOH* to O*and OH* leading to the four-electron process is not energetically favourable, the reduction of OOH* to H_2O_2 is possible. It must be noted that dissociation of OOH* is energetically favourable at h-BN/Ni(111) [30, 31]. Unusually strong stabilization of OOH* can be explained by the large solvent effect. The

production of H_2O_2 at BNNS/Au by the two electron reduction process is good agreement with the theoretical calculations proposed by Dr. Taketsugu for h-BN/Au(111) system [45].

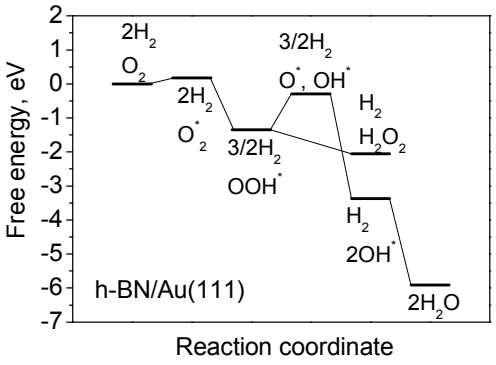

Figure: 3.15 Free energy diagram for ORR on the h-BN/Au(111).

3.2.6 Active site for ORR

3.2.6.1 AFM measurements

Now remains the question of where is the active site for ORR. The above calculations for O_2 adsorption and the free energy diagram are for the terrace of BNNS/Au, but the important role of the edge for O_2 adsorption at the N-doped carbon was suggested. To find the active sites for ORR at BNNS/Au current sensing AFM measurements have been carried out. Figure 3.16 shows (a) topography and (b) current images of BNNS on Au (111), obtained by using AFM (Agilent 5500). Although the thickness of the BNNS is about 0.9 nm (Fig. 3.16(c)), i.e., three monolayer, negligible current flowed on the BNNS [53] showing it is insulating. Thus, the terrace region of BNNS is not expected to be electrocatalytically active. It is assumed that the presence of zigzag and armchair edges (observed in Fig. 3.4(c, d)) promotes the electron transfer at the interface of gold substrate and BN nanosheets. This transferred electrons at the interface between the gold and BN nanosheets, results a strong adsorption and dissociation of oxygen [30, 31]. The adsorption of O_2 at the edge of h-BN islands of a finite size supported on the Au(111) surface was also examined theoretically [45]. As a simplest model for the h-BN island, it was considered that the hydrogen terminated 3×3 element of the h-BN layer on Au(111), which is represented by a four-layer slab containing 8×8 unit cells of Au. It is demonstrated that O_2 can readily adsorb in highly activated states at the edges of the BN island in two different configurations as shown in Fig. 3.16(d) bridging two B atoms at the BN edge and Fig. 3.16(e) bridging B and Au atoms at the perimeter

interface between the BN island and the Au(111) surface with binding energies of O_2 calculated for the B−B and B−Au bridge configurations of 0.4 and 0.2 eV, respectively, while adsorbed O_2 can exist only in a metastable configuration on defect-free BNNS monolayer on Au(111). This suggests that the edges of BNNS act as an active site for ORR. The highest ORR enhancement observed at BNNS modified Au compare to BNNT modified Au, is due to the walls of BNNT was not completely exfoliated as sheets and still exist in the nanotube structure, which is confirmed by TEM images (Fig. 3.2) and has poor contact with Au surface. In the case of BNNS, TEM images show that the highly exposed BN edges (Fig. 3.4), which has strong contact with Au surface and facilitates enhanced ORR activity compare to BNNT modified Au electrode. More detailed experimental and theoretical investigations are required to define the actual reaction site and the number of active sites. For example, a free energy diagram for ORR via edge adsorbed O_2 must be obtained and the reaction site must be detected in situ. Also, it is possible to increase the number edges by reducing the BNNS size, which possibly increase the active sites and promote the ORR as suggested by the theoretical calculations.

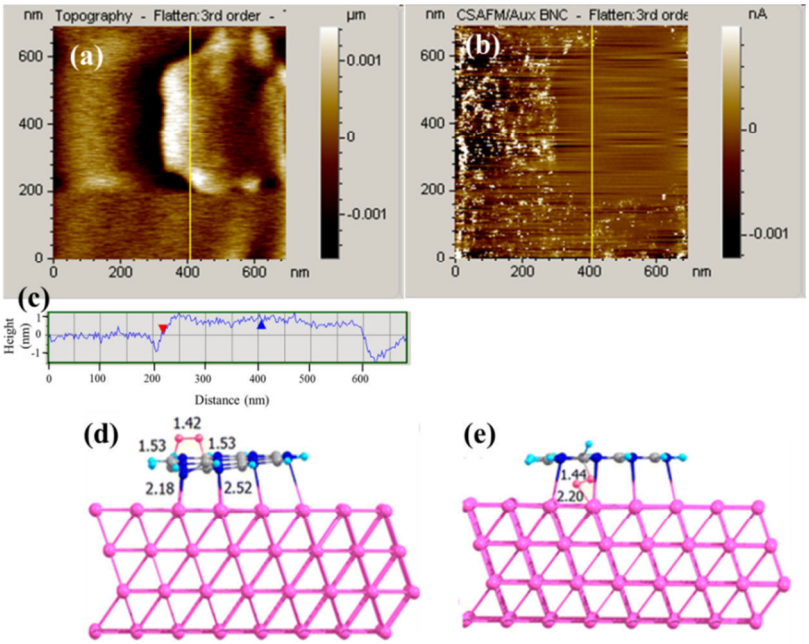

Figure: 3.16 (a) AFM topography and (b) conductance images of BNNS/Au. Bias voltage for conductance measurement was +0.4 V. (c) Cross section of topography. Optimized structures of O_2 adsorbed in (d) B–B bridge and (e) B–Au bridge configurations at the edge of the small h-BN island on the Au(111) surface. The distances are given in angstroms.

3.2.7 Effect of Substrate

Electrocatalytic activity of BNNS modified on various substrates like Au, Pt and GC were examined. Fig. 3.17 shows LSVs of (i) bare and (ii) BNNS modified Au electrodes, (iii) bare and (iv) BNNS modified Pt electrodes, and (v) bare and (vi) BNNS modified GC electrode in an O_2 saturated 0.5 M H_2SO_4 electrolyte solution at the rotation of 1500 rpm and the scan rate of 10 mV sec^{-1}. There was so no significant change observed by BNNS modification at GC electrodes ((iii), (iv)) but current-potential relation at Pt electrode shifted negatively, i.e., ORR activity was reduced by the BNNS modification ((v), (vi)), showing that BNNSs seem to block active Pt surface, which is one of the best ORR electrode [2-4]. These results confirm the importance of substrate in general and Au in particular. Theoretical study suggests that BN/Ni combination is a good candidate as an ORR electrocatalyst [30, 31] but low stability of Ni electrode in positive potential region prevents Ni to be used as a substrate. Search for more stable substrate is under way.

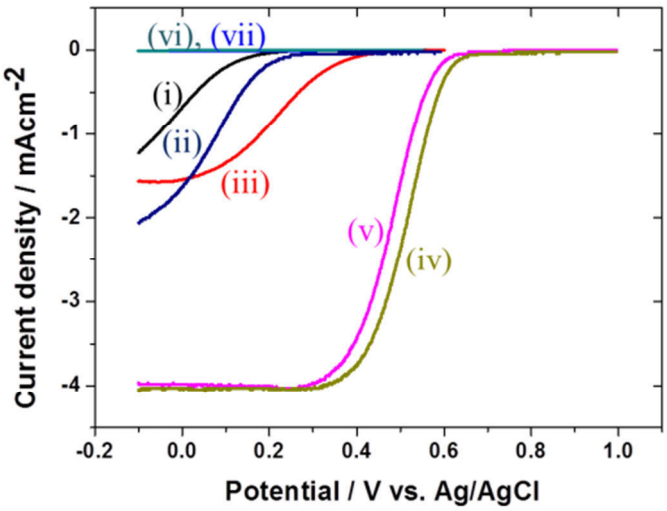

Fig. 3.17 LSVs of (i) bare, (ii) BNNT and (iii) BNNS modified Au, (iv) bare and (v) BNNS modified Pt, and (vi) bare and (vii) BNNS modified GC in O_2 saturated 0.5 M H_2SO_4 solution at the rotation rate of 1500 rpm. Scan rate: 10 mV sec^{-1}.

3.3. Conclusion

Electrocatalytic activities of various types of h-BN (BNNT, BNNS and sputter deposited BN) on gold for ORR were investigated in 0.5 M H_2SO_4 solution. All BNs acted as

ORR electrocatalyst and the overpotential for ORR at Au electrode was reduced by 0.02 to 0.27 V. The highest activity was obtained by BNNS modification and the reason for the enhanced catalytic activity of BNNS on Au was attributed to the presence of B-and/or N-edge structures. The interface between the BNNS and Au seems to play a vital role in the observed enhancement of the ORR activity due to presence of the edge structures. The number of electrons involved in ORR determined from the slope of Koutecky-Levich plot is about 2 and RRDE measurements suggest at the bare and BNNS modified Au, H_2O_2 is formed by 2-electron reduction. The kinetic parameters are determined and the difference in the Tafel slope at the BNNS decorated with Au-NCs modified Au electrode (-86 mV dec^{-1}) suggests that the ORR mechanism is differs from its on bare Au (-125 mV dec^{-1}), i.e. presence of large O_2 adsorption sites at the interface of BNNS and Au is confirmed. While the BNNS modification was very effective to improve ORR activity at Au electrode, it has no and negative effects at GC and Pt electrodes, respectively, confirming the important role of BN-Au substrate interaction for ORR activity enhancement. Although the present catalyst is not as active as Pt for ORR, the present experimental study demonstrates the possibility to functionalize inert materials to become ORR catalyst, opening new ways to design effective Pt-free catalysts for FC based on materials never before considered as catalysts.

3.4 References

(1) H. A. Gasteiger, and N. M. Markovic, *Science* 324 **(2009)**, 48.

(2) M. H. Shao, K. Sasaki, and R. R. Adzic, *J. Am. Chem. Soc.,* 128 **(2006)**, 3526.

(3) V. R. Stamenkovic, B. Fowler, B. S. Mun, G. F. Wang, P. N. Ross, C. A. Lucas, and N. M. Markovic, *Science* 315 **(2007)**, 493.

(4) E. H.Yu, K. Scott, and R. W. Reeve, *J. Electroanal. Chem.,* 547 **(2003)**, 17.

(5) N. M. Markovic, T. J. Schmidt, V. R. Stamenkovic, and P. N. Ross, *Fuel Cells* 1 **(2001)**, 105.

(6) M. Winter and R. J. Brodd, *Chem. Rev.,* 104 **(2004),** 4245.

(7) A. Kongkanand, S. Kuwabata, G. Girishkumar and P. Kamat, *Langmuir*, 22 **(2006)**, 2392.

(8) J. Zhang, K. Sasaki, E. Sutter and R. R. Adzic, *Science,* 315 **(2007),** 220.

(9) B. Lim, M. Jiang, P. H. C. Camargo, E. C. Cho, J. Tao, X. Lu,Y. Zhu and Y. Xia, *Science,* 324 **(2009),** 1302.

(10) F. Colmati, E. Antolini and E. R. Gonzalez, *J. Power Sources*, 157 **(2006)**, 98.

(11) J. Zhang, H. Yang, J. Fang and S. Zou, *Nano Lett.*, 10 **(2010)**, 638.

(12) W. Chen, J. Kim, S. Sun and S. Chen, *J. Phys. Chem. C*, 112 **(2008)**, 3891.

(13) Y. Xu, H. Wang, R. Zhu, C. Liu, X. Wu and B. Zhang, *Chem. Asian J.*, 8 **(2013),** 1120.

(14) G. Wu and P. Zelenay, *Acc. Chem. Res.*, 46 **(2013),** 1878.

(15) X. Yu and S. Ye, *J. Power Sources,* 172 **(2007),** 145.

(16) Y. Shao, J. Liu, Y. Wang and Y. Lin, *J. Mater. Chem.,* 19 **(2009),** 46.

(17) Y. J. Wang, D. P. Wilkinson and J. Zhang, *Chem. Rev.,* 111 **(2011),** 7625.

(18) B. Cao, G. M. Veith, R. E. Diaz, J. Liu, E. A. Stach, R. R. Adzic and P. G. Khalifah, *Angew. Chem., Int. Ed.,* 52 **(2013),** 10753.

(19) Y. Maekawa, A. Ishihara, J. H. Kim, S. Mitsushima and K. Ota, *Electrochem. Solid State Lett.*, 11 **(2008),** B109.

(20) G. Zhong, H. Wang, H. Yu and F. Peng, *Fuel Cells*, 13 **(2013)**, 387.

(21) R. Liu, D. Wu, X. Feng and K. Müllen, *Angew. Chem., Int. Ed.*, 49 **(2010)**, 2565.

(22) Z. S. Wu, S. Yang, Y. Sun, K. Parvez, X. Feng and K. Müllen, *J. Am. Chem. Soc.*, 134 **(2012)**, 9082.

(23) R. A. Sidik, A. B. Anderson, N. P. Subramanian, S. P. Kumaraguru and B. N. Popov, *J. Phys. Chem. B,* 110 **(2006)**, 1787.

(24) J. Ozaki, T. Anahara, N. Kimura and A. Oya, *Carbon*, 44 **(2006),** 3358.

(25) K. Gong, F. Du, Z. Xia, M. Durstock and L. Dai, *Science,* 323 **(2009),** 760.

(26) X. Hu, Y. Wu, H. Li and Z. Zhang, *J. Phys. Chem. C*, 114 **(2010),** 9603.

(27) S. Wang, E. Iyyamperumal, A. Roy, Y. Xue, D. Yu and L. Dai, *Angew. Chem.*, 123 **(2011),** 11960; *Angew. Chem., Int. Ed.,* 50 **(2011)**, 11756.

(28) D. S. Yang, D. Bhattacharjya, S. Inamdar, J. Park and J. S. Yu, *J. Am. Chem. Soc.*, 134 **(2012)**, 16127.

(29) T. Ikeda, M. Boero, S. F. Huang, K. Terakura, M. Oshima, J. Ozaki and S. Miyata, *J. Phys. Chem. C,* 114 **(2010)**, 8933.

(30) A. Lyalin, A. Nakayama, K. Uosaki and T. Taketsugu, *Phys. Chem. Chem. Phys.*, 15 **(2013)**, 2809.

(31) A. Lyalin, A. Nakayama, K. Uosaki and T. Taketsugu, *J. Phys. Chem. C*, 117 **(2013),** 21359.

(32) V. L. Solozhenko, A. G. Lazarenko, J. P. Petitet and A. V. Kanaev, *J. Phys. Chem. Solids*, 62 **(2001)**, 1331 and references therein.

(33) D. Golberg, Y. Bando, Y. Huang, T. Terao, M. Mitome, C. Tang and C. Zhi, *ACS Nano*, 4 **(2010)**, 2979.

(34) Y. Lin and J. W. Connell, *Nanoscale*, 4 **(2012)**, 6908.

(35) T. Oku, in Physical and Chemical Properties of Carbon Nanotube, ed. S. Suzuki, Intech, **(2013)**, ch. 5.

(36) Z. Liu, Y. Gong, W. Zhou, L. Ma, J. Yu, J. C. Idrobo, J. Jung, A. H. MacDonald, R. Vajtai, J. Lou and P. M. Ajayan, *Nat. Commun.*, 4 **(2013),** 2541.

(37) H. Zheng, C. Zhi, Z. Zhang, X. Wei, X. Wang, W. Guo, Y. Bando and D. Golberg, *Nano Lett.,* 10 **(2010)**, 5049.

(38) S. Azevedo, J. R. Kaschny, C. M. C. de Castilho and F. de Brito Mota, *Eur. Phys. J. B*, 67 **(2009)**, 507.

(39) L. Britnell, R. V. Gorbachev, R. Jalil, B. D. Belle, F. Schedin, M. I. Katsnelson, L. Eaves, S. V. Morozov, A. S. Mayorov, N. M. R. Peres, A. H. Castro Neto, J. Leist, A. K. Geim, L. A. Ponomarenko and K. S. Novoselov, *Nano Lett.*, 12 **(2012)**, 1707.

(40) Z. Yao, H. Nie, Z. Yang, X. Zhou, Z. Liu and S. Huang, *Chem.Commun.*, 48 **(2012)**, 1027.

(41) R. Laskowski, P. Blaha and K. Schwarz, *Phys. Rev. B*, 78 **(2008)**, 045409.

(42) M. Gao, A. Lyalin and T. Taketsugu, *Int. J. Quantum Chem.* 113 **(2013)**, 443.

(43) M. Gao, A. Lyalin and T. Taketsugu, *J. Phys. Chem. C*, 116 **(2012)**, 9054.

(44) M. Gao, A. Lyalin and T. Taketsugu, *J. Chem. Phys.,* 138 **(2013)**, 034701.

(45) K. Uosaki, G. Elumalai, H. Noguchi, T. Masuda, A. Lyalin, A. Nakayama, and T. Taketsugu, *J. Am. Chem. Soc.,* 136 **(2014)**, 6542.

(46) Z. G. Wu, and R. E. Cohen, *Phys. Rev. B* 73 **(2006)**, 235116.

(47) A. B. Preobrajenski, S. A. Krasnikov, A. S. Vinogradov, M. L Ng, T. Kaambre, A. A. Cafoolla and N. Martensson, *Phys. Rev. B* 77 **(2008)**, 085421.

(48) J. G. Diaz, Y. Ding, R. Koitz, A. P. Seitsonen, M. Iannuzzi, and J. Hutter, *J. Theor. Chem. Acc.,* 132 **(2013)**, 1350.

(49) N. Alem, R. Erni, C. Kisielowski, M. D. Rossell, W. Gannett and A. Zettl, *Phys. Rev. B*, 80 **(2009)**, 155425.

(50) R. V. Gorbachev, I. Riaz, R. R. Nair, R. Jalil, L. Britnell, B. D. Belle, E. V. Hill, K. S. Novoselov, K. Watanabe, T. Taniguchi, A. K. Geim, and P. Blake, *Small*, 7 **(2011)**, 465.

(51) P. Sutter, J. Lahiri, P. Zahl, B. Wang and E. Sutter, *Nano Lett.*, 13 **(2013)**, 276.

(52) Since BN clusters were not clearly observed in the SEM images, AFM was used to observe them using a flat Au(111) surface as the substrate.

(53) G. H. Lee, Y. J. Yu, C. Lee, C. Dean, K. L. Shepard, P. Kim, and J. Hone, *Appl. Phys.*

Lett. 99 **(2011)**, 243114.

(54) A. J. Bard and L. R. Faulkner, Electrochemical Methods: Fundamentals and Applications, Wiley, New York, 2nd edn, **(2000)**.

(55) M. Kullapere, G. Jürmann, T. T. Tenno, J. J. Paprotny, F. Mirkhalaf and K. Tammeveski, *J. Electroanal. Chem.*, 599 **(2007)**, 183.

(56) K. E. Gubbins and R. D. J. Walker, *J. Electrochem. Soc.*, 112 **(1965)**, 469.

(57) R. E. Davis, G. L. Horvath and C. W. Tobias, *Electrochim. Acta*, 12 **(1967)**, 287.

(58) N. M. Markovic, H. A. Gasteiger, B. N. Grgur and P. N. Rose, J. *Electroanal. Chem.,* 467 **(1999)**, 157.

(59) V. Stamenkovic, T. J. Schmidt, P. N. Ross and N. M. Markovic, *J. Electroanal. Chem.*, 554 **(2003),** 191.

(60) B. Liu and A. J. Bard, *J. Phys. Chem. B*, 106 **(2002)**, 12801.

(61) R. R. Adzic, S. Strbac and N. Anastasijevic, *Mater. Chem. Phys.,* 22 **(1989)**, 349.

(62) S. M. Park, S. Ho, S. Aruliah, M. F. Weber, C. A. Ward, R. D. Venter and S. Srinivasan, *J. Electrochem. Soc.,* 133 **(1986)**, 1641.

(63) Y. Kiros, *J. Electrochem. Soc.,* 143 **(1996)**, 2152.

(64) R. R. Adzic, . Strbac, and N. Anastasijevic, *Mate. Chem. Phys.* 22 **(1989)**, 349.

(65) O. Antoine, and R. Durand, *J. Appl. Electrochem.*, 30 **(2000)**, 839.

(66) V. A. Sethuraman, J. W. Weidner, A. T. Haug, S. Motupally, and L. V. Protsailo, *J. Electrochem. Soc.*, 155 **(2008)**, B50.

Chapter 4

ELECTROCATALYTIC REDUCTION OF OXYGEN ON BNNS DECORATED WITH AU-NANOCLUSTERS

4.1 Introduction

Oxygen reduction reaction (ORR) is one of the most important electrochemical reactions at present in the development of fuel cells. Metal nanoclusters (NCs) doped on carbon materials have been demonstrated as an efficient electrocatalyst for ORR [1-12]. It is well known that an Au is not a suitable electrode for ORR because the overpotential is large and the oxygen reduction in acidic solution proceeds via a 2-electron reaction pathway generating H_2O_2, while low overpotential and 4-electron reduction to H_2O are observed at Pt electrodes [13-17]. Although conventionally Au has been thought as the most inert of all metals, Au-NCs can be catalytically active, due to its small and narrow size distribution [18-23]. Interaction with the support is another factor that can dramatically influence the chemical reactivity of Au clusters [24-31]. Au clusters supported on various metal oxides, such as MgO, ZnO, TiO_2, ZrO_2, Al_2O_3, and Fe_2O_3 [32 and references therein] have been investigated experimentally. The catalytic activity of supporting material dependent Au clusters has been discussed in elsewhere [24, 26, and 32]. It was demonstrated that the interaction with the metal oxide support can modify remarkably the geometry structure and morphology of the supported cluster [33, 34] due to the charge transfer from the metal oxide support to the Au clusters [35, 36]. Thus, the charge state of the supported Au clusters can considerably influence their reactivity [37-39]. Defects in the supporting material can also be promotes the catalytic activity of metal clusters. It can trap the metal cluster and enhance charge transfer between the support and the cluster [37, 38].

Fabricating Au nanoparticles (Au-NPs) on carbon nanotube sidewalls [40] and attaching selectively Au-NPs to chemically functionalized surface sites on N-doped CNTs [41] is also a great concern for attaining Au-NP/CNT hybrids due to the interaction between the cluster and substrate as a result of charge transfer between the N-atoms and Au clusters. The high fraction of low-coordinated surface atoms decorated with on carbon materials are also described as the enhanced catalytic activity of Au-NCs on which oxygen molecules can be adsorbed [22]. It has been demonstrated that the Au atoms supported on h-BN can act as

an electrocatalyst for ORR. In metal doped h-BN due to the strong interaction between the metal atoms and defect sites in h-BN suggest, it can be stable at high temperatures compare to metal doped carbon materials [42, 43]. In this chapter, I have investigated the structural, electronic and electrocatalytic properties of BN nanosheets (BNNS) decorated with Au-NCs (Au-BNNS) in O_2 saturated 0.5 M H_2SO_4 solution.

4.2 Results and discussion

4.2.1 XRD pattern of BNNS and Au-BNNS

The XRD patterns of the BNNS and Au-BNNS are given in Figure 4.1. The resulting diffraction peaks for BN located at 2θ values of 26.6°, 41.5°, 43.8°, 50.1°, 55.2°, 59.4°, 71.4° and 75.8° are attributed to the (002), (100), (101), (102), (004), (103), (104) and (110) planes of BN, respectively [44]. The 2θ values of Au observed at 37.5°, 44.3°, 64.8° and 77.8° are attributed to the (111), (200), (220) and (311) planes of Au, respectively [45]. These peaks indicate that the structure of Au-NCs is face-centered cubic (fcc). The position of diffraction peaks for exfoliated BN and Au-NCs are identical to that of the pure h-BN and Au.

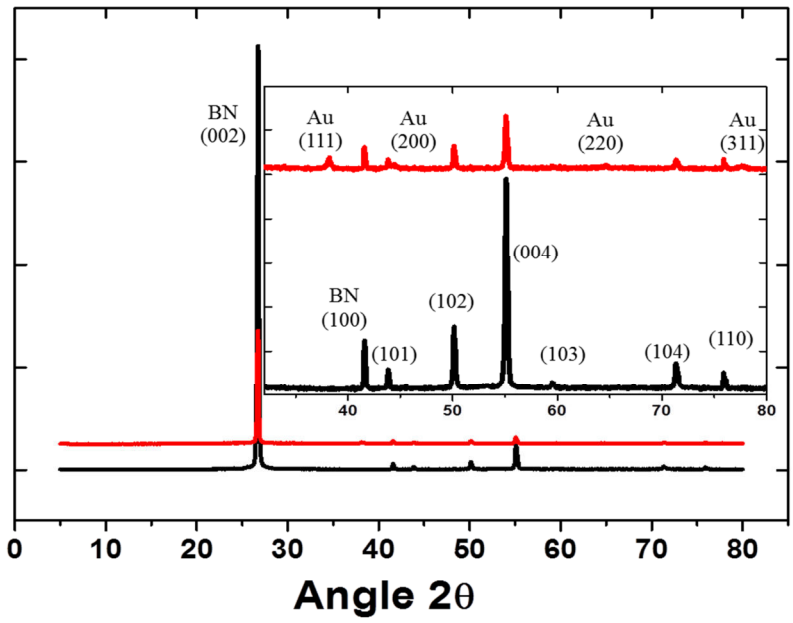

Figure: 4.1 XRD pattern of BNNS (black) and Au-BNNS (red).

The average crystallite size of Au-NCs was calculated using the Debye Scherrer formula,

$$d = K\lambda / \beta \cos(\theta) \quad (4.1)$$

where d is the crystallite size, λ is the wavelength of the X-ray radiation, K is usually taken as 0.89, 2θ is the Bragg angle of the Au(111) peak, and β is the line width at half-maximum height [45]. The average crystallite size of Au-NCs was estimated to be 28 nm.

4.2.2 TEM measurements of BNNS and Au-BNNS

TEM and HRTEM images of BNNS (top panel) and Au-BNNS (bottom panel) are shown in Figure 4.2. For TEM studies 1 µl of the BNNS and Au-BNNS dispersions were dropped onto copper mesh grid followed by solvent evaporation.

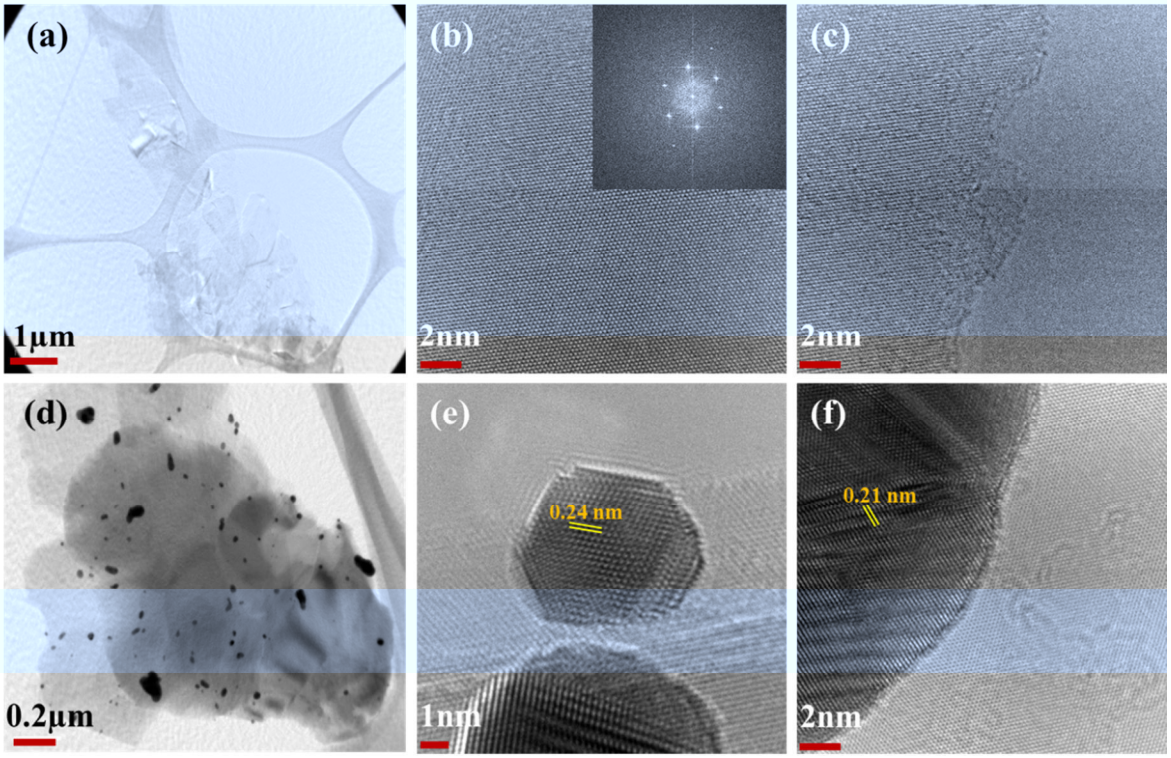

Figure: 4.2((a), (d)) TEM and ((b-c), (e-f)) HRTEM images of BNNS (top panel) and Au-BNNS (bottom panel) respectively. Inset in (b) is the FFT pattern of the image.

HRTEM images shows that BNNS are composed of single to few layers with honeycomb BN lattice. The fast Fourier transform (FFT) image also indicates that BNNS are composed of a hexagonal atomic structure as shown in inset of Figure 4.2(b). Figure

4.2(c) shows the presence of zigzag and armchair edge structures. TEM image of Au-BNNS (Figure 4.2(d)) shows that the Au-NCs are attached at the edges as well as on the surface of BN nano sheets. The size of the Au-NCs is ranging from 5 nm to 30 nm. It is good agreement with the XRD results. HRTEM (Figure 4.2(e), (f)) images show that Au-NCs are polycrystalline in nature, has the randomly oriented Au(111) and Au(200) phases with the 0.24 nm and 0.21 nm as an inter-lattice spacings, respectively. There are two possibilities for the growth of different size of Au-NCs on BNNS, (i) it is likely that the sub-5 nm Au-NCs might be formed during the dispersion of BNNS with $AuCl_4^-$ solution [46] (ii) the further growth of the Au-NCs due to the sub-5 nm Au-NCs on BNNS support which is in direct contact with BH_4^- anions during the reduction process [46]. The BNNS in the dispersion then assisted as templates for the succeeding growth of the metallic Au-NCs on their surfaces. Particularly the templating effect was more apparent for the NCs growth at the nanosheet edges, where conformal metal−BN interfaces (as shown in Figure 4.2(f)) are observed [46].

4.2.3 XPS analysis of BNNS and Au-BNNS

XP spectra of before and after the decoration of Au-NCs on BNNS were investigated by X-ray photoelectron spectroscopy (XPS) as shown in Figure 4.3. Before the decoration of Au-NCs the B 1s peak of BNNS is located at 189.7 eV and the N 1s peak is located at 397.4 eV (black lines in Figure. 4.3((a), (b)). After the decoration of Au-NCs on BNNS, significant red shifts of 0.4 eV and 0.3 eV were observed in B 1s (190.1 eV) and N 1s (397.7 eV), spectrum respectively. Furthermore, there was a 0.4 eV blue shift of XPS peak of Au-NCs (83.4 eV) observed compared with the reference Au (83.8 eV) [22, 47] as shown in Figure 4.3(c). There have been wide range of theoretical calculations demonstrated that the possibility of the interaction of metal atoms with h-BN by the mixing of dz^2 metal orbitals with the N-p_z and B-p_z orbitals of h-BN [43, 48-50]. This kind of small shift in binding energy is observed for small metal NPs, including Au, on various support materials. Those shifts are observed in higher binding energy and are generally attributed to the reduced core-hole screening in metal NPs [22, 47]. Perhaps, in this case the shift was observed in lower binding energy, suggests that there was an electron transfer between the Au-NCs and the edges of BNNS.

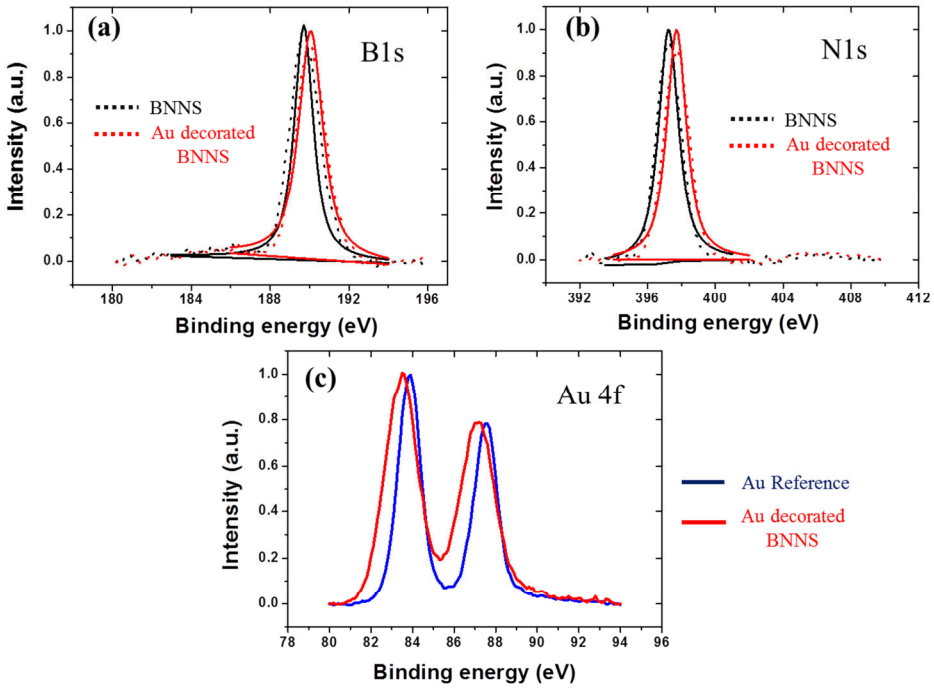

Figure: 4.3(a-c) XPS spectrum of the B1s, N1s and Au 4f region of BNNS (black line), Au-BNNS (red line), respectively. Blue line in (c) is the reference Au sample prepared by sputter deposition (thickness 150 nm).

4.2.4 Electrochemical measurements of Au-BNNS

4.2.4.1 Cyclic Voltammogram

Cyclic voltammograms (CVs) of bare, BNNS and Au-BNNS modified Au were measured in Ar saturated 0.5 M H_2SO_4; the CVs are shown in Fig. 4.4. At the bare Au electrode, in the positive going scan a large anodic current was started to be observed at around 1 V due to oxidation of Au surface (equation 4.2) and a large cathodic current was observed at around 0.95 V due to reduction of Au oxide (equation 4.3) [51]. The electric charge of the cathodic reduction of Au oxide was estimated to be 1.01 mC cm^{-2} and the standard charge for Au oxide reduction is 440 µC cm^{-2} [51], from which the electrochemical active surface area (ECSA) was estimated to be 2.29 cm^2 for bare Au electrode.

$$Au + H_2O \rightarrow AuO + 2H^+ + 2e^- \quad (4.2)$$

$$AuO + 2H^+ + 2e^- \rightarrow Au + H_2O \quad (4.3)$$

After the modification of BNNS on Au electrode surface both the Au oxide formation and the reduction currents were reduced, suggest that the oxide formation at the Au electrode was remarkably inhibited by the modification of BNNS. The electric charge for Au oxide reduction after the modification of BNNS was found to be 0.40 mC cm^{-2}. The ECSA at BNNS/Au was found to be 0.90 cm^2. From these results, it was found that 60% of the Au surface was covered by BNNS after the modification. It is good agreement with the SEM results (see fig. 3.6). In previous chapter, it was discussed that the B- and N- edge structures are important for the enhancement of ORR. In the case of Au-BNNS modification at Au electrode, large anodic and cathodic currents were observed compare to BNNS/Au. The electric charge for Au oxide reduction after the modification of Au-BNNS was found to be 0.68 mC cm^{-2}. The ECSA at Au-BNNS/Au was found to be 1.55 cm^2. Although, BNNS inhibit the oxide formation at the Au electrode, the observed large anodic and the cathodic currents are doubled compare to BNNS modified Au, its due to the oxide formation and reduction at the Au nanoclusters. Hence, it is assumed that the number of active sites also doubled at Au-BNNS/Au, due to the presence of sandwich like Au/BNNS/Au interface.

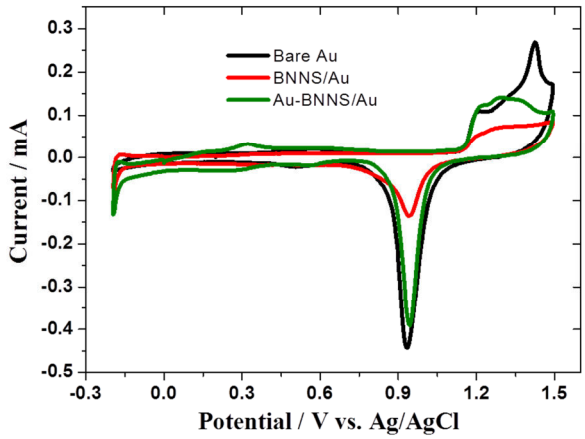

Figure: 4.4 cyclic voltammograms of (black) bare Au and (red) BNNS and (green) Au-BNNS modified Au in Ar saturated 0.5 M H_2SO_4 solution at a scan rate of 50 mV sec^{-1}.

4.2.4.2 Rotating disk and Rotating ring disk electrode measurements

RDE of Au-BNNS in O_2 saturated 0.5 M H_2SO_4 solution with a rotation rate from 0 to 2500 rpm is shown in Figure 4.5(a). The potential was scanned from +0.6 to -0.1 V at a sweep rate of 10 mV sec^{-1}. At the Au-BNNS coated Au, the cathodic current started to flow at +0.53 V (at -0.02 mA cm^{-2}). The limiting current was observed at around +0.15 V on Au-

BNNS coated Au. The Koutecky-Levich (*K-L*) plots [16, 52] at various electrode potentials are presented in Figure 4.5(b). Linear relationships were observed in all cases, the number of electron transferred was calculated to be *ca.* 2.9 to *ca.*3.1.

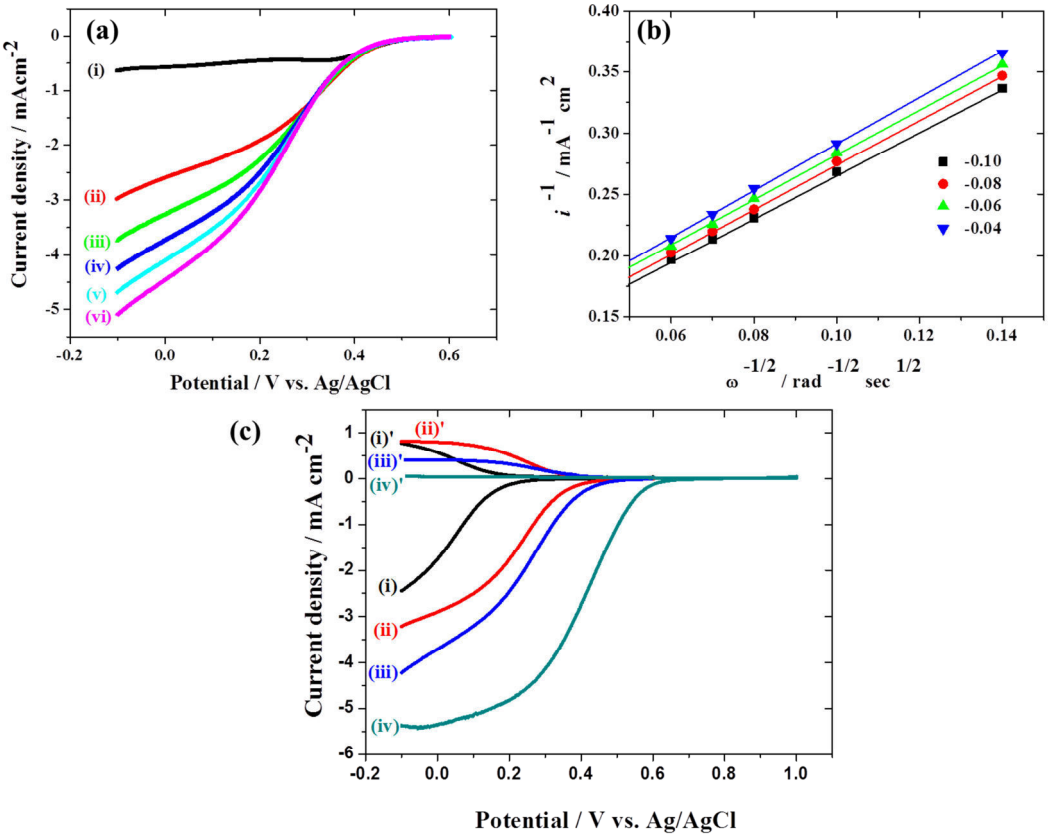

Figure: 4.5(a) Rotating disk electrode (RDE) curves of Au-BNNS in O_2 saturated 0.5 M H_2SO_4 at the rotation rate of (i) 0, (ii) 500, (iii) 1000, (iv) 1500, (v) 2000, and (vi) 2500 rpm. (b) Presents the *K-L* plots derived from the RDE measurements. (c) Rotating ring disk electrode curves of (i) bare Au, (ii) Au-BNNS/Au and (iii) Pt, and the corresponding ring currents are given as (i)' bare Au, (ii)' Au-BNNS/Au and (iii)' Pt in O_2 saturated 0.5 M H_2SO_4 at the rotation rate of 1500 rpm. Sweep rate 10 mV sec^{-1}.

RRDE measurements were carried out to estimate the produced intermediates during the ORR. For example, the production of H_2O_2 at disk electrode during ORR could be observed at ring electrode and is re-oxidized to O_2 at a given potential. The RRDE measurements of (i) bare Au, (ii) Au-BNNS coated on Au, and (iii) Pt electrodes with the rotation rate of 1500 rpm are shown in Figure 4.5(c). Au and Pt are used as disk and ring electrodes, respectively, and the ring electrode potential was kept at +0.9 V. The potentials at

which ORR current of -0.02 mA cm^{-2} flowed was 0.23, 0.53, and 0.72 V at the bare Au, Au-BNNS coated Au, and Pt electrodes, respectively. The overpotential of ORR at the Au electrode is significantly reduced by 0.3 V with the enhanced current density by the modification of Au-BNNS. Hence, it is important to estimate the reaction pathway. At the bare Au and BNNS modified Au disk electrodes, the RRDE measurements showed that the 2-electron reduction process taking place by producing H_2O_2 as discussed in chapter 3. At platinum electrode there was no significant ring current observed as has been reported [16]. At the Au-BNNS modified on Au disk electrode, the reduction current started to flow from +0.53 V and the oxidation current at Pt ring electrode started to flow at +0.48 V, showing higher electrocatalytic activity than that at the bare Au(disk) electrode. At +0.3 V, the ring current reached a maximum and diffusion-limited behavior was observed in a more negative potential region. The fraction of H_2O_2 formation was estimated form the equation (2.4) at various potetials, the potential vs. fraction of H_2O_2 formation is shown in Fig. 4.6. On bare Au and BNNS modified Au disk electrodes, fraction of H_2O_2 formation was found to be 100% [16, 53, 54] as explained in chapter 3. In the case of Au-BNNS modified on Au electrode, the fraction of H_2O_2 formation was found to be ≈55%. The enhanced current density and the reduced collection co-efficiency of H_2O_2 are clearly suggests that the partial production of H_2O_2 and H_2O are simultaneoulsy taking place at Au-BNNS modified on Au. Significant improvements are still required to decorate the well ordered uniform size metal NCs on BNNS to act as an efficient oxygen reduction electrocatalyst. The possible reactions at the disk and ring electrodes are shown in equations 4.4 to 4.8.

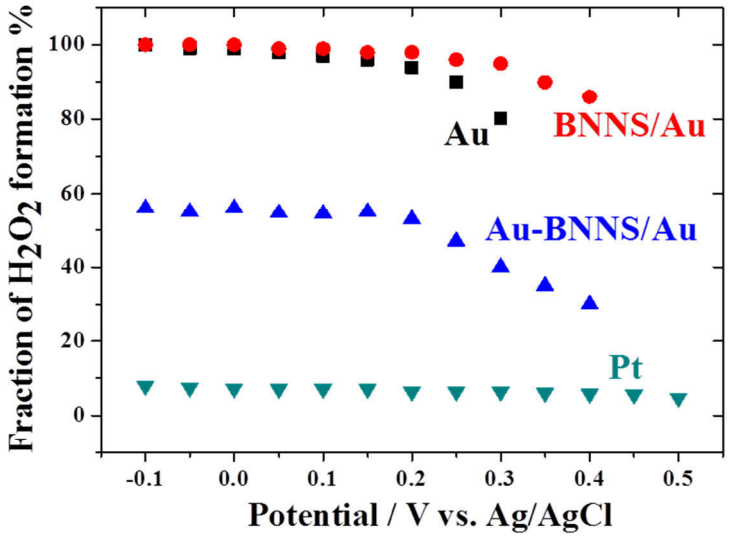

Figure: 4.6 Fraction of H_2O_2 formation, drived form the fig. 4.5 (c).

At Au and BNNS/Au

$$\text{Disk: } O_2 + 2H^+ + 2e^- \rightarrow H_2O_2 \quad (4.4)$$

$$\text{Ring: } H_2O_2 \rightarrow O_2 + 2H^+ + 2e^- \quad (4.5)$$

At Pt

$$\text{Disk: } O_2 + 4H^+ + 4e^- \rightarrow 2H_2O \quad (4.6)$$

At Au-BNNS/Au

$$\text{Disk: } O_2 + 2H^+ + 3e^- \rightarrow \text{Partial } (H_2O_2 + H_2O) \quad (4.7)$$

$$\text{Ring: (Partial) } H_2O_2 \rightarrow O_2 + 2H^+ + 2e^- \quad (4.8)$$

The observed partial production of H_2O_2 with H_2O on Au-BNNS is similar that as it observed on Au-NCs supported on other substrates as reported elsewhere [54, 55]. However, the present study demonstrates that Au-BNNS modification reduced the overpotential of Au by +0.3 V whereas is was ≈ 0.1 to 0.2 V on previouly reported Au-NCs in the literatures [55, 56] in acidic medium. XPS results suggest that the enhanced catalytic activity of BNNS decorated on Au-NCs is may be to the electron transfer between the Au-NCs and B- and/or N-edges of BNNS, that is, the interface between Au and edges of BNNS plays a crucial role for the enhanced ORR activity. BNNS decorated Au-NCs possess sandwich like Au-BNNS/Au interface, hence, there are two possiblities for the transfer of electrons, (i) at the interface between Au substrate and BNNS, (ii) at the interface between the BNNS and Au-NCs. These possibly transferred electrons can promote the sandwich like interface to act as active sites for the adsoption and dissociation of oxygen.

4.2.5 Quantitative analysis

4.2.5.1 Tafel Plots

Tafel plots obtained by plotting the values of kinetic current density (i_k) (collected from *K-L* plots) with respect to the potential (V) are shown in Figure 4.5. The Tafel slopes and exchange current densities (i_0) of bare Au, BNNS and Au-BNNS coated on Au electrodes are summarized in Table 1. The exchange current density at the Au-BNNS modified Au electrode is 4 orders of magnitude higher (2.58×10^{-4} mA cm^{-2}) than that at the bare Au electrode (6.31×10^{-8} mA cm^{-2}). The exchange current density of Au-BNNS/Au is one times higher than it at the BNNS/Au, suggest that the electron transfer rate at BNNS/Au

is faster than at the bare Au and BNNS/Au electrodes and which significantly increase the power output in the FC system. The slope at bare Au is -125 mV dec^{-1} at entire potential region, whereas, the slope at Au-BNNS modified Au electrode is -84 mV dec^{-1} at low overpotential region (> +0.2 V). The obtained slope at the high overpotential region (< +0.2 V) is -220 mV dec^{-1}. The Tafel slope of Au-BNNS modified Au electrode at low overpotential region is close to that at Pt electrode, which is approximately -60 mV dec^{-1}. Although more theoretical investigation is required to understand the unique behavior at Au-BNNS modified Au electrode, one possible explanation is the presence of relative large O_2 adsorption sites at the interface of BNNS and Au, as the Tafel slope of -60 mV dec^{-1} at Pt electrode in low overpotential region, considered to be due to high coverage of adsorbed oxygenated intermediate species at Pt electrode [57-59].

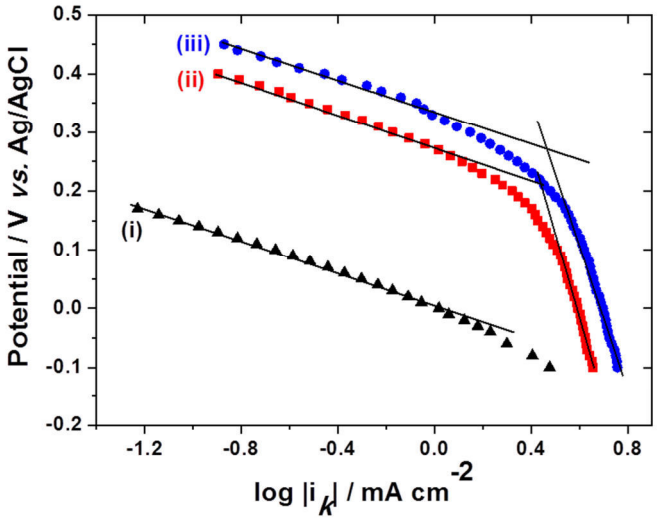

Figure: 4.7 Tafel plots of (i) bare Au, (ii) BNNS/Au, and (iii) Au-BNNS/Au electrodes in O_2 saturated 0.5 M H_2SO_4 solution derived from the intercepts of K-L plots at various potentials.

Various values for the slope ranging from -120 mV dec^{-1} to over 200 mV dec^{-1} in higher overpotential region has been reported [16, 60, 61] elsewhere. Very large Tafel slope at Au-BNNS modified Au electrode in high overpotential region, -220 mV dec^{-1}, is not easy to be explain but transition from relative small Tafel slope to very large slope should be related to the slow turn over of adsorbed O_2 to the next step [16]. These results suggest that the ORR mechanism at Au-BNNS modified Au electrode is different from those at Au

electrode, i.e., presence of large O_2 adsorption sites at the interface of BNNS and Au is confirmed.

Table: 1 Kinetic parameters of various electrodes for ORR obtained from Figure 4.5.

Electrodes	Tafel slope (mV dec^{-1})	Exchange current density (mA cm^{-2})
Bare Au	-125	6.31 X 10^{-8}
BNNS/Au	-86, -220	1.53 X 10^{-4}
Au-BNNS/Au	-84, -216	2.58X 10^{-4}

4.2.6 Effect of substrate

Electrocatalytic activity of Au-BNNS modified on Au, and GC were examined. Figure 4.6 shows RDE voltammograms of (i) bare Au, (ii) BNNS modified and (iii) Au-BNNS modified Au, (iv) bare glassy carbon (GC) and (v) Au-BNNS modified on GC electrodes in an O_2 saturated 0.5 M H_2SO_4 electrolyte solution at the rotation rate of 1500 rpm and the scan rate of 10 mV sec^{-1}.

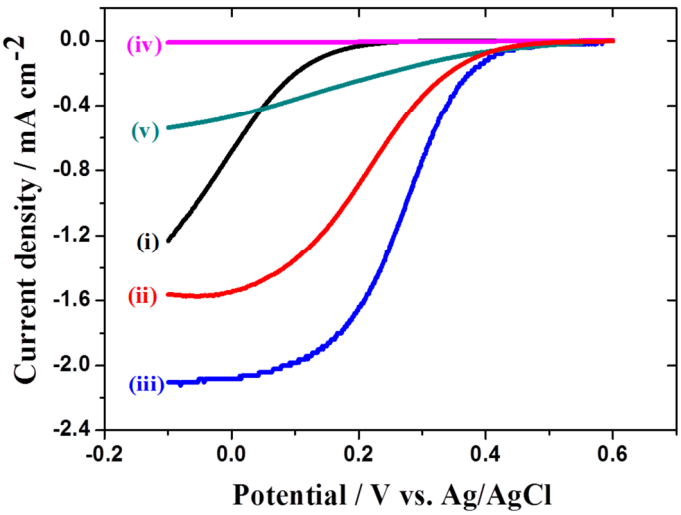

Figure: 4.8 RDE curves of (i) bare, (ii) BNNS and (iii) Au-BNNS modified Au, (iv) bare and (iv) Au-BNNS modified GC in O_2 saturated 0.5 M H_2SO_4 at the rotation rate of 1500 rpm. Scan rate 10 mV sec^{-1}.

As discussed above the ORR activity of Au (Figure 4.8(i)) was enhanced by the modification of Au-BNNS (Figure 4.8(iii)). There was no significant ORR activity observed on bare GC (Figure 4.8(iv)) in acidic solution. After the modification of Au-BNNS on GC also showed the enhanced ORR activity (Figure 4.8(v)), whereas, it was not enhanced by the modification of BNNS as demonstrated in chapter 3. These results confirm the importance of substrate in general and Au in particular.

4.3 Conclusion

Au-NCs were decorated on BNNS by reduction method. Au-BNNS modified on Au exhibits highest electrocatalytic activity. The overpotential for ORR at the Au electrode was significantly reduced by 0.3 V. XPS results suggest that the enhanced catalytic activity of Au-BNNS is may be due to the electron transfer at the interface between Au and neighbouring B- and/or N-edge atoms in BNNS. The number of electrons involved in ORR determined from the slope of *K-L* plot is about 3 and RRDE measurements suggest the partial production of H_2O_2 by 2-electron reduction process and H_2O by 4-electron reduction process. This is in contrast to the results obtained at the bare and BNNS modified Au, where only H_2O_2 is formed by 2-electron reduction. Electrocatalytic activity for ORR is enhanced even at the GC electrode when it is modified by Au-BNNS, confirming the importance of Au-BN interaction for the enhancement of electrocatalytic activity. The kinetic parameters are determined and the difference in the Tafel slope at the Au-BNNS modified Au electrode (-84 mV dec^{-1}) suggests that the ORR mechanism is differs from its on bare Au (-125 mV dec^{-1}), i.e., presence of large O_2 adsorption sites at the interface of BNNS and Au is confirmed. Significant improvements are still required to decorate the well-ordered uniform size metal NCs on BNNS to act as an efficient oxygen reduction electrocatalyst.

4.4 References

(1) C. Zhu, and S. Dong, *Nanoscale*, 5 **(2013)**, 1753.

(2) X. Fan, W.T. Zhenga, and J.-L. Kuo, *RSC Adv.*, 3 **(2013)**, 5498.

(3) S.-S. Kim, Y.-R. Kim, T. D. Ching, and B.-H. Sohn, *Adv. Funct. Mater.*, **(2014)**, DOI: 10.1002/adfm.201303968.

(4) T. Zhang, Q. Xue, M. Shan, Z. Jiao, X. Zhou, C. Ling, and Z. Yan, *J. Phys. Chem. C,*

116 **(2012)**, 19918.

(5) Y. Lu, and W. Chen, *Chem. Soc. Rev.,* 41 **(2012)**, 3594.

(6) P. V. Kamat, *J. Phys. Chem. Lett.*, 1 **(2010)**, 520.

(7) D. Wu, F. Zhang, P. Liu, and X. Feng, *Chem.-Eur. J.*, 17 **(2011)**, 10804.

(8) M. Zhou, A. Zhang, Z. Dai, P. Feng, and C. Zhang, *J. Phys. Chem. C,* 114 **(2010)**, 16541.

(9) D.-H. Lim, and J. Wilcox, *J. Phys. Chem. C,* 115 **(2011)**, 22742.

(10) D.-H. Lim, and J. Wilcox, *J. Phys. Chem. C,* 116 **(2012)**, 3653.

(11) X. Chen, G. Wu, J. Chen, X. Chen, Z. Xie, and X. Wang, *J. Am. Chem. Soc.*, 133 **(2011),** 3693.

(12) K. S. Subrahmanyam, A. K. Manna, S. K. Pati, and C. N. R. Rao, *Chem. Phys. Lett.*, 497 **(2010)**, 70.

(13) M. H. Shao, K. Sasaki, and R. R. Adzic, *J. Am. Chem. Soc.,* 128 **(2006)**, 3526.

(14) V. R. Stamenkovic, B. Fowler, B. S. Mun, G. F. Wang, P. N. Ross, C. A. Lucas, and N.M. Markovic, *Science,* 315 **(2007)**, 49.

(15) E. H.Yu, K. Scott, and R. W. Reeve, *J. Electroanal. Chem.,* 547 **(2003)**, 17.

(16) N. M. Markovic, T. J. Schmidt, V. R. Stamenkovic, and P. N. Ross, *Fuel Cells,* 1 **(2001)**, 105.

(17) M. Winter and R. J. Brodd, *Chem. Rev.,* 104 **(2004),** 4245.

(18) W. Chen, and S. Chen, *Angew. Chem. Int. Ed.*, 48 **(2009)**, 4386.

(19) Y. Lee, A. Loew, and S. Sun, *Chem. Mater.*, 22 **(2010)**, 755.

(20) W. Tang, H. Lin, A. Kleiman-Shwarsctein, G. D. Stucky, and E. W. McFarland, *J. Phys. Chem. C,* 112 **(2008)**, 10515.

(21) R. Pal, L. Wang, Y. Pei, L. Wang, and X. C. Zheng, *J. Am. Chem. Soc.*, 134 **(2012)**, 9438.

(22) H. Yin, H. Tang, D. Wang, Y. Gao, and Z. Tang, *ACS Nano*, 6 **(2012)**, 8288.

(23) N. Alexeyeva, T. Laaksonen, K. Kontturi, F. Mirkhalaf, D. J. Schiffrin, and K. Tammeveski, *Electrochem. Commun.,* 8 **(2006)** 1475.

(24) M. Haruta, *Catal. Today* 36 **(1997)**, 153.

(25) R. Coquet, K. L. Howard, and D. J. Willock, *Chem. Soc. Rev.,* 37 **(2008)**, 2046.

(26) M. Okumura, S. Tsubota, and M. Haruta, *J. Mol. Catal. A: Chem.,* 199 **(2003)**, 73.

(27) U. Landman, B. Yoon, C. Zhang, U. Heiz, and M. Arenz, *Top. Catal.,* 44 **(2007)**, 145.

(28) C. Harding, V. Habibpour, S. Kunz, A. N.-S. Farnbacher, U. Heiz, B.Yoon, and U. Landman, *J. Am. Chem. Soc.,* 131 **(2009)**, 538.

(29) J. A. Rodríguez, L. Feria, T. Jirsak, Y. Takahashi, K. Nakamura, and F. Illas, *J. Am. Chem. Soc.,* 132 **(2010)**, 3177.

(30) M. Haruta, *Faraday Discuss.,* 152 **(2011)**, 11.

(31) K. L. Howard, and D. J. Willock, *Faraday Discuss.,* 152 **(2011)**, 135.

(32) M. Haruta, *Chem. Rec.,* 3 **(2003)**, 75.

(33) V. V. Semenikhina, A. Lyalin, A. V. Solov'yov, and W. Greiner, *JETP,* 106 **(2008)**, 678.

(34) V. V. Dick, I. A. Solov'yov, and A. V. Solov'yov, *Phys. Rev. B,* 84 **(2011)**, 115408.

(35) B. Yoon, H. Häkkinen, U. Landman, A. S. Wörz, J.-M. Antonietti, S. Abbet, K. Judai, and U. Heiz, *Science,* 307 **(2005)**, 403.

(36) M. Chen, Y. Cai, Z. Yan, and D. W. Goodman, *J. Am. Chem. Soc.,* 128 **(2006)**, 6341.

(37) M. Gao, A. Lyalin and T. Taketsugu, *J. Phys. Chem. C,* 116 **(2011)**, 9054.

(38) A. Lyalin, and T. Taketsugu, *J. Phys. Chem. Lett.,* 1 **(2010)**, 1752.

(39) C. Bürgel, N. M. Reilly, G. E. Johnson, R. Mitrićc, M. L. Kimble, A. W. Castleman, and V. Bonačcić -Koutecký, *J. Am. Chem. Soc.,* 130 **(2008)**, 1694.

(40) H. C. Choi, M. Shim, S. Bangsaruntip, and H. Dai, *J. Am. Chem. Soc.,* 124 **(2002)**, 9058.

(41) H. Y. Koo, H.-J. Lee, Y.-Y. Noh, E.-S. Lee, Y.-H. Kim, and W.-S. Choi, *J. Mater. Chem.,* 22 **(2012)**, 7130.

(42) S. Lin, X. Ye, R. S. Johnson, and H. Guo, *J. Phys. Chem. C*, 117 **(2013)**, 9054.

(43) H. P. Koch, R. Laskowski, P. Blaha, and K. Schwarz, *Phys. Rev. B,* 86 **(2012)**, 155404.

(44) R. T. Paine, and C. K. Narula, *Chem. Rev.*, 90 **(1990)**, 73.

(45) L. D. Zhu, T.S. Zhao, J.B. Xu, and Z.X. Liang, *J. Power Sources*, 187 **(2009)**, 80.

(46) Y. Lin, C. E. Bunker, K. A. S. Fernando, and J. W. Connell, *ACS Appl. Mater. Interfaces,* 4 **(2012)**, 1110.

(47) M. Turner, V. B. Golovko, O. P. H. Vaughan, P. Abdulkin, A. B. Murcia, M. S. Tikhov, B. F. G. Johnson and R. M. Lambert, *Nature,* 454 **(2008)**, 981.

(48) A. Lyalin, A. Nakayama, K. Uosaki and T. Taketsugu, *Phys. Chem. Chem. Phys.*, 15 **(2013)**, 2809.

(49) A. Lyalin, A. Nakayama, K. Uosaki and T. Taketsugu, *J. Phys. Chem. C*, 117 **(2013),** 21359.

(50) M. Gao, A. Lyalin and T. Taketsugu, *J. Chem. Phys.,* 138 **(2013)**, 034701.

(51) H. A. Kozlowska and B. E. Conway, *Electrochim. Acta*, 31 **(1986)**, 1051.

(52) A. J. Bard and L. R. Faulkner, Electrochemical Methods: Fundamentals and

Applications, Wiley, New York, 2nd edn, **(2000)**.

(53) O. Antoine, and R. Durand, *J. Appl. Electrochem.*, 30 **(2000)**, 839.

(54) V. A. Sethuraman, J. W. Weidner, A. T. Haug, S. Motupally, and L. V. Protsailo, *J. Electrochem. Soc.*, 155 **(2008)**, B50.

(55) T. Inasaki, and S. Kobayashi, *Electrochim. Acta,* 54 **(2009)**, 4983.

(56) I. Yagi, T. Ishida, and K. Uosaki, *Electrochem. Commun.,* 6 **(2004)**, 773.

(57) N. M. Markovic, H. A. Gasteiger, B. N. Grgur and P. N. Rose, *J. Electroanal. Chem.*, 467 **(1999)**, 157.

(58) V. Stamenkovic, T. J. Schmidt, P. N. Ross and N. M. Markovic, *J. Electroanal. Chem*., 554 **(2003)**, 191.

(59) B. Liu and A. J. Bard, *J. Phys. Chem. B*, 106 **(2002)**, 12801.

(60) S. M. Park, S. Ho, S. Aruliah, M. F. Weber, C. A. Ward, R. D. Venter and S. Srinivasan, *J. Electrochem. Soc.*, 133 **(1986)**, 1641.

(61) Y. Kiros, *J. Electrochem. Soc.*, 143 **(1996)**, 2152.

Chapter 5

BNNS AND BNNS DECORATED WITH METAL NANOCLUSTERS ON METAL SUBSTRATES AS EFFICIENT HYDROGEN EVOLUTION CATALYSTS

5.1 Introduction

Hydrogen is the cleanest fuel and represents one of the most promising energy sources. The findings of the efficient electrocatalysts to reduce the overpotential of the hydrogen evolution reaction (HER) is essentially important for a variety of electrochemical processes, fuel cells, and solar H_2 production (water splitting) as well as being earth abundant and inexpensive [1-6]. Although Pt have high efficiency in the HER, their scarcity and high cost inhibit large scale applications [1-5]. Nevertheless, due to its high cast, limited resources, and growing consumption in the automobile industry restricts its usage in a large scale commercial development. Discovery of noble metal free electrocatalyst is the foremost task in front of the development and implementation of HER catalyst. It has been found that the first-row transition metals are very efficient owing to their stability, abundance in nature, and low cost to address this challenge. Various types of Ni alloys ought to be demonstrated as an alternative for Pt due to their low cost, high abundance, low overpotential, and stability in alkaline electrolyzers [7-12]. Recently, inorganic catalysts such as nanometer scaled XS_2 (MoS_2 and WS_2) have drawn great attention due to their low cost, high chemical stability, and promising photocatalytic and electrocatalytic properties in HERs [13-25]. Much of the experimental work has been developed from the theoretical calculations, which suggested that the metallic edges of 2H XS_2 crystals are electrocatalytically active. This has led to investigations of XS_2 nanoparticles or complexes with a high concentration of exposed edges as electrocatalyst for hydrogen evolution. Hinnemannet al. reported that the hydrogen binding energy (HBE) of MoS_2 is located near the noble metal group on the volcano plot [22] and this was subsequently verified by experimental results.

Hexagonal boron nitride (h-BN) monolayer has geometric structure similar to the graphene, although BN is an insulator with a wide band gap (˜5.8eV), the band gap in h-BN monolayer can be considerably reduced if some defects are introduced or it is placed on metal substrates [26-32]. It was demonstrated that the atomically thin h-BN nanoribbons will

become semiconducting due to conducting (N-) edge structure and vacancy defects [33, 34] similar like XS_2 crystals [15-19]. Theoretical calculations confirm that the electronic properties of h-BN monolayer supported 3d, 4d, and 5d transition metal surfaces can be strongly modified as a result of mixing of the dz^2 metal orbital with N-p_z and B-p_z orbitals of the h-BN monolayer [26, 27]. This rearrangement was strongly influenced oxygen reduction reaction (ORR) in previously reported [26, 27, 35-38] studies; it was demonstrated in Chapter 3 and 4. Additionally, it has been demonstrated theoretically that BN can also act as an electrocatalyst for CO oxidation [39] and CO_2 capture [40]. There are wide ranges of theoretical and experimental studies have been reported in elsewhere claiming that the BN can adsorb hydrogen better than carbon nanotubes (CNTs) [41-47]. Because, it has the ionic character of B-N bond, which may induce an extra dipole moment and hence hydrogen strongly adsorbs on BN. In fact, this feature may applicable for all ionic materials because the induced dipole moment of hydrogen is sensitive to local electric field [44-46]. The adsorption of hydrogen on BN is a chemisorption process [45]. Also, it have been reported that the doping of transition metals with BN can enhance the hydrogen uptake capacity [47, 48].

In this chapter I will report the electrocatalytic evolution of hydrogen on BNNS, and BNNS decorated with Au- and Ni-nanoclusters (Au-BNNS and Ni-BNNS) modified on various substrates like Au, Pt and glassy carbon (GC). I will also report the hydrogen oxidation reaction (HOR) behavior.

5.2 Results and discussion

5.2.1 TEM measurements of Ni-BNNS

The characterization (SEM, XRD, TEM and XPS measurements) of BNNS and Au-BNNS has been discussed in Chapter 3 and Chapter 4. In this section I will discuss the characterization of Ni-BNNS. For TEM studies 1 µl of the Ni-BNNS dispersion was dropped onto copper mesh grid followed by solvent evaporation. TEM and HRTEM images of Ni-BNNS are shown in Figure 5.1. TEM image of Ni-BNNS (Figure 5.1(a)) shows that the Ni-NCs are attached both on the edges and traces of BNNS and it was decorated by spherical shaped Ni-NCs with the diameter ranging from 5 to 100 nm. HRTEM (Figure 5.1(b), (c)) images show that Ni-NCs are amorphous in nature and surrounded by oxide layer of 3 to 5 nm, has the randomly oriented Au (111) phase with the 0.24 nm as an inter-lattice spacing.

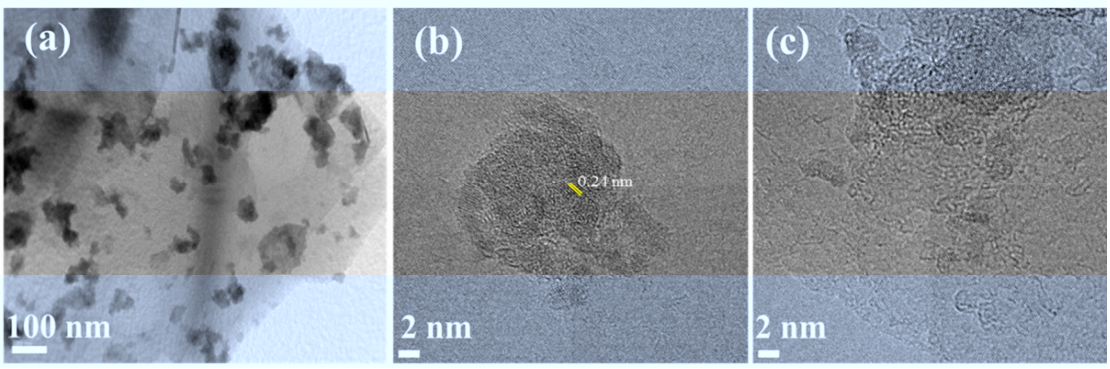

Figure: 5.1 (a) TEM and (b-c) HRTEM images of Ni-BNNS.

5.2.2 XPS analysis of Ni-BNNS

XP spectra of BNNS, Ni-BNNS and reference Ni are shown in Figure 5.2. The Ni 2p spectrum of Ni-BNNS is shown in Figure 5.2(a). It has the Ni $2p_{3/2}$ XPS peaks at the binding energies of 854.7, 855.8, and 857.2 eV and the Ni $2p_{1/2}$ peaks at the binding energies of 872.7, 873.8 and 875.1 eV. As a reference Ni substrate was prepared by sputter deposition. The Ni $2p_{3/2}$ XPS peaks for the reference sample (Figure 5.2(b)) observed at the binding energies of 852.7, 853.8, 855.6, and 857.3 eV and the Ni $2p_{1/2}$ peaks at the binding energies of 870.2, 871.4, 873.4 and 875.2 eV, which are corresponds to Ni^0, NiO, $Ni(OH)_2$, and NiOOH, respectively [55, 56]. Hence, the observed Ni 2p peaks for Ni-BNNS are assigned to be NiO, $Ni(OH)_2$, and NiOOH, respectively. It is evident that the HRTEM images showed the presence of metallic fringes covered by oxide layer. In general, the Ni $2p_{3/2}$ spectrum shows a complex structure with an intense satellite signals (between 860 eV to 865 eV) of high binding energy adjacent to the main peaks (located between 850 eV to 860 eV), which can be attributed to multi electron excitation [57-64]. NiO peak of Ni-NCs decorated on BNNS is red shifted of 0.9 eV. Before the decoration of Ni-NCs the B 1s peak of BNNS is located at 189.7 eV and the N 1s peak is located at 397.4 eV (black line Figure 5.2 (c), (d)). After the decoration of Ni-NCs on BNNS, B 1s peak (189.4 eV) and N 1s (397.3 eV) peaks are blue shifted at of 0.3 eV and 0.1 eV, respectively. These binding energy shifts clearly suggests that the electrons are transferring at the interface between the Ni-NCs and the neighboring B- and/or N- edges of BNNS. A broad peak observed between 188 eV to 182 eV is attributed to the presence of Ni boride (Ni_2B) [67-69]. It might be formed during the reduction reaction of Ni^{2+} ions with borohydride in aqueous solution under anaerobic conditions [67].

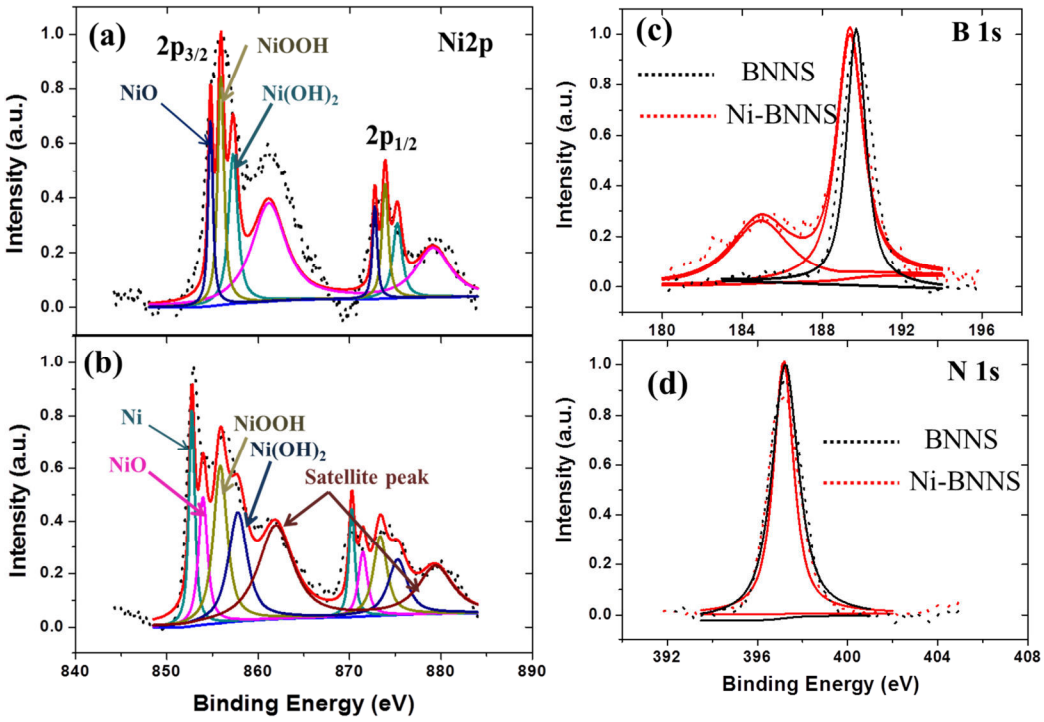

Figure: 5.2(a, b) XPS spectrum of the Ni 2p, (c) B 1s, and (d) N 1s of Ni-BNNS. (b) is the reference sample of Ni prepared by sputter deposition (thickness 150 nm).

5.2.3 Electrochemical hydrogen evolution reaction

5.2.3.1 HER measurements of BNNS and Au (or) Ni-BNNS on Au, Pt and GC electrodes

The electrocatalytic HER activities of BNNS, and Au or Ni-BNNS deposited on Au, Pt and GC electrodes were investigated in Ar saturated 0.5 M H_2SO_4 solution using a typical three-electrode setup (see the experimental section for more experimental details). The (i-v) polarization curves of HER are shown in Figure 5.3. As a reference, the measurements also performed using a sputter deposited Au and Pt, and commercial GC, in which Pt (Figure 5.3((a)((i))) exhibiting high HER catalytic performance, Au (Figure 5.3((a)((v))) and GC (Figure 5.3((c)((iv))) exhibiting comparatively poor performance (with a 200 and 700 mV of overpotential, respectively).

At the Au electrode, the polarization curve recorded for Au-BNNS modified electrode showed a small overpotential of ~70 mV for the HER (Figure 5.3((a)((ii))), whereas, BNNS (Figure 5.3((a)((iii))) and Ni-BNNS (Figure 5.3((a)((iv))) modified electrodes showed a overpotential of ~90 mV and ~140 mV for the HER, respectively, beyond which the cathodic current flow rapidly under more negative potentials.

At the Pt electrode, the polarization curve recorded for BNNS (Figure 5.3((b)((iv))) showed overpotential of ~30 mV for the HER, whereas, it's for Au or Ni-BNNS showed a near overpotential zero for the HER (Figure 5.3((b)((ii), (iii))), beyond which the cathodic current flow rapidly under more negative potentials.

At the GC electrode, BNNS (Figure 5.3((c)((v))) and Ni-BNNS (Figure 5.3((c)((vi))) modified on GC showed large overpotential ~600 mV and 500 mV respectively, for the HER. The polarization curve recorded for Au-BNNS (Figure 5.3((c)((vii))) on GC electrodes showed the overpotential of ~80 mV for HER but beyond which the cathodic current starts to flow slowly up to the overpotential of ~250 mV after that the cathodic current flows rapidly under more negative potentials.

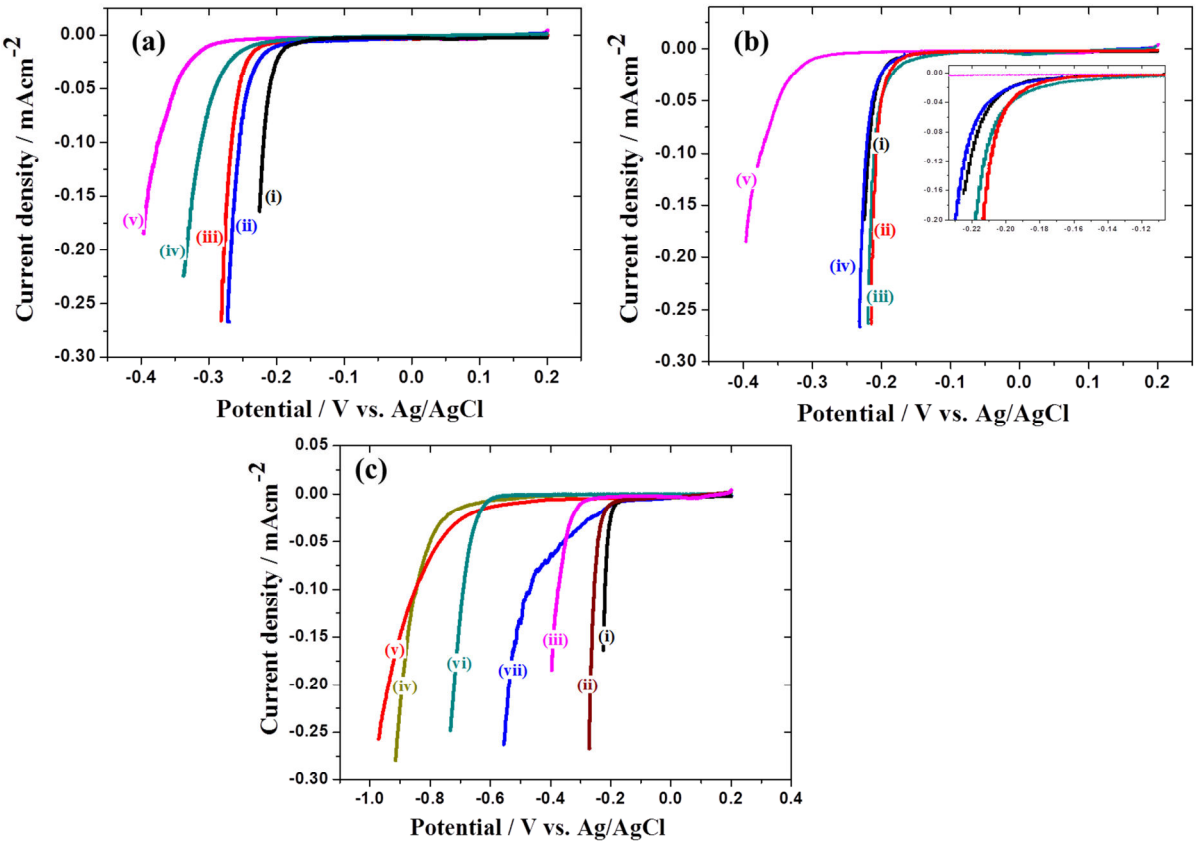

Figure: 5.3(a) Au substrate: HER polarization curves of (i) Pt, (ii) Au-BNNS/Au, (iii) BNNS/Au (iv) Ni-BNNS/Au, and (v) bare Au. (b) Pt substrate: HER polarization curves of (i) Pt, (ii) Au-BNNS/Pt (iii) Ni-BNNS/Pt, (iv) BNNS/Pt, and (v) Au. (c) GC substrate: HER polarization curves of (i) Pt, (ii) Au-BNNS/Au, (iii) bare Au (iv) bare GC, (v) BNNS/GC, (vi) Ni-BNNS/GC, and (vii) Au-BNNS/GC in Ar saturated 0.5 M H_2SO_4. Scan rate 0.1 mV Sec^{-1}.

From the above results, In the case of BNNS modification, the significant enhancement of HER was observed at Au electrode. Perhaps, no such enhancement was observed at GC and it was reduced at Pt electrodes. It suggests that the BNNS is blocking the Pt surface and it's inert on the GC substrate in acidic medium. It is good agreement with the results obtained for ORR, i.e., ORR activity of Pt electrode was reduced and it was not enhanced at GC electrode after the modification of BNNS. Although, BN has the potential to adsorb the hydrogen due to its ionic nature of B-N bond, it was also reported that the transition metal functionalization can enhance hydrogen adsorption. According to Mulliken analysis, Ti atom donates 0.78 electrons to single wall BN tubes [48]. In the case of BNNS modified Au, it is expected similar kind of electron transfer at the interface of BNNS and Au, the possibly transferred electrons at the interface and facilitate the HER.

In the case of Au-BNNS modification, the HER activity of Au, GC and Pt electrodes are all enhanced. Modification by Ni-BNNS also showed enhanced HER activity but much less than by the Au-BNNS modification because oxide layer is formed over the Ni metallic fringes, which is confirmed by XPS. XPS results also confirm that there is electron transfer between Au- (or) Ni-NCs and edges of BNNS.

In the case of Au-BNNS modification on GC, the cathodic current flows slowly in the less overpotential region and its flow rapidly in the higher overpotential region are due to the effect of substrate. If the Au-BNNS placed on GC substrate there is only one possibility to enhance the HER, that is, the electron transfer occurs between the Au-NCs and the edges of BNNS, whereas there is no significant interface effect between the BNNS and GC substrate, that is the reason why, although the hydrogen starts to evolve at very less overpotential there was no significant flow of cathodic current at its less overpotential region. Similar behavior was also observed for Ni-BNNS modified on GC electrode. These results strongly suggest that the crucial role of substrate to functionalize the traditionally inert material, BN to become electrocatalytically active. These results also confirm that Au-BN interaction plays a crucial role in the flow of HER cathodic current.

As discussed in chapter 3 and 4, it was suggested that the active for ORR might be the interface between the Au electrode and B- and/or N-edge structures. It is also suggested that the active site for HER might be the same because the transition metal doped BN strongly binds the hydrogen atoms than that of on bare BN surface, and the adsorbed hydrogen atoms can be easily desorbed as H_2 molecules during the catalysis. Although hydrogen adsorbs on BN surface due to its ionic character, for catalysis there must be an electron transport between the conducting electrode surface and BN surface. Current sensing AFM suggest that

there is no current flow on the BN surface. Hence, it's clearly suggesting that the Au and BN interface plays crucial role for also HER.

5.2.4 Quantitative analysis

5.2.4.1 Tafel plots

The relation between the potential and logarithmic kinetic current gives Tafel plot, reflecting rate determining step (*rds*) of the reaction and the adsorption model of intermediates, which is very important for discussing the mechanism of electrochemical reactions. The linear portions of the Tafel plots (Figure 5.4) were fit to the Tafel equation

$$\eta = b \log j + a,$$

where j is the current density, b is the Tafel slope and a is Tafel constant, yielding Tafel slopes of ~30, ~75, ~27, ~27, ~28, ~40, ~44, and ~71 mV dec^{-1} for Pt, Au, BNNS/Pt, Au-BNNS/Pt, Ni-BNNS/Pt, BNNS/Au, Au-BNNS/Au and Ni-BNNS/Au, respectively. Three possible reaction steps have been suggested for the HER in acidic media [2-5].

First is a primary discharge step (Volmer reaction),

$$H_3O^+ + e^- \rightarrow H_{ads} + H_2O \qquad (\approx 120 \text{ mV dec}^{-1}) \qquad (5.1)$$

This step is followed by either an electrochemical desorption step (Heyrovsky reaction),

$$H_{ads} + H_3O^+ + e^- \rightarrow H_2 + H_2O \qquad (\approx 40 \text{ mV dec}^{-1}) \qquad (5.2)$$

or a recombination step (Tafel reaction),

$$H_{ads} + H_{ads} \rightarrow H_2 \qquad (\approx 30 \text{ mV dec}^{-1}) \qquad (5.3)$$

The slopes of the above proposed reaction steps have been derived [20, 70, and 71]as follows.

The slope for discharge step was derived to be

$$b = 2.3\, RT/\alpha F \qquad (5.4)$$

The slope for electrochemical desorption step was derived to be

$$b = 2.3\, RT/(1+\alpha)\, F \qquad (5.5)$$

The slope for recombination step was derived to be

$$b = 2.3\ RT/\ 2F \qquad (5.6)$$

Where, i = ORR current density, i_o = exchange current density, α = the transfer coefficient, η= the overpotential of ORR, F = the Faraday constant, R = the gas constant, and T = the temperature in K.

The determination and interpretation of the Tafel slope are important for interpretation of the elementary steps involved. Having a very high H_{ads} coverage ($\theta_H \approx 1$), the HER on a Pt surface is known to proceed through the Volmer Tafel mechanism (eqs 5.1 and 5.3), and the recombination step is the rate-limiting step at low overpotentials, as attested by the measured Tafel slope of 30 mV dec^{-1} and an exchange current density of 4.5 x 10^{-4}[2, 5]. Whereas, the Tafel slope and the exchange current density for the recently developed catalyst such as MoS_2, WS_2 and Ni_2P have been demonstrated as 41, 33 and 46 mV dec^{-1} and 8.0 x 10^{-6}, 2.0 x 10^{-5} and 3.3 x 10^{-5} A cm^{-2} respectively.

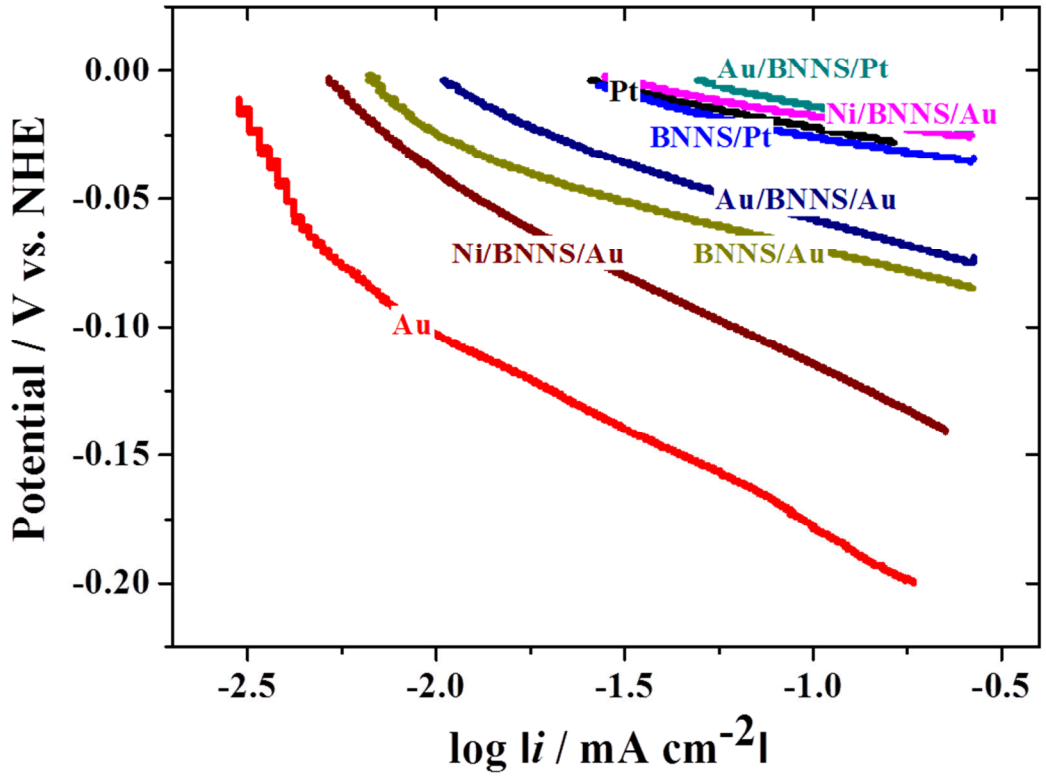

Figure: 5.4 Tafel plots obtained from the HER polarization curves (Figure 5.3).

Unfortunately, the reaction mechanism on BNNS has been not studied. However, the observed Tafel slope of ~44 and ~40 mV dec^{-1} and the exchange current density of 1.6 x 10^{-6} and 4.8 x 10^{-6} A cm^{-2} respectively, in the present study. The Tafel slopes and exchange current densities obtained for the present and reported catalysts are given in table. 5.1. The Tafel slope measured to date for a BNNS and Au-BNNS catalyst is close to the values reported for MoS_2 and Ni_2P. These results suggesting that the electrochemical desorption is the rate limiting step and thus that the Volmer Heyrovsky HER mechanism (eqs 5.1 and 5.2) could be operative in the HER.

Among the above said catalyst Au-BNNS showed the high performance in the HER, is may be due to the transfer of electron between the BNNS sheets and Au (see XPS results in chapter 4). The high dispersion of Au-NCs on BNNS, which has an abundance of accessible edges (see TEM results in chapter 4) that could serve as active catalytic sites for the HER. At the interface between the interconnected network of Au-NCs and BNNS may offered a rapid electron transport, due which the electrons are possibly accumulated at the interface, facilitates the high catalytic performance.

Table: 5.1 Kinetic parameters of various electrodes for HER obtained from the results in Figure 5.4.

Electrodes	**Tafel slope (mV/decade)**	**Exchange current density (A cm^{-2})**	**Ref**
Pt	30	2.0 x 10^{-5}	Present
Au	75	3.1 x 10^{-7}	Present
BNNS/Pt	27	1.2 x 10^{-5}	Present
Au-BNNS/Pt	27	3.2 x 10^{-5}	Present
Ni-BNNS/Pt	28	2.4 x1 0^{-5}	Present
BNNS/Au	40	1.6 x 10^{-6}	Present
Au-BNNS/Au	44	4.8 x 10^{-6}	Present
Ni-BNNS/Au	71	2.5 x 10^{-6}	Present
Pt	30	4.5 x 10^{-4}	2
MoS_2	41	8.0 x 10^{-6}	20, 21
WS_2	33	2.0 x 10^{-5}	24
Ni_2P	46	3.3 × 10^{-5}	12

5.2.5 HER/HOR measurements of BNNS and Au-BNNS

The polarization curves of HER and the HOR are recorded in a H_2 saturated 0.5 M H_2SO_4 solution at the rotation rate of 1500 rpm is shown in Figure 5.5. The HER and the HOR are among the fastest known electrochemical reactions on Pt in acidic solution with the very small overpotential as shown in Figure 5.5(i). After the modification of Au-BNNS (Figure 5.5(ii)) and BNNS (Figure 5.5(iii)) the hydrogen evolution current starts to flow near overpotential zero and ~30 mV respectively, as observed in section (5.2.3.1), whereas the hydrogen oxidation current was comparatively reduced on both Au-BNNS and BNNS modified Pt electrode. Bulk Au is known to be an inert electrocatalyst. As shown in Figure 5.5(iv), it has poor catalysing behaviour towards HER and HOR. Interestingly, BNNS (Figure 5.5(v)) and Au-BNNS (Figure(vi)) modified on Au showed enhanced HER performance close to Pt and there is no enhanced HOR were observed as it is a typical behaviour on Au. The overpotential for the HER at BNNS and Au-BNNS modified Au showed ~90 and ~ 70 mV as observed in Ar saturated solution (section (5.2.3.1)). Interestingly, at Au electrode is not enhanced by BNNS and Au-BNNS modification, showing the unique feature of this catalyst.

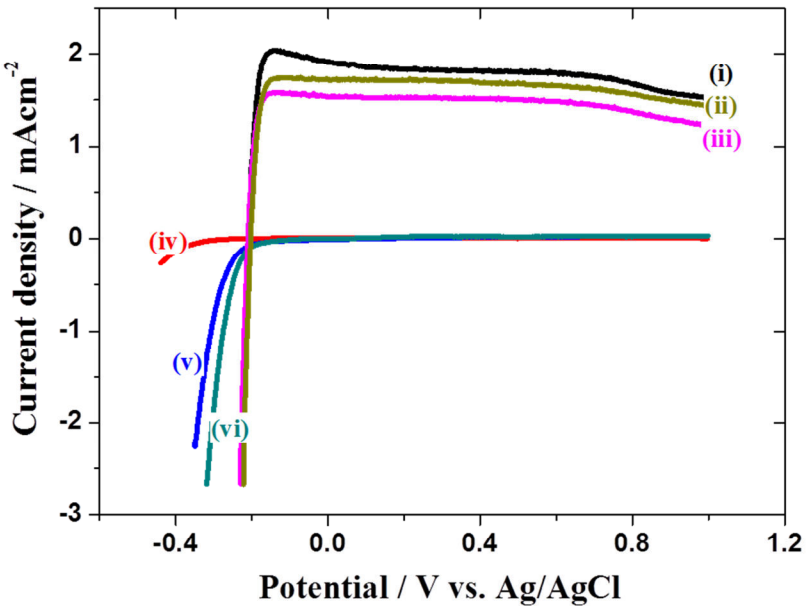

Figure: 5.5 HER/HOR polarization curves on (i) Pt, (ii) Au-BNNS and (iii) BNNS modified Pt, (iv) bare Au, (v) BNNS and (vi) Au-BNNS modified Au in H_2 saturated 0.5 M H_2SO_4 at the rotation rate of 1500 rpm. Scan rate 1 mV Sec^{-1}.

5. 3 Conclusion

The electrocatalytic activity of BNNS, and BNNS decorated with Au- and Ni-NCs modified on various substrates have been investigated. The obtained Au-BNNS modified on Au (or) Pt (or) GC system have demonstrated the superior electrocatalytic activity than at its host substrate. The HER activity observed on BNNS, BNNS decorated with Au- and Ni-NCs, induced the positive HER potential shift on Au about +110 mV, +130 mV, +60 mV, respectively. Its on Pt -10 mV, +14 mV, +10 mV, respectively, whereas its on GC about +100 mV, +620 mV, +200 mV, respectively. The interface between the BNNS and metal can play a vital role in the observed enhancement of the HER. The superior catalytic activity of Au-decorated with BNNS showing the importance of Au-BN interaction for the enhancement of HER as well, as observed for ORR. Interestingly, hydrogen oxidation reaction (HOR), i.e., reverse reaction of HER, at Au electrode is not enhanced by BNNS and Au- or Ni-BNNS modification, showing the unique feature of this catalyst. The findings in this work may pave the way for developing other high efficiency non-Pt based catalysts for Electrocatalysis, fuel cells and water–gas shift reactions.

5. 4 References

(1) M. H. Miles, *J. Electroanal. Chem.*, 60 **(1975)**, 89.

(2) N. M. Markovic, B. N. Grgur, and P. N. Ross, *J. Phys. Chem. B* 101 **(1997)**, 5405.

(3) A. Anani, A. Visitin, K. Petrov, S. Srinivasan, J. J. Reilly, J. R. Johnson, R. B. Schwarz and P. B. Desch, *J. Power Sources*, 47 **(1994)**, 261.

(4) K. Watanabe and T. Kikuoka, *J. Appl. Electrochem.*, 25 **(1995)**, 219.

(5) J. Greeley, and N. M. Markovic, *Energy Environ. Sci.*, 5, **(2012)**, 9246.

(6) J. B. Goodenough, *J. Solid State Electrochem.*, 16 **(2012)**, 2019.

(7) J. O. M. Bockris and E. C. Potter, *J. Electrochem. Soc.*, 99 **(1952)**, 169.

(8) W.-F. Chen, J. T. Muckerman, and E. Fujita, *Chem. Commun.*, 49 **(2013)**, 8896.

(9) D. M. Soares, O. Teschke, and I. Torriani, *J. Electrochem. Soc.,* 139 **(1992),** 98.

(10) J. Tamm, L. Tamm, and J. Arol'd, *Russ. J. Electrochem.,* 40 **(2004),** 1343.

(11) W.-F. Chen, K. Sasaki, C. Ma, A. I. Frenkel, N. Marinkovic, J. T. Muckerman, Y. Zhu, and R. R. Adzic, *Angew. Chem. Int. Ed.,* 51 **(2012),** 6131.

(12) E. J. Popczun, J. R. McKone, C. G. Read, A. J. Biacchi, A. M. Wiltrout, N. S. Lewis, and R. E. Schaak, *J. Am. Chem. Soc*., 135 **(2013),** 9267.

(13) J. O. M. Bockris and E. C. Potter, *J. Electrochem. Soc.,* 99 **(1952),** 169.

(14) V. S. Bagotsky, Fundamentals of electrochemistry, John Wiley & Sons, Inc., Hoboken, New Jersey, 2nd edn, **(2006)**.

(15) A. B. Laursen, S. Kegnaes, S. Dahl and I. Chorkendorff, *Energy Environ. Sci.*, 5 **(2012),** 5577.

(16) D. Merki and X. L. Hu, *Energy Environ. Sci.,* 4 **(2011),** 3878.

(17) S. S. Chou, M. De, J. Kim, S. Byun, C. Dykstra, J. Yu, J. Huang and V. P. Dravid, *J. Am. Chem. Soc.,* 135 **(2013)**, 4584.

(18) D. Merki, S. Fierro, H. Vrubel and X. L. Hu, *Chem. Sci.,* 2 **(2011),** 1262.

(19) H. Vrubel, D. Merki and X. Hu, *Energy Environ. Sci.*, 5 **(2012),** 6136.

(20) Y. Li, H. Wang, L. Xie, Y. Liang, G. Hong, and H. Dai, *J. Am. Chem. Soc.*, 133 **(2012)**, 7296.

(21) T. F. Jaramillo, K. P. Jorgensen, J. Bonde, J. H. Nielsen, S. Horch, and Ib. Chaokendorff, *Science*, 317 **(2007),** 100.

(22) B. Hinnemann, P. G. Moses, J. Bonde, K. P. Jørgensen, J. H. Nielsen, S. Horch, I. Chorkendorff and J. K. Nørskov, *J. Am. Chem. Soc.,* 127 **(2005),** 5308.

(23) Z. Z. Wu, B. Z. Fang, A. Bonakdarpour, A. K. Sun, D. P. Wilkinson and D. Z. Wang, *Appl. Catal., B*, 125 **(2012),** 59.

(24) D. Voiry, H. Yamaguchi, J. Li, R. Silva, D. C. B. Alves, T. Fujita, M. Chen, T. Asefa, V. B. Shenoy, G. Eda, and M. Chhowalla, *Nat. Mater.,* 12 **(2013)**, 850.

(25) M. V. Bollinger, J. V. Lauritsen, K. W. Jacobsen, J. K. Nørskov, S. Helveg, and F. Besenbacher, *Phy. Rev. Lett.,* 87 **(2001)**, 196803.

(26) A. Lyalin, A. Nakayama, K. Uosaki and T. Taketsugu, *Phys. Chem. Chem. Phys.*, 15 **(2013)**, 2809.

(27) A. Lyalin, A. Nakayama, K. Uosaki and T. Taketsugu, *J. Phys. Chem. C*, 117 **(2013),** 21359.

(28) V. L. Solozhenko, A. G. Lazarenko, J. P. Petitet and A. V. Kanaev, *J. Phys. Chem. Solids*, 62 **(2001)**, 1331 and references therein.

(29) D. Golberg, Y. Bando, Y. Huang, T. Terao, M. Mitome, C. Tang and C. Zhi, *ACS Nano*, 4 **(2010)**, 2979.

(30) Y. Lin and J. W. Connell, *Nanoscale*, 4 **(2012)**, 6908.

(31) T. Oku, in Physical and Chemical Properties of Carbon Nanotube, ed. S. Suzuki, Intech, **(2013)**, ch. 5.

(32) Z. Liu, Y. Gong, W. Zhou, L. Ma, J. Yu, J. C. Idrobo, J. Jung, A. H. MacDonald, R.

Vajtai, J. Lou and P. M. Ajayan, *Nat. Commun.*, 4 **(2013),** 2541.

(33) H. Zheng, C. Zhi, Z. Zhang, X. Wei, X. Wang, W. Guo, Y. Bando and D. Golberg, *Nano Lett.,* 10 **(2010)**, 5049.

(34) S. Azevedo, J. R. Kaschny, C. M. C. de Castilho and F. de Brito Mota, *Eur. Phys. J. B*, 67 **(2009)**, 507.

(35) R. Laskowski, P. Blaha and K. Schwarz, *Phys. Rev. B*, 78 **(2008)**, 045409.

(36) M. Gao, A. Lyalin and T. Taketsugu, *Int. J. Quantum Chem.* 113 **(2013)**, 443.

(37) M. Gao, A. Lyalin and T. Taketsugu, *J. Phys. Chem. C*, 116 **(2012)**, 9054.

(38) M. Gao, A. Lyalin and T. Taketsugu, *J. Chem. Phys.,* 138 **(2013)**, 034701.

(39) M. Gao, A. Lyalin, T. Taketsugu, *J. Chem. Phys.,* 138 **(2013)**, 034701.

(40) Q. Sun, Z. Li, D. J. Searles, Y. Chen, G. M. Lu, A. Du, *J. Am. Chem. Soc.,* 135, **(2013)**, 8246.

(41) P. Wang, S. Orimo, T. Matsushima, H. Fujii, *Appl. Phys. Lett.*, 80 **(2002),** 318.

(42) R. Ma, Y. Bando, H. Zhu, T. Sato, C. Xu, D. Wu, *J. Am. Chem. Soc.,* 124, **(2002)**, 7672.

(43) C. C. Tong, Y. Bando, X. X. Ding, S. R. Qi, D. Golberg, *J. Am. Chem. Soc.*, 124 **(2002)**, 14550.

(44) S.-H. Jhi, Y.-K. Kwon, *Phys. Rev. B* 69 **(2004)**, 245407.

(45) G. Mpourmpakis, G. E. Froudakis, *Catalysis Today*, 120 **(2007),** 341.

(46) Q. Weng, X. Wang, C. Zhi, Y. Bando, D. Golberg, *ACS Nano*, 7 **(2013),** 1558.

(47) S. A. Shevlin, Z. X. Guo, *Appl. Phys. Lett.*, 89 **(2006)**, 153104.

(48) E. Durgun, Y.-R. Jang, S. Ciraci, *Phys. Rev. B* 76 **(2007)**, 073413.

(49) W. Sheng, H. A. Gasteiger, and Y. Shao-Horn, *J. Electrochem. Soc.,* 157 **(2010)**, B1529.

(50) D. Strmcnik, K. Kodama, D. van der Vliet, J. Greeley, V. R. Stamenkovic and N. M. Markovic, *Nat. Chem.,* 1 **(2009)**, 466.

(51) H. B. Gray, *Nat. Chem.,* 1 **(2009)**, 7.

(52) B. E. Conway and B. Timothy, *Electrochim. Acta*, 47 **(2002)**, 3571.

(53) D. Stmcnik, D. Tripkovic, D. van der Vliet, V. R. Stamenkovic and N. M. Markovic, *Electrochem. Commun.*, 10 **(2008)**, 1602.

(54) Y. H. Li, J. Xing, Z. J. Chen, Z. Li, F. Tian, L. R. Zheng, H. F. Wang, P. Hu, H. J. Zhao and H. G. Yang, *Nat. Commun.*, 4 **(2013)**, 1.

(55) K.-W. Park, J.-H. Choi, B.-K. Kwon, S.-A. Lee, Y.-E. Sung, H.-Y. Ha, S.-A. Hong, H. Kim and A. Wieckowski, *J. Phys. Chem. B* 106 **(2002)**, 1869.

(56) L.-R. Zhang, J. Zhao, M. Li, H.-T. Ni, J.-L. Zhang, X.-M. Feng, Y.-W. Ma, Q.-L. Fan,

X.-Z. Wang, Z. Hu and W. Huang, *New J. Chem.,* 36 **(2012)**, 1108.

(57) K. S. Kim, and N. Winograd, *Surf. Sci*. 43 **(1974)**, 623.

(58) N. S. McIntyre, and M. G. Cook, *Anal. Chem.,* 47 **(1975),** 2208.

(59) D. B. Mitton, J. Walton, and G. E. Thomson, *Surf. Interface Ana*l., 20 **(1993),** 36.

(60) R. Shulz, A. Van Neste, P. A. Zielinski, S. Boily, F. Czerwinski, J. Szpunar, and S. Kaliaguine, *Catal. Lett.*, 35 **(1995)**, 89.

(61) H.-W. Hoppe, and H.-H. Strehblow, *Surf. Interface Anal.,* 14 (1989), 121.

(62) J. C. Klein, and D. M. J. Hercules, *Catal*., 82 **(1983),** 424.

(63) K. T. Ng, and D. M. J. Hercules, *Phys. Chem.,* 80 **(1976)**, 2094.

(64) D. K. Paul, Y. Xie, and P. M. A. Sherwood, *Anal. Chem.,* 65 **(1993)**, 2276.

(65) P. F. Luo, T. Kuwana, D. K. Paul, and P. M. A. Sherwood, *Anal. Chem.,* 68 **(1996)**, 3330.

(66) I. G. Casella, M. R. Guascito, and M. G. J. Sannazzaro, *Electroanal. Chem.,* 462 **(1999)**, 202.

(67) J. Legard, A. Taleb, S. Gota, M.-J. Guittet and C. Petit, *Langmuir,* 18 **(2002)**, 4131.

(68) W. T. Evans and M. Schlesinger, *J. Electrochem. Soc.*, 141 **(1994)**, 78.

(69) Z. Liu, Y. Gong, W. Zhou, L. Ma, J. Yu, J. C. Idrobo, J. Jung, A. H. MacDonald, R. Vajtai, J. Lou and P. M. Ajayan, *Nat. Commun.*, 4 **(2013)**, 1.

(70) M. R. Gennero de Chialvo and A. C. Chialvo, *J. Electroanal.Chem.*, 372 **(1994)**, 209.

(71) B. E. Conway, and B. V. Tilak, *Electrochim. Acta,* 47 **(2002)**, 3571.

Chapter 6

GENERAL CONCLUSION AND FUTURE PROSPECTS

6.1 General Conclusion

Electrocatalytic reduction of oxygen, hydrogen evolution reactions of various structures of Boron Nitride were investigated in this thesis.

In Chapter 3, the electrocatalytic activities of various types of h-BN such as BN nanotube (BNNT), BN nanosheets (BNNS), and sputter deposited BN, coated on Au, glassy carbon (GC) and Pt electrodes, for ORR are examined. The overpotential for ORR at Au electrode was reduced by ca. 100, ca. 270, and ca.150 mV by coating with BNNT, BNNS, and sputter deposited BN, respectively, showing the enhancement of electrocatalytic activity. Rotating disk electrode (RDE) and rotating ring disk electrode (RRDE) studies showed that O_2 is reduced to H_2O_2 by 2-electron reduction. On the other hand, ORR activity of GC electrode was not enhanced and that of Pt is reduced by the BNNS modification, suggesting that the BN-Au substrate interaction plays an important role for BN to become ORR active. Hence, I intended to decorate the Au nanoclusters on BNNS to confirm the role of Au-BN interaction.

In Chapter 4, the electrocatalytic reactivity of BNNS decorated with Au nanoclusters (Au-BNNS) on Au for ORR is examined. The overpotential of ORR at Au electrode was significantly reduced by 300 mV by the modification of Au-BNNS. The enhanced catalytic activity of Au-BNNS was attributed to the electron transfer at the interface between Au and neighbouring B- and/or N- atoms. The number of electrons involved in ORR determined from the slope of Koutecky-Levich plot was about 3 and RRDE measurements suggest the partial production of H_2O_2 by 2-electron reduction and H_2O by 4-electron reduction. This is in contrast to the results at the bare and BNNS modified Au electrodes, where only H_2O_2 was formed by 2-electron reduction. Electrocatalytic activity for ORR was enhanced even at the GC electrode when it was modified by Au-BNNS, confirming the importance of Au-BN interaction for the enhancement of electrocatalytic activity.

Inasaki et al. (*Electrochim. Acta* 54 (2009), 4893) and Yagi et al. (*Electrochem. Commun*. 6 (2004), 773) reported the ORR activity of Au nanoclusters (NCs) modified on carbon and boron doped diamond in acidic solution, respectively. They have demonstrated

that the overpotential at Au was reduced by 100 to 200 mV. However, the present study demonstrates that Au-BNNS modification reduced the overpotential of Au by 300 mV, suggests that BNNS can be good candidate to promote the catalytic activity of Au-NCs. Although the present catalyst BNNS and Au-BNNS are not as active as Pt for ORR, the present experimental study demonstrates the possibility to functionalize the inert materials to become ORR active catalyst, opening new ways to design effective Pt-free catalysts for fuel cell based on materials which never before considered as catalysts.

In Chapter 5, the electrocatalytic evolution of hydrogen at Au, GC and Pt modified by BNNS and BNNS decorated with Au- and Ni-NCs (Au-BNNS and Ni-BNNS) were investigated. HER at Au, GC and Pt electrodes were enhanced, not much changed, and reduced, respectively, by BNNS modification as for ORR. HER at Au, GC and Pt electrodes were all enhanced by the modification of Au-BNNS. HER activity of Au electrode modified by Au-BNNS was very high with only ca. 50 mV more overpotential than Pt. Modification by Ni-BNNS also showed enhanced HER activity but much less than by the Au-BNNS modification, showing the important role of Au-BN interaction for the enhancement of HER as well. Interestingly, hydrogen oxidation reaction (HOR), i.e., reverse reaction of HER, at Au electrode was not enhanced by BNNS and Au (or) Ni-BNNS modification, showing the unique feature of this catalyst.

Recently developed 2D materials (XS_2), such as MoS_2 (*J. Am. Chem. Soc*. 133 (2011), 7296) and WS_2 (*Nature Mater*. 12 (2013), 850) were demonstrated as efficient electrocatalyst for HER with the overpotential of 100 to 200 mV. Perhaps, the present Au-BNNS showed better HER catalytic activity than those XS_2 materials with only ca. 50 mV overpotential than Pt. The findings in this work may pave the way for developing other high efficiency non-platinum based catalysts for electrocatalysis, fuel cells and water–gas shift reactions.

6.2 Future Prospect

As emphasized in this thesis, Au-BNNS showed enhanced ORR and HER activity. Although it showed highest electrocatalytic performance than BNNT, BNNS and sputter deposited BN modified Au, still it is suffering from overpotential of ~450 mV for ORR. Significant improvements are still required to decorate the well-ordered uniform size metal nanoclusters on BNNS to act as an efficient ORR electrocatalyst. In future it can be done by optimizing the preparation conditions of BNNS with highly exposed edges and vacancy defects. It is possible to increase the number edges by reducing the BNNS size, which

possibly increase the active sites and promote the ORR as suggested by the theoretical calculations.

It was demonstrated that the interface between the BN and Au plays a crucial role for the enhancement of the electrocatalytic activity against ORR and HER. Based on the XPS studies, electron transfer was observed between Au and BN. Detailed studies are required to evaluate the effect of interface for the catalytic activity of BN. In future it can be done by performing the in-situ IR, Scanning electrochemical microscopy studies (SECM) and X-ray absorption fine structure (XAFS) measurements to evaluate the electrocatalytic active sites and the electron transfer process, respectively.

It was also demonstrated the both BNNS and Au-BNNS modified Au showed very ~70 and ~ 50 mV, respectively, more overpotential than Pt against HER and it was not enhanced the HOR activity. In future, photocatalytic evolution of hydrogen on BNNS and BNNS decorated with various transition metal-NCs will be studied for real time applications.